Theoretical and Experimental Identification of Brake Pad Material Properties

Thesis submitted in accordance with the requirements of the University of Liverpool for the degree of Doctor in Philosophy

By

LiangLiang Liu

March 2022

Abstract

The research of the noise, vibration and harshness (NVH) of the brake system of a vehicle has been carried out for many years. Much effort has been made to improve the predictability of various numerical methods to attack the problem in the early design stage. However, current finite element models for simulation and analysis are still not accurate. One of the reasons is the lack of knowledge of the mechanical properties of the friction pads of car brakes.

The main focus of the research in this thesis aims at developing a more efficient and reliable method to identify the material properties such as the Young's Modulus, Poisson's Ratio, and Shear Modulus of the pad friction material in all directions. Two methods are used in this project, the Sensitivity Method and the optimization algorithm in MSC/Nastran solution 200. Both methods aim to minimize the difference between the analytical dynamic response, such as the natural frequencies and mode shapes, and the experimental dynamic response of the pad.

The analytical dynamic response of the pad is determined using the finite element (FE) model built in ABAQUS software. Two dynamic experimental methods are proposed and compared. The experimental dynamic response is collected from the Acceleration/Force dynamic testing method. Furthermore, a new method is proposed to collect the changes in stress and strain of the friction material in all directions using Digital Imaging Correlation (DIC). This compression test method gives more accurate results compared with the conventional method for the friction material, which uses a strain gauge to measure the lateral strain.

Two MATLAB programs are developed for the Sensitivity Method and the optimization method in MSC/Nastran solution 200 identification methods. The advantages of the developed programs are the user-friendliness, more functions, faster computation compared with the design of the experiment method, and the more detailed and accurate results of the updated material properties of the pad friction material.

Another research topic in this project is to analyze the pad friction material as a Hyperelastic material instead of an elastic material in the pad FE model. This analysis is carried out using ABAQUS software, and the compression test results are used to simulate the pad friction material as different types of hyperelastic material. A suitable type of hyperelastic material in ABAQUS software is determined from the static results collected from the compression test.

The theoretical analysis of the damping of the pad friction material is also proposed in this thesis. However, the research is only theoretical due to the lack of experimental data on the damping of the friction material. This topic is worth studying in the future.

Acknowledgements

Table of Content

List of Figures

X

List of Tables

XIII

Nomenclature

c, c_i	(*i*th) Damping of a system
$\mathbf{C}$	Damping matrix of an MDOF system
$f, \mathbf{f}$	Force and force vector
$F(\omega)$	The input signal in the frequency domain
$\underline{F}(\omega)$	The input signal vector
$\underline{F}^m(\omega)$	The measured input signal vector
$H(s)$	Transfer function
$H(\omega)$	The FRF of a SISO system
$H_1(\omega), H_2(\omega), H_v(\omega)$	Different FRF estimators used in a modal test
$\mathbf{H}(\omega)$	The FRF matrix
k, k_i	(*i*th) Stiffness of a system
$\mathbf{K}$	Stiffness matrix of an MDOF system
m, m_i	(*i*th) Mass of a system
$\mathbf{M}$	Mass matrix of an MDOF system
$\underline{N}^f(\omega)$	Input noise vector

$\underline{N}^x(\omega)$	Output noise vector
t	Time in second [s]
$\mathbf{x}, \dot{\mathbf{x}}, \ddot{\mathbf{x}}$	Physical coordinates (Displacement) vector and its first derivative (Velocity) and second derivative (Acceleration)
x, y, z	Cartesian coordinates, displacements
$X(\omega)$	The output signal in the frequency domain
$\underline{X}(\omega)$	The output signal vector
$\underline{X}^m(\omega)$	The measured output signal vector
λ	
$\gamma^2(\omega)$	The ordinary coherence function
ω	Frequency in radius per second, [rad/s]
ω^f	Frequency in Hertz [Hz]
L	Laplace transform

Notation

Items	Font Type	Example
Absolute values	Normal with vertical line brackets	|Scalar|, |*Variable*|
Constants	Normal	π
Functions with more-than-one-letter names	Normal	sin, log, ln
Matrices	Bold upper case normal	$\mathbf{M}$
Numbers	Normal	1, 2
Physical units	Normal with square brackets	[kg], [MPa]
Subscripts	Italic (if Variable)	x_i
	Normal (if Constants or Numbers)	x_1
Superscripts	Italic (if Variable)	x^i
	Normal (if Constants or Numbers)	x^1
Variables	Italic	x, ω
Vectors	Bold normal (if in lower case)	$\mathbf{x}$
	Normal with single underline (if in upper case)	$\underline{X}$

Acronyms

1D, 2D, 3D	One Dimensional, Two Dimensional, Three Dimensional
CAE	Computer-aided Engineering
CEA	Complex Eigenvalue Analysis
DIC	Digital Imaging Colleration
DOF	Degree of freedom
EOM	Equation of Motion
FE	Finite Element
FEA	Finite Element Analysis
FRF	Frequency Response Function
LDV	Laser Doppler Vibrometer
MAC	Modal Assurance Criterion
MDOF	Multi Degree of Freedom
MIMO	Multi Input Multi Output
MISO	Multi Input Single Output
SDOF	Single Degree of Freedom
SIMO	Single Input Multi Output
SISO	Single Input Single Output

Chapter 1 Introduction

1.1 Background

In modern days, due to people's demand for a faster and better travelling experience, many new technologies have been developed in the transportation industry to provide more powerful vehicles. The brake of a vehicle is the most important component as it ensures the safety of the passenger. Therefore, the braking system of a vehicle must follow the same rate of development and more research are put into the braking system. Nowadays, more researchers and engineers have shown their interest in developing the braking system.

Two main service brakes are being used on-road vehicles: disc brakes and drum brakes. Emergency brakes are also equipped on almost all road vehicles, and antilock braking systems (ABS) are used on many modern road vehicles.

<u>Disc Brakes</u>

A disc brake consists of a rotor (disc) that attaches to the wheel and rotates with it. A calliper is attached to the axle of the vehicle and holds two brake pads just outside the rotor. While applying the brake pedal, hydraulic pressure from the master cylinder causes the calliper to clamp the brake pads against the disc surface. The friction force generated between the disc and the brake pads causes the disc to slow down and stop, so the vehicle decelerates as the wheel slows down. The friction surface of the brake pad only covers a portion (typically no more than 15%) of the rotor friction surface area (Day, 2014).

There are two main designs of disc brake calliper that are commonly used today: fixed calliper (or dual-calliper) disc brakes and floating calliper (sliding) disc brakes. A fixed calliper disc brake contains two separate sets of pistons located on each side of the disc. When the brake is applied, both sets of pistons are moved towards the disc, and the actuation force is uniformly distributed on the friction interface on both sides. On the other hand, in a floating calliper disc brake, the inner and outer bodies of the calliper are fitted with two rods or pins and only one piston is embedded on the inner side of the calliper. The force applied to the inner piston generates a reaction force that slides the outer calliper

towards the disc during a brake operation. The applied and reaction force are almost equal, with a small difference due to the friction in the sliding rods.

Figure 1.1 shows a fixed calliper disc brake, and Figure 1.2 is a floating-calliper disc brake. The fixed calliper disc brakes require more space and are heavier compared with the floating calliper disc brakes. Therefore, fixed calliper disc brakes are often used in high-performance road vehicles, and floating disc brakes are used on small road vehicles.
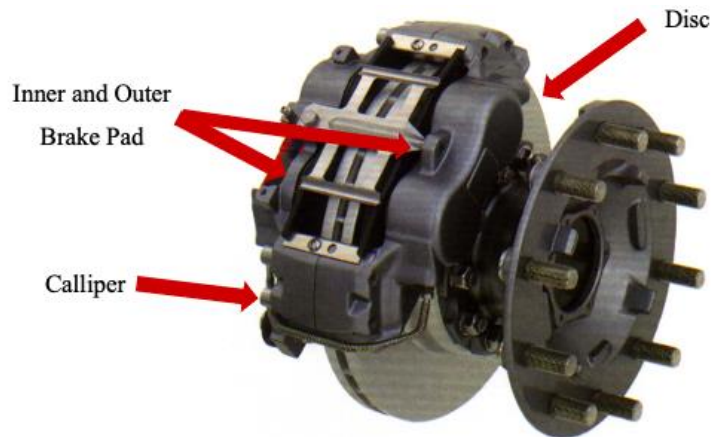
Figure 1.1 Fixed-caliper Disc Brake ((Day, 2014))
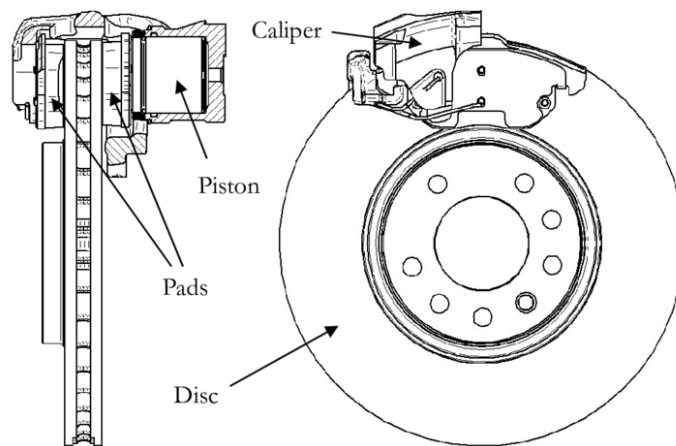
Figure 1.2 Floating-calliper Disc Brake (Wahlström, 2011)

Drum Brakes

A drum brake consists of a brake drum attached to the wheel hub and rotates with it. The friction material linings, known as 'brake shoes', are mounted on a backplate attached to the vehicle's axle. While applying the brake pedal, the

shoes are forced outwards against the inner surface of the drum. The friction force between the inner surface of the drum and the brake shoes causes the drum to slow down; hence the wheel attached to the drum would slow down and stop. The friction surface of the brake linings covers most of the drum's friction surface area, typically around 70% (Day, 2014).
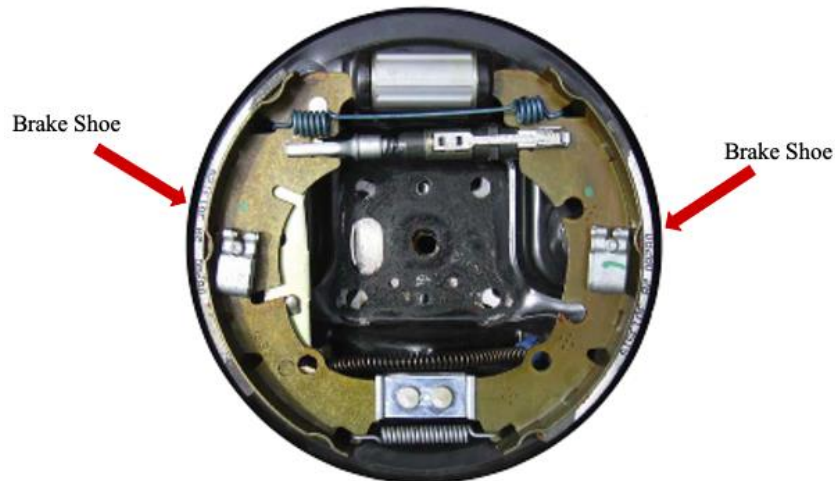
Figure 1.3 Drum brake with two brake shoes (Day, 2014)

Emergency Brakes

Emergency brakes are also known as hand brakes or parking brakes. Generally, emergency brakes are used to keep the vehicle stationary while parked. Emergency brakes work independently from the disc or drum brakes and are powered by a cable that mechanically applies pressure to the wheels. (Day, 2014)

Antilock braking systems (ABS)

Antilock braking systems (ABS) are found on modern vehicles and are mainly used to prevent skidding. An antilock system requires the computational design to decide what to measure and how to use the measured data to prevent the wheels from locking up and the tires from skidding. This feature is useful when driving in rainy weather or on wet or slippery roads. (Orthwein, 2004)

While applying the brake pedal, the kinetic energy of the motion of the vehicle is converted into heat by the friction generated between the rotor and friction material stators. Overheating problems must be avoided in the brake design

3

process, and the heat generated must be dissipated effectively and efficiently by the brake components. The design of disc brakes gives a better heat dissipation ability than drum brakes; however, disc brakes are more expensive in comparison (Day, 2014). In modern car industries, disc brakes are fitted into the front axles of the car and drum brakes are used as the rear brakes. In this project, the main type of brake focused is the disc brake.

The research of the noise, vibration and harshness (NVH) of the brake system of a vehicle has been carried out for many years. One motivation is the environmental concern of the noise pollution emitted during brake operations. Another concern is the expectation from the customer of a better quality of the brake.

Many different types of noise can be generated from the brake system; brake squeal from the braking system of the vehicle is one of the major concerns to the drivers and the car manufacturers; another major concern is the judder. Brake noise occurs over a wide range of frequencies, typically from 100 Hz to above 20 kHz (which is the upper limit of human audibility), and the classic brake 'squeal' noise is often in the region of 1-6 kHz, where the human ear is most sensitive (Day, 2014).

Both noise and judder problems have been high-warranty problems in the automotive industry worldwide. Manufacturers continue to search for quiet brakes to reduce warranty costs until today. Various researches have been made to improve the predictability of the brake squeal in the early design stage, but the effective predictability of designing a quiet (or judder-free) brake remains a challenge.

Ouyang et al. (2005) stated that theoretical and experimental methods are important in understanding the brake squeal. The simulation and analysis of brake squeal can be made by two distinct methods: time-domain analysis and complex eigenvalue analysis. However, current finite element models for simulation and analysis are still not accurate. One of the reasons is the lack of knowledge of the mechanical properties of the friction pads of car brakes. Dealing with this modelling inadequacy is the main motivation of this research project.

4

1.1.1 Types of Brake Pads

Brakes pads were originally made from asbestos because of their fibrous nature, low density, thermal insulation, mild wear, and stable coefficient of friction (Dante, 2015), which was very suitable for the performance of the brake pads. However, asbestos was found to have many disadvantages over time; one of the main reasons to replace asbestos is toxic, and prolonged exposure can potentially cause cancer. As an asbestos-based brake pad wears down, the decomposed asbestos would be released into the air, which is unsafe to use.

Since the mid-1980s, many uses of asbestos have been banned in several countries. Artificial fibres have been manufactured and used in many applications to replace asbestos (Soto and Salazar, 2009). Copper (powder and fibre) and steel fibres became two important ingredients for friction materials (Dante, 2015). However, lately, copper was banned by the US government under the enactment of the prevention of the users of copper law (Sundarkrishnaa, 2015). Rubber is used in the brake pads formulas to provide better damping and reduce brake noise or judder. Rubber also provides better compressibility and flexibility in brake linings (Dante, 2015).

Although different brake pad manufacturers would have slightly different formulas for their pads, generally, there are three classes of brake pads: the non-asbestos, semi-metallic and low-steel pads (Day, 2014).

Semi-Metallic Formula

Semi-metallic brake pads are used in most road vehicles nowadays to replace asbestos pads. This type of brake pad is made up of high content of metals (usually greater than 50%). The metals, including steel fibre (normally larger than 30%), copper, copper alloys (bronze and brass), and tin and zinc in some cases, are mixed and compressed together with strong abrasives and lubricants (graphite). The coefficient of friction of the semi-metallic pads is usually around 0.4. (Dante, 2015)

Semi-metallic brake pads are known to last longer and perform well as their formulas are primarily the content of metals. They are cheaper to be replaced and most suitable for daily use vehicles. Heavy-duty vehicles also use semi-metallic brake pads because they need high braking power with heavier loads. A

disadvantage of the semi-metallic pads is that they are heavier compared with types of brake pads.

Low Steel and Low Metal Formula

The friction material formula for low steel and low metal pads is very similar. The low steel formula contains less than 20% of steel fibres, whereas the low metal formula contains metals lower than 20%, including steel fibres. (Dante, 2015)

Generally, the average coefficient of friction for the low steel or low metal pads is around 0.35-0.38, which is lower than for the semi-metallic pads. The size of the abrasive would affect the wear rate. Round shaped particles are used in these formulas to reduce the wear rate of the pad due to abrasion. (Dante, 2015)

The low steel formulae would have a higher coefficient of friction than the low metal formulae because of the higher steel fibre content. Hence, the low steel pads are more suitable for the front brakes, and the low metal pads are more suitable for the rear axles (Dante, 2015). The low steel formulae usually use fewer abrasives than low metal formulas, and more steel fibre would cause more noise and vibration. Hence, a damping system, premixing materials with rubber and lubricant, is used in the low steel formulae to minimise the negative effects of steel fibre (Dante, 2015).

Ceramic (Non-Asbestos Organic) Formulas

Ceramic formulas, also known as Non-Asbestos Organic (NAO) formulas, tend to use copper instead of steel fibres in their formula to favour heat dissipation. The metal content in the ceramic formula is normally less than 20%. Ceramic friction materials have a high content of ceramic fibres such as Ca–Mg silicates, rock wool, and fibrous titanates (Dante, 2015). Ceramic friction pads are normally made of a mixture of ceramic fibres and materials such as rubber, carbon compounds, glass or fibreglass, Kevlar, and more and are bound together with resin (Day, 2014).

These ceramic pads are lightly weighted because of their composite nature. They tend to have a lower friction coefficient than the other two pad formulas. They are quieter and less likely to cause brake squeal or judder. Ceramic pads also last

longer and produce less dust than other formulas. (Dante, 2015, Kumar and Kumaran, 2019)

One of the biggest disadvantages of using ceramic pads is that they tend to be more expensive, so replacing them is costly (Day, 2014). Also, the design of ceramic formula is moving to a different concept because of the restraint of using copper in the United States recently.

1.1.2 Brake Pad Components

The brake pad for a disc brake may be different for many reasons: the size of the vehicle, different designs of the disc brake, the friction material formula, etc. For example, Figures 1.3 and 1.4 show two brake pads currently used in the Jaguar Land Rover company. Figure 1.3 shows a brake pad model with two friction material blocks and a slot in the middle, whereas the brake pad in Figure 1.4 does not have a slot and the friction material is a whole part.

Although different brake pad models may have slightly different designs, brake pads generally have the following components in their design.

Friction Material Block

The surface of the friction material is clamped against the disc surface, which generates the friction force and causes the vehicle to slow down and stop. There are different formulas for the friction material (shown in section 1.1.1), and the coefficient of friction may vary depending on the friction material formulation.

Backplate

The backplate is one of the components required in a brake pad. They are generally made from steel and are used to mount the pad friction material within the brake calliper (Muscoplat, 2019, Newby, 2014). The backplate also provides support to the friction material so that it is strong enough to withstand the compression force applied to the pad during operation (Day, 2014).

The piston acts directly to the backplate for a hydraulically actuated brake, and the pressure is distributed evenly to the friction material block (Day, 2014,

Newby, 2014). The backplate also transfers the heat generated between the disc surface and friction material surface away from the friction material block (Newby, 2014).

Figure 1.4 Pad model FER7217 with ear and shim removed (Front)

Figure 1.5 Pad model FER7217 with ear and shim removed (Back)

Figure 1.6 Pad model GA8135 without slot (Front)

Figure 1.7 Pad model GA8135 without slot (Back)

Underlayer and Bonding Adhesive

An adhesive layer is applied between the friction material and the backplate to chemically bond the two components together (Kumar and Kumaran, 2019, Day, 2014). It is very important to avoid debonding between the friction material and the backplate of the pad, so the adhesive must remain active even under extreme conditions and temperatures (Muscoplat, 2019, Day, 2014).

Additional to the adhesive layer, an underlayer (also known as interlayer) of the friction material is also used to increase the bond strength between the friction block and backplate (Day, 2014, Muscoplat, 2019). This interlayer contains a higher percentage of resin than the friction material surface (Muscoplat, 2019, ZRTMotorsport, 2016).

Shim

A shim is generally made from steel and is glued onto the backplate of the pad. The shim acts as a damping layer to increase the stability between the actuation piston and the backplate. The coupling stiffness and damping between the piston

and the backplate is altered; therefore, the brake noise propensity is reduced. The viscoelastic layer between the shim and the backplate also helps to eliminate the brake squeal noise (Day, 2014).

<u>Slot and Chamfers</u>

The purpose of both chamfers and slots in the friction material block is to reduce the brake noise propensity. The contact surface between the disc and the pad friction block is changed if chamfers are included in the design; hence the required range of brake noise could be reduced (Day, 2014, Muscoplat, 2019).

The slots in the friction material block change the natural frequency of the pad so that the brake squeal can be eliminated. The slot could also prevent the friction block from cracking as the flexural characteristics of the pad change (Day, 2014, ZRTMotorsport, 2016). Another function of the slots is to refresh the disc friction surface and prevent pad lift (Day, 2014, Muscoplat, 2019).

<u>Ear</u>

The ears on the backplate of the pad fix the pad to the calliper; hence, the brake pad would not move axially during a stop. (Muscoplat, 2019)

1.2 Aim and Objectives

Different pads have very different formulations and designs to match different operational duties and requirements, but the manufacturing processes for the pad friction materials can be generally classified as mixing, moulding and curing (stabilisation) (Dante, 2015). The pad friction materials tend to be non-isotropic, inhomogeneous and nonlinear.

Currently, in industries such as Jaguar Land Rover, the brake pad friction materials are treated as transversely isotropic material, where the isotropic plane is the friction material surface of the pad. A design of experiment method is used to determine the material properties, such as the Young's Modulus, Poisson's Ratio, and Shear Modulus of the pad friction material.

In the design of the experiment method, the range for the material properties of the friction material is set. This range narrows as the predicted results (such as frequencies modes) of the pad from the Finite Element Model converge to the test frequencies of the pad. The material properties of the pad are found as the error between the theoretical modal data of the FE model and the experimental modal data becomes acceptably small.

However, only the Young's Modulus of the isotropic plane of the pad friction material is determined and updated in the pad FE model, whereas the rest of the material properties of the friction material remain uncertain. This is because when more than one material property needs to be determined, the computation cost of the design of the experiment method increases significantly.

Another disadvantage of the design of the experiment method is that the range of the material properties must be correctly set at the beginning; otherwise, the convergence would be slow or even unsuccessful. Additionally, this method is not very efficient, and the number of iterations used to find the material properties of the friction material is large.

Since the material properties of the pad friction material are not determined accurately, the behaviour of the brake pad in the FE model is also not analysed correctly. Damping is not considered in the brake pad FE models, and nonlinearity is largely ignored.

Considering the above disadvantages of the current design of the experimental method used in Jaguar Land Rover, a more suitable and reliable identification method is proposed in this thesis to efficiently and accurately determine the material properties of the pad friction material.

Different parameter identification methods were reviewed in Chapter 2, and two methods were used in this project, the Sensitivity Method and the optimisation algorithm in MSC/Nastran solution 200. Both methods are based on sensitivity analysis, which concerns the rates of change of the dynamic responses of the brake pad with respect to the change in the design variables (Choi and Kim, 2005, MSCSoftware, 2012, Maia and Montalvão e Silva, 1997). The dynamic responses of the brake pad can be the natural frequencies and mode shapes or the FRFs of the pad. The design variables, in this case, are the material properties of the pad friction material such as the Young's Modulus, Poisson's Ratio, and Shear Modulus of the pad. Further details of the Sensitivity Method and the

optimisation algorithm in MSC/Nastran solution 200 will be included in Chapter 5.

It is important to consider analytical and experimental methods when determining the pad friction material properties. Two main dynamic testing methods were carried out in this project, 1. Acceleration/Force testing method, and 2. Velocity/Force testing method. Both methods have their advantages and disadvantages. Further details of the dynamic testing procedure will be included in Chapter 3.

The complex eigenvalue analysis (CEA) is used in the FE model to predict the analytical frequencies and mode shapes of the pad. The analytical modal data are correlated with the frequencies and mode shapes of the pad from the dynamic experiments.

In this thesis, the noise reduction shim is removed and will not be considered part of the brake pad in the theoretical and experimental analyses. The underlayer of the friction material and the friction block is assumed to be a whole part of the pad. The friction material and the backplate of the pad is bonded together, but the bonding adhesive layer is not included in the FE model.

1.2.1 Aim

This research project aims to characterise the mechanical properties of the friction material of the brake pads through identification and structural analysis methods based on vibration tests and implement them in realistic FE models of disc brakes for higher prediction accuracy. For this purpose, it is also crucial to establish reliable testing methods to collect useful test data such as frequencies and mode shapes of the brake pads. Knowledge of damping of the friction material of the brake pads remains scarce, and its identification and modelling will be investigated in this project. The concept of hyper-elastic material will also be studied, and its validity for the friction material will be explored.

1.2.2 Objectives

The Objectives of this project are:

1. To determine a procedure for reliable/repeatable dynamic testing method for measuring more than 9 reliable natural frequencies and mode shapes of the brake pad.

2. To measure the compressibility of pad friction materials in different directions at different average compressive stress (2, 4 and 6 MPa). The outcome will be several stress-strain diagrams.

3. To determine a procedure for identifying the material properties of brake pad friction material as non-isotropic materials in three dimensions and implement the updated material properties in FE models of brake pads.

4. To use the Hyperelastic material card in the FE model of the brake pad in ABAQUS and include the compressibility of pad friction materials in the pad FE simulations.

5. To identify the damping coefficients of the pad friction material in three dimensions and include the damping effect of the friction material to the pad FE simulation in ABAQUS.

1.3 Thesis Structure

This thesis consists of eight chapters, and the outline of each chapter is given below. The overall structure of this thesis is shown in a flowchart in Figure 1.8 below.
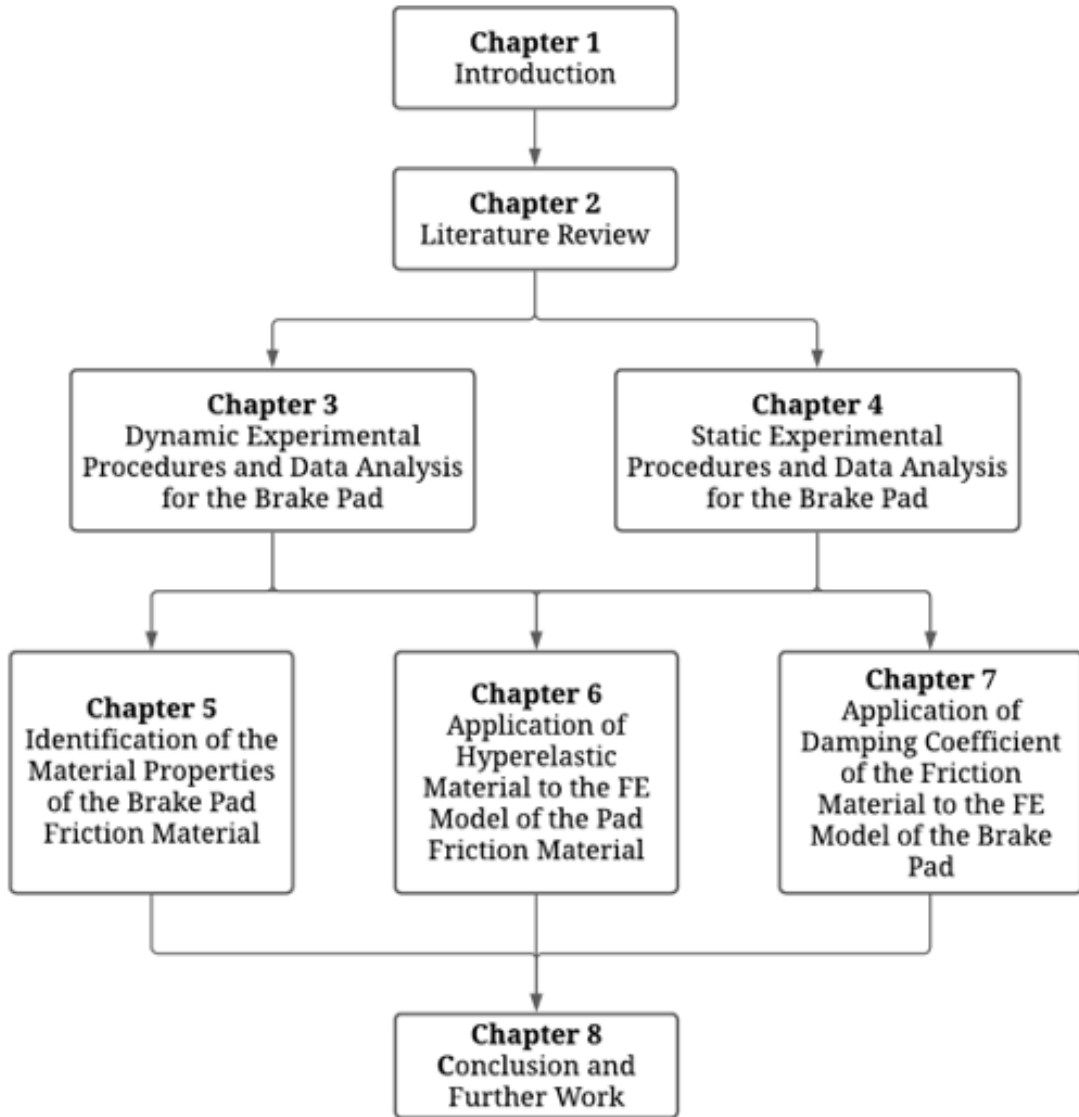
Figure 1.8 Flowchart of the thesis structure

Chapter 1 introduces the background and motivation of this project, gives the aim and objectives of the research, states the original contributions and summarises the chapter outlines of this thesis.

Chapter 2 provides a comprehensive literature review concerning mechanical properties identification of the brake pad material in different aspects: the fundamental of the brake squeal mechanisms including stick-slip vibration, sprag-slip vibration, mode-coupling vibration, and negative coefficient of

friction vs velocity slop; the fundamental theory of the Finite Element Method (FEM) and the FEM applications;

the dynamic and static experimental investigations on the brake pad; the identification categories and common identification methods; the review on the hyperelastic material concept and applications; and the damping identification methods.

Chapter 3 presents the theories of dynamic experimental analysis. The modal data for out-of-plane vibration of a plate is obtained using two different experimental methods to observe the difference between these two methods. The analysed test data are compared to find a more suitable dynamic experimental method. This selected method is then used to test a brake pad to collect reliable dynamic test data such as the frequencies, mode shapes and damping of the pad.

Chapter 4 presents the theories of analysing the static test data of the pad friction material from compression tests. The lateral changes in the strain of the pad friction material specimens were measured using the strain gauges and Digital Imaging Correlation (DIC). The experimental setups using both measuring techniques are described, and the compression test results with different measuring methods using different test specimens are observed and analysed. The suitable stress-strain measuring method was used in the identification method in chapter 5 and chapter 6 when analysing the pad as hyperelastic material in ABAQUS.

Chapter 5 proposes two methods of identifying the material properties of the pad friction material, which provides reliable analytical modal data, such as the frequencies and mode shapes, of the pad FE model. The theories of both the sensitivity approach and the optimisation approach are given in this chapter. The developed MATLAB codes are explained in detail in this chapter. Both selected model updating methods are applied to the brake pad model using the developed MATLAB programs. Both identification methods were used on a rectangular steel plate to validate the functionality of the developed program. The estimated analytical dynamic results from the updated pad material properties in the FE model were identified using both updating methods, and the dynamic and static tests data shown in chapters 3 and 4 could be used in the identification process. In the identification process, the pad friction material was assumed to be either orthotropic or transversely isotropic. The updated material properties of the pad friction material using different methods and different material types are

implemented in the pad FE model to determine the analytical frequencies and mode shapes of the pad.

Chapter 6 presents the theories of different types of Hyperelastic materials, including the isotropic and anisotropic Hyperelastic materials. Firstly, a theoretical analysis is done by applying different types of Hyperelastic materials cards to the brake pad sample in ABAQUS. Then the measured stress-strain data of the brake pad friction material from the compressibility tests are used in ABAQUS to apply the pad friction material as a Hyperelastic material.

Chapter 7 covers formulations and theories of the damping identification methods. The theoretical analysis of the damping coefficients of the pad friction material is included in this chapter. Data of the damping factors of the friction material collected from the dynamic experiments are shown in this chapter. The damping identification method is used to analyse the input damping coefficient of the friction material for the pad FE model.

Chapter 8 summarises the major findings and key conclusions of this project and provides some suggestions for future work and improvement.

Chapter 2 Literature Review

There have been many published studies on the brake pad friction material, which greatly enhances understanding of the material properties of the pad friction material. This chapter is dedicated to the literature review of this project in different aspects.

Firstly, a review of the fundamental concepts of the disc brake squeal is carried out in section 2.1. Secondly, the finite element modelling theory and applications are presented in section 2.2. Thirdly, the dynamic and static experimental investigations on the brake pad in industries are reviewed in section 2.3. Next, different identification categories and common identification methods, especially for non-isotropic, inhomogeneous, and nonlinear materials, are presented in section 2.4. Section 2.5 reviews the hyperelastic material applications, and section 2.6 provides an overview of the damping methods.

2.1 Disc Brake Squeal

Many types of research have been done to review the brake squeal mechanisms since the 1930s (Lamarque and Williams, 1938, Mills, 1939). Drum brakes were commonly used as early brake systems and therefore studied initially. However, nowadays, researchers are more focused on disc brakes as they are used more in modern road vehicles. Research on brake noise has been carried out in many different aspects:

- The fundamental instability mechanisms of brake systems will be reviewed in this section.

- The design liabilities and countermeasures are also reviewed in this section.

- The advanced computational modelling of the brake components is reviewed in section 2.2 with the fundamental concept of finite element modelling.

- A review of signal analysis and the data processing methods for the experimental data of the pad is given in section 2.3.

- The uncertainty analysis and the dissatisfaction with the model prediction will be reviewed in section 2.3.

2.1.1 The fundamental of brake squeal mechanisms

In the literature, the occurrence of the brake squeal is generally caused by four mechanisms: 1) stick-slip oscillation, 2) sprag-slip oscillation, 3) mode-coupling instability, and 4) negative relationship between friction coefficient and velocity. Ibrahim (1994) and Kinkaid et al. (2003) reviewed these mechanisms. In this section, the main concepts of these mechanisms are explained.

2.1.1.1 Stick-slip

Stick-slip vibration can occur in the brake system and our daily lives. Applications of stick-slip oscillation could contact between rubber and glass for car wiper blade (Koenen and Sanon, 2007), clutch engagement in powertrain system (Crowther et al., 2004), the stick-slip phenomenon during an earthquake (Brace, 1972), the stick-slip motion of turbine blade dampers, and many more (Pfeiffer and Hajek, 1992).

Stick-slip oscillation was introduced by Mills (1939) as a brake squeal mechanism, and the effect of velocity-dependent coefficient of friction was investigated on the drum brakes. The occurrence of stick-slip vibration between two objects is based on two discrete phenomena) two objects are in an equilibrium state with each other while a friction force is applied to the contact surface (static motion); 2) system in relative motion with each other (dynamic motion).

There are many pieces of research made with respect to the stick-slip motion. Popp and Stelter (1990) demonstrated the stick-slip motion using a violin as an example (Figure 2.1). The paper observed the chaotic and rich bifurcation behaviour of the violin associated with stick-ship motion using a simple block on a belt.
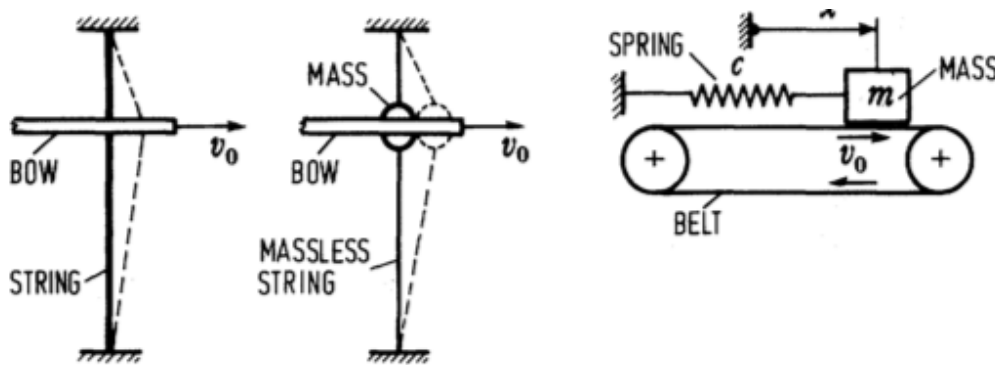
Figure 2.1 Simple models of violin string (Popp and Stelter, 1990)

Kinkaid et al. (2005) used a four-DoF system with two-dimension friction force to show that the change of the direction of the friction force could cause unstable vibration in the system. In other words, the squeal of the brake could be caused

by the stick-slip motion between the pad and disc contact surface while applying the brake pedal.

Behrendt et al. (2011) presented the numerical study of stick-slip oscillation in a brake system. A model of a brake pad with constant velocity against a rigid surface was set up using the FE modelling method. The paper demonstrated the prediction of noise and vibration generated from the brake. Assumptions were made to simplify the FE model and predict the underlying interface processes between the pad and block contact surface.

The stick-slip oscillation of the contact surface between two objects under decelerative motion was reviewed (Van De Velde and De Baets, 1996, Vielsack, 2001), and the results have shown that the stick-slip vibration can be induced under deceleration but would not appear when the system is in a steady motion.

2.1.1.2 Sprag-slip

Spurr (1961) proposed that the geometry of the brake components could be the cause of the occurrence of brake squeal. He demonstrated this theory using a simple system of three blocks (as shown in figure 2.2). In Spurr's experimental setup, only a narrow strip of the brake pads surface was in contact with the disc, and the brake squeal was caused by the deformation of the contact surface due to the normal and tangential forces in the system.

Jarvis and Mills (1963) further investigated Spurr's theory by replacing the pad components with a cantilever beam in contact with the rotating disc surface. The vibration instability was not caused by the friction change relative to the disc velocity but by the geometrical coupling between the components.
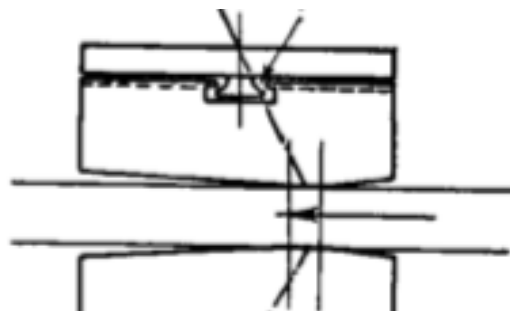
Figure 2.2 A simple model of disc brake with a disc and two pads (Spurr, 1961)

Fieldhouse et al. (2009) published a paper that showed the relationship between the position of the dynamic centre of pressure and the occurrence of the brake squeal. A unique design of disc brake with modified 12-piston opposed calliper was used in the paper to vary the dynamic centre of pressure of the disc pad contact surface. A few conclusions were drawn from this paper: 1) the leading centre of pressure is caused by 'spragging' of the system; 2) the leading centre of pressure is more likely to cause the noise between the disc/pad interface; 3) the occurrence of noise reduces when the pressure applied to the disc/pad interface increases; 4) when the pressure applied to the brake is light, the centre of pressure always tend to be leading, so the noise occurrence increases; and 5) if the centre of pressure moves radially towards the centre of the pad, the squeal occurs more often.

2.1.1.3 Mode-coupling

North (1972) used a lumped model of a disc with an eight DoF model of calliper and disc to illustrate the effects of the stiffness nonlinearity in the disc brake system. The paper proposed that the asymmetry of the stiffness matrix is a cause of the brake squeal. The basic mode-coupling concept was formed in North's paper.

Akay (2002) demonstrated the mode-coupling mechanisms using a rotating disk and a clamped beam. The numerical and experimental observation of the system suggested that noises were confined to the contact surfaces at light contact loads. This paper also reviewed the brake noise mechanisms consisting of high-frequency squeal, low-frequency squeal, groan and judder.

An undamped two-degree-of-freedom was used to demonstrate the mode-coupling instability in the paper presented by Hoffmann et al. (2002), as shown in figure 2.3.

In this paper, the change in the friction force affected the phase shifts between in- and out-of-plane motion of the system. The squeal instability occurrence depended on whether the friction-induced cross-coupling force of the system balances the corresponding cross-coupling force.
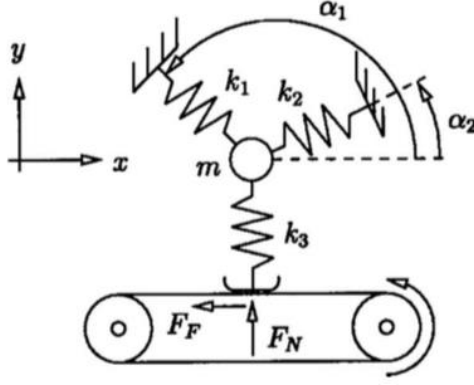
Figure 2.3 A minimal model of single mass 2-DoF system (Hoffmann et al., 2002)

In figure 2.3, a mass m constrained by three springs k_1, k_2, and k_3 can vibrate in both x and y directions. F_F and F_N are the friction and normal forces between the mass and the belt. From Coulomb's law of friction, $F_F = \mu F_N = \mu k_3 y(t)$, where μ is the friction coefficient between the contact surface.

An EoM is derived for this system (Hoffmann et al., 2002):

$$\begin{bmatrix} m & 0 \\ 0 & m \end{bmatrix} \begin{Bmatrix} \ddot{x}(t) \\ \ddot{y}(t) \end{Bmatrix} +$$

$$\begin{bmatrix} (k_1 \cos^2 \alpha_1 + k_2 \cos^2 \alpha_2 + k_3) & (k_1 \cos \alpha_1 \sin \alpha_1 + k_2 \cos \alpha_2 \sin \alpha_2) - \mu k_3 \\ (k_1 \cos \alpha_1 \sin \alpha_1 + k_2 \cos \alpha_2 \sin \alpha_2) & (k_1 \sin^2 \alpha_1 + k_2 \sin^2 \alpha_2 + k_3) \end{bmatrix} \begin{Bmatrix} x(t) \\ y(t) \end{Bmatrix} = \begin{Bmatrix} 0 \\ 0 \end{Bmatrix}$$

$$(2.1)$$

Simplifying equation (2.1) gives:

$$\begin{bmatrix} m & 0 \\ 0 & m \end{bmatrix} \begin{Bmatrix} \ddot{x}(t) \\ \ddot{y}(t) \end{Bmatrix} + \begin{bmatrix} k_{11} & k_{12} - \mu k_3 \\ k_{12} & k_{22} \end{bmatrix} \begin{Bmatrix} x(t) \\ y(t) \end{Bmatrix} = \begin{Bmatrix} 0 \\ 0 \end{Bmatrix} \qquad (2.2)$$

From the EoM shown above in equation (2.2), a MATLAB script was written to derive the frequencies and modes of the system.

After comparing the imaginary parts (frequencies) and the real parts (growth rate) of the solutions of the system at different frictional coefficients, shown in Figure 2.4, the mode coupling behaviour between x and y is observed.
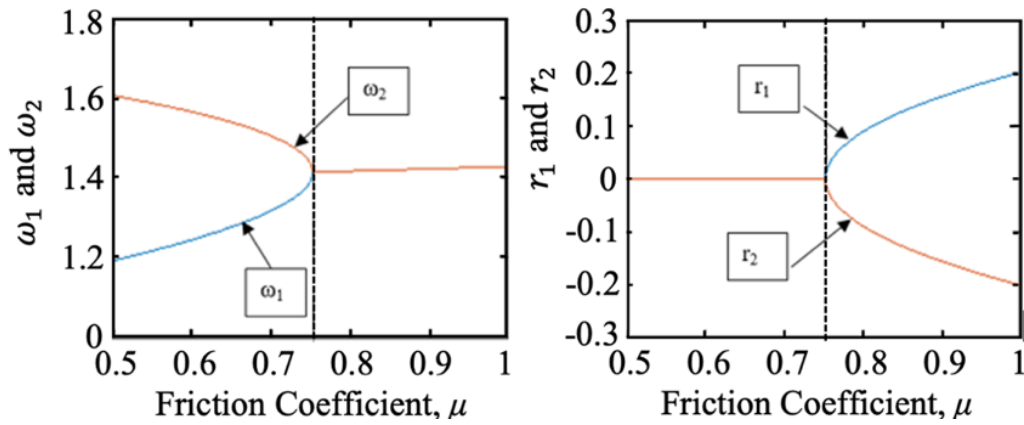
Figure 2.4 Mode-coupling phenomenon

Figure 2.4 shows that the frequencies of the system are merging together and coalesced at the point $\mu = 0.75$ (critical coefficient of friction). The bifurcation of the growth rate of the system also appears at the same point $\mu = 0.75$.

Figure 2.5 shows the time history of the system at frictional coefficient values of below ($\mu<0.75$), equal to ($\mu=0.75$) and above ($\mu>0.75$) critical frictional coefficient.
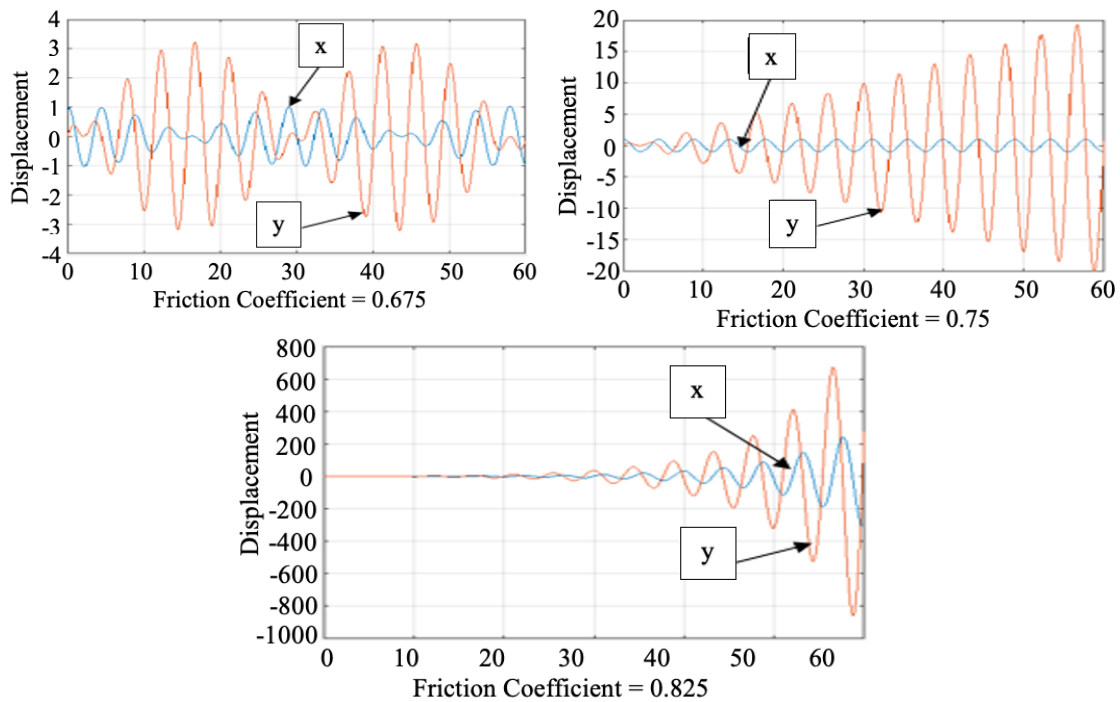
Figure 2.5 Time Series of the 2-DoF system

The top-left graph in Figure 2.5 shows that x and y oscillate at 2 (natural) frequencies coupling with each other as beating because the two frequencies of the system are different.

The top-right graph in Figure 2.5 is a special case of mode-coupling where x is uncoupled from y, but y is excited by x. This type of mode-coupling is called one-way-coupling. As x is uncoupled from y, the EoM of x becomes the EoM of undamped SDoF free vibration; hence x is oscillating harmonically. However, y is still coupled with x, and x behaves as an excitation force acting on y, and y is in an undamped SDoF force vibration system. The oscillation of y is growing linearly with respect to t.

For the last graph in Figure 2.5, x and y are coupled. However, because the two frequencies of the system coalesce into one and the growth rates of the system bifurcate, oscillations of both x and y are growing exponentially.

Chen et al. (2008) presented the contribution of time-delay of the corresponding friction force from the changing normal force in the system. The conclusion was that the change of the time delay could affect the squeal instability of the system. The paper did not show whether the time delay is due to the frictional force or the damping in the system, and this needs to be further investigated.

In the paper published by Kang et al. (2009), a simple disc brake with two pads were used to study the instability of the brake system. Both mode-coupling and negative friction-velocity slop mechanisms were considered in this paper. The modal stability index was introduced, and the FE models were used to analyse the features of the reduced-order models shown in the paper. The results showed that the modal interactions of the components could be better analysed using the FE model instead of the conventional complex eigenvalue analysis.

2.1.1.4 Negative gradient between coefficient of friction and velocity

The negative coefficient of friction vs velocity slop was proposed in many papers (Mills, 1939, D. Sinclair, 1955, Fosberry, 1961). The negative damping of the system can cause dynamic instability due to the negative friction-velocity gradient. Many types of research have been carried out regarding the negative friction-velocity relationship of the system (Yuan, 1995, Chen and Zhou, 2003).

Ouyang et al. (1998) demonstrated the effect of the negative friction-velocity relationship using a simple mass-spring-damper system in contact with an annular disc together with a frictional force. An in-plane spring-dashpot was introduced, and the results showed that when the friction is constant, a modification to the resonances can occur, which causes the negative friction-velocity relationship. The instabilities of the existing resonances are insensitive to the in-plane spring over a wide range of values.

Chen and Zhou (2003) carried out an experiment to explore the dependence of friction on the frequency and the displacement of the reciprocating sliding of the test specimen. The paper concluded that when the coefficient of friction between the contact surface is below the threshold coefficient of friction, the squeal does not occur, and the negative friction-velocity slope mechanism cannot be used to interpret the dependence of squeal formation on a threshold coefficient of friction.

2.1.2 The Design Liabilities and Countermeasures

In the paper published by Ouyang et al. (2000), a generic method was proposed to understand and analyse the brake squeal problem considering both the dynamics of the calliper, pads and mounting and the relative rotation between the pads and disc. The finite element method was used to model the calliper, mounting and pads of the brake. Some assumptions were made to simplify the system and concentrate the problem on the squeal instability due to different levels of friction, rotating speed, damping and stiffness of the contact surface. The system's assumptions are: the materials of the parts in this system are isotropic, linear, elastic and homogeneous; the disc is a thin elastic plate; the pads and the disc are in complete contact; the rotating speed is constant in the model. Based on these assumptions, a few conclusions were drawn in this paper: the stiffness of the pad material could affect the instability with a stiffer pad behaving better than a less stiff one, but the improvement is limited to a small range; the softer calliper could decrease instability, and the combination of stiffer pads and softer calliper should be considered to reduce the instability; the instability regions of the system is highly dependent on the damping of the pads and the disc; the relative rotating speed between the disc and the pads have a large impact on the dynamic instability and therefore must be taken into account accurately. These conclusions provide a better insight into the brake squeal

problem, and further investigations can be done based on the results shown in this paper.

Stender et al. (2016) used a 4 DoF system to demonstrate how the joints could have a large impact on the dynamics of the system. The MATLAB built-in optimisation method 'fmincon' was used, and two parameters were considered in the process: the stiffness of the joint and the normal load applied to the structure. The results showed that both the increase in stiffness and the decrease in the normal load could significantly reduce the vibration level of the structure.

The paper presented by Ahn et al. (2021) considered improving the shape of the brake pads to reduce the squeal of the disc brake for an urban railway vehicle. Pads with three different slot and chamfer designs were used in the paper. The FE model of the brake component was validated with the experimental data. The results showed that with suitable applications of chamfers and slots in the pad design, the contact stress between the pads and the disc could be evenly distributed, and therefore, the occurrence of the brake squeal reduces. However, in this paper, the brake pads were considered isotropic material, whereas, in reality, the pad friction material has more complicated material properties (Chapter 1 pad formulation). Therefore whether this design of the pad shape is achievable in real-life manufacturing remains a challenge.

2.2 Finite Element Method

Finite Element Modelling plays an important role in determining the pad friction material properties. The material identification methods are normally based on validating the simulated dynamic data from the updated FE model with the experimental data of the pad. An accurate FE model of the pad is required for the pad material identification methods and the brake squeal simulation.

2.2.1 Lumped Model

Von Wagner et al. (2007) reviewed numerous publications on the minimal models of disc brake squeal. The paper showed that there is still a lack of a minimal model describing the basic behaviour of disk brake squeal. Hence, a

new minimal model was proposed in this paper containing a wobbling disc in point contact with two pads.

Kruse et al. (2015) explored the relationship between the dynamic state of the joints and the stability of the system subject to friction-induced flutter. The paper demonstrated that joints play a very important role in the dynamics when it comes to the stability prediction of the system. It also illustrated the necessity of nonlinear analysis to develop the brake noise predictability method.

2.2.2 Finite Element Theory

A system with a finite degree of freedom is a discrete system, where mass, damping and elasticity are assumed to be present only at certain discrete points. For a discrete system, the mass, damping and elasticity of the system can be described numerically so that the eigenvalue and eigenvector can be calculated (Rao and Yap, 2011, Zienkiewicz et al.).

However, there are many cases, known as a distributed or continuous system, in which it is impossible to identify discrete masses, dampers or springs. These continuous systems are known as a system with an infinite degree of freedom. "In general, the frequency equation of a continuous system is a transcendental equation that yields an infinite number of natural frequencies and normal modes." (Quote from (Rao and Yap, 2011))

The numerical approximation of the solution, frequencies or mode shapes of a continuous system can be determined using the Finite Element Method. In this method, the actual structure is replaced by several elements, and each is assumed to behave as a continuous structural member called a finite element. The elements are assumed to be interconnected at certain points known as joints or nodes. (Rao and Yap, 2011, Zienkiewicz et al.)

Since it is very difficult to find the exact solution (such as the displacements) of the original structure under the specified loads, a convenient approximate solution is assumed in each finite element. The idea is that if the solutions of the various elements are selected properly, they can converge to the exact solution of the entire structure as the element size is reduced. The entire structure is made to behave as a single entity if both the equilibrium of forces at the joints and the

compatibility of displacements between the elements are satisfied (Rao and Yap, 2011).

An example is given in Figure 2.6 to understand the Finite Element Method better. The curve from the left graph can be simplified to many straight lines connected, as shown in the right graph. The length of the curve is represented by the straight lines with a small error between the true value and the estimated value. The error will decrease if a larger number of straight lines (elements) are used. If the error is small enough and is negligible (within the tolerance range), this estimated value can be considered as true value.
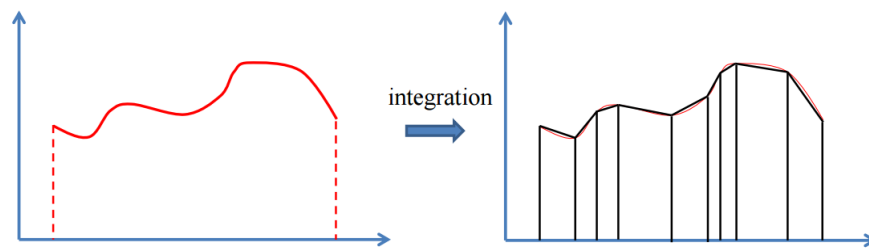
Figure 2.6 FEM example (Lallement and Inman, 1995)

A continuous system can be represented by nodal elements, with each nodal element written as a function of nodal position and nodal displacement. The sum of the nodal position of all elements is the shape function matrix $\mathbf{N}(x)$, and the sum of the nodal displacement is represented by the element nodal displacement vector $\mathbf{u}(t)$. Note that $\mathbf{N}$ is a function of x and $\mathbf{u}$ is a function of time, t.

$$u(x,t) = \mathbf{N}(x)\mathbf{u}(t) \tag{2.3}$$

where $\mathbf{N}(x) = \left[\mathrm{N}_1(x)\mathrm{N}_2(\mathrm{x})...\mathrm{N}_j(\mathrm{x}) \right]$ and $\mathbf{u}(t) = \left\{ u_1 u_2 ...u_j \right\}^{\mathrm{T}}$.

From the nodal displacement vector and shape function matrix, the Potential and Kinetic Energy of the discrete system can be calculated, as shown in equations (2.2) and (2.3). Hence the Potential and Kinetic Energy of the corresponding continuous system can be estimated.

Potential Energy:

$$E_{\mathrm{p}} = \frac{1}{2}\mathbf{u}^{\mathrm{T}}\mathbf{K}_{\mathrm{e}}\,\mathbf{u} \tag{2.4}$$

27

Kinetic Energy:

$$E_{k} = \frac{1}{2} \dot{\mathbf{u}}^{T} \mathbf{M}_{e} \dot{\mathbf{u}}$$

(2.5)

$\mathbf{K}_e$ and $\mathbf{M}_e$ are the element stiffness and mass matrices calculated from the discrete FE model. Both $\mathbf{K}_e$ and $\mathbf{M}_e$ are consist of shape function $\mathbf{N}$.

Since the Lagrange equation is a method to find the EoM of the system using energy conservation law, the EoM of the FE model would be calculated from the elements. Equations (2.4) and (2.5) below defines Lagrange's Equation.

$$L = E_{k} - E_{p}$$

(2.6)

$$\frac{\partial}{\partial t}\left(\frac{\partial L}{\partial \dot{\mathbf{u}}}\right) - \left(\frac{\partial L}{\partial \mathbf{u}}\right) = \mathbf{f}$$

(2.7)

Equation (2.6) represents a system of n differential equations, each corresponding to one of the n nodal displacements. Thus, the equations of motion of the vibrating system can be derived from equation (2.6), provided the energy expressions are available.

$$\frac{\partial}{\partial t}\left(\frac{\partial L}{\partial \dot{u}_{j}}\right) - \left(\frac{\partial L}{\partial u_{j}}\right) = 0, j = 1, 2, \ldots, n$$

(2.8)

2.2.3 Finite Element Modelling of the Brake Squeal Problem

In 1989, Liles published a paper that analyses the stability of a disc brake using the finite element modelling method. In Liles' paper, the complex eigenvalue analysis (CEA) was used to determine the squeal propensity of a disc brake.

Ouyang et al. (2005) stated that both the numerical simulation and the experimental methods are important when analysing the brake noise problems,

and further investigations were needed to include all changing parameters into the brake squeal simulation.

Trichês Júnior et al. (2008) reviewed the parameters that could influence the contact stiffness of the contact surface between the pad and the disc. The finite element software MSC. Nastran was used to simulate the dynamic behaviour of the disc brake. The parameters considered in the paper were the pressure applied to the contact surface, the friction coefficient, the temperature and the brake wear. The paper also mentioned determining the contact stiffness between the disc and pads using Young's modulus of the friction material, but there was very little investment into this determination method.

Brunetti et al. (2016) proposed a new instability index, the Modal Absorption Index (MAI), to compare the different unstable modes and identify the expected mode to become effectively unstable. A lumped model was used to simulate the unstable friction-induced vibration, and the results were presented using the transient analysis and the CEA. The MAI described in the paper compared the energy absorption capability of each mode, and the mode that absorbs more energy were found to correspond to the effective unstable frequency. Further development could be done to the extent of this approach to the brake FE model.

2.2.4 FE Modelling Software Packages

There are numerous finite element software packages available in the market; a few most well-known ones are listed here: ANSYS, COMSOL Multiphysics, ABAQUS, Altair HyperWorks, Autodesk CFD, Nastran. A limited number of papers compare the simulation results and computational costs between different FE software packages.

Jungwirth et al. (2010) compared the modelling and simulation methods in ANSYS Multiphysics 11 and COMSOL Multiphysics 3.5a regarding model order reduction. The simulation time between the two software was compared for non-reduced transient FE simulation, and model-order reduced transient simulation. The results in the paper showed that COMSOL Multiphysics 3.5a were twice faster when simulating the non-reduced transient FE model, whereas ANSYS Multiphysics 11 were ten times faster for model-order reduced transient simulation.

Ozel et al. (2011) studied the comparison between the ABAQUS and DEFORM 3D software in terms of 3D FE modelling for machining the nickel-based alloy Inconel 718. The simulation results from both software were compared with the experimental results. The predicted temperature, stress, and strain values were similar to the ABAQUS/Explicit and DEFORM 3D software.

FE software is becoming more powerful and accurate nowadays, and the software companies are putting more effort into developing and updating the software functionalities. A comparison between the dynamic simulation of the pad using ABAQUS and Nastran is made in Chapter 5.

2.3 Dynamic and Static Experimental Analysis

Both numerical simulation and experimental analysis are important when trying to understand the brake squeal problem and further investigation on the material properties of the pad friction material (Ouyang et al., 2005). The review of the dynamical and static experimental approaches are shown in this section.

2.3.1 Dynamic Experimental Studies

2.3.1.1 Introduction

Modal testing involves three main types of measuring mechanisms: the excitation mechanism, the sensing mechanism, and the data acquisition mechanism. The fundamental concept of modal testing mechanisms is explained in Maia and Montalvão e Silva (1997) and McConnell and Varoto (1995). Much of this sub-section is adapted from them. Further details of the modal testing theory are included in Chapter 3.

The excitation mechanism is to apply the input force to the system, and the excitation device can be either a shaker which is normally used to generate continuous input signals such as stepped-sine, swept-sine or random signals; or an impact hammer which applies an impulse force to the system.

The sensing mechanism is the transducers that measure the dynamic response of the structure during the experiment. The transducer can be displacement, velocity, and acceleration transducer.

Finally, the data acquisition mechanism is the analyser, which processes and develop the signals measured from the transducer. The most common algorithm used in an analyser is the Fast Fourier Transform (FFT) algorithm, which measures the Frequency Response Functions (FRFs).

Figure 2.7 shows a typical process of a dynamic test with either an exciter or an impact hammer as the input force.
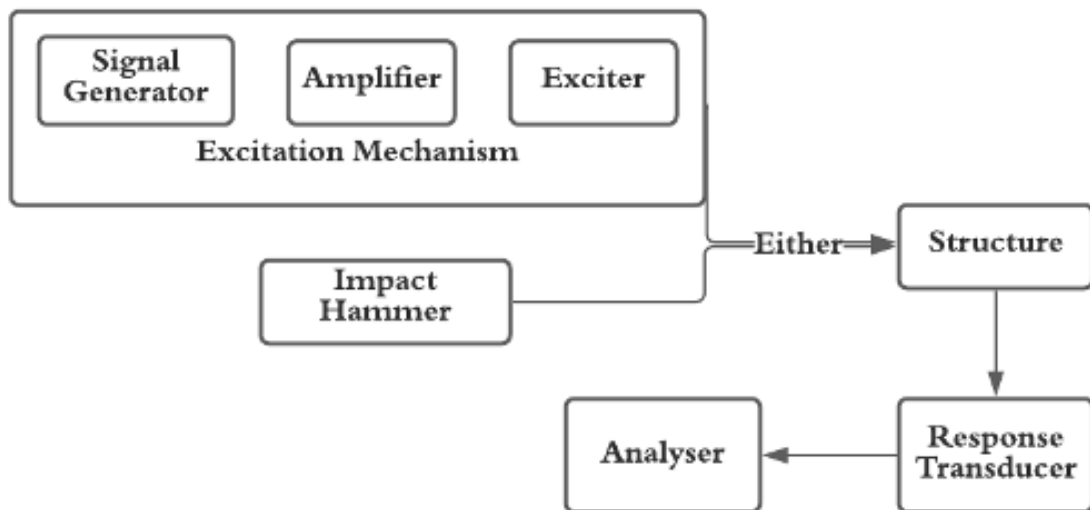
Figure 2.7 Basic modal testing structure

2.3.1.2 Applications

There are many applications of the experimental analysis of the brake system, and a few of them are reviewed below. Some of these applications were selected to review the history of the dynamic test methods, other applications were selected to gain better understanding on different types of dynamic test procedures and their use to the brake system.

Fieldhouse and Newcomb (1996) demonstrated an experimental method to examine the amplitude information of the brake system. The experiment is based on and extended from the classical holographic interferometry method. The paper showed that the directional and phase information and amplitude information could be collected.

Stanbridge and Ewins (1999) proposed a technique that uses a Laser Doppler Vibrometer (LDV) to measure the dynamic responses of a rotating disc. The out-

of-plane mode shapes of the rotating disc were calculated from the measurements of the 3D operational deflection shapes of the rotating disc.

Chen et al. (2003) published a paper that experimentally studied the squeal appearance of a disc brake under the influence of different variation conditions:

- pad damping variation,
- rotor and pad resonant frequency variation,
- disc/pad contact area and pressure variation,
- pad compressibility variation,
- variation of friction coefficient of the pad friction material,
- pad friction material elastic constants variation,
- variation of the load and operation condition during the test.

Different dynamic response measuring techniques were used in that paper, such as the accelerometer, the Laser Doppler Vibrometer, the laser holographic and pulse holographic interferometer, and the laser speckle pattern interferometer. The purpose of this paper is to minimise the influence of the different testing conditions between on-road brake squeal conditions (which include a brake suspension) and the laboratory brake testing condition (without brake suspension).

They also suggested that "The parameter measurements of the brake components should be performed before and after the on-road and laboratory tests to avoid bad data points, to gauge variation, and to trace squeal origination."

Giannini published two papers in 2006 (Giannini et al., 2006, Giannini and Sestieri, 2006) in which the squeal instability was examined through an experimental approach. The paper set up a laboratory brake of a steel disc with an attached electric motor to control the disc rotating speed, together with two brake pads held by steel beams placed on each face of the disc. The paper showed that the squeal occurrence could be repeated if correctly set up the testing conditions.

In 2008, Giannini and Massi further investigated the brake squeal instability using a similar experimental setup. The paper presented the correlation between the dynamic behaviour of the system and the length of the brake pad. A calliper consisted of two small pads with distance, d, on the same surface of the disc was used in the experiment, and d represented the characteristic length of one pad. A variable, r, is proposed in the paper, representing the ratio between the

wavelength of the considered mode and the dimension of the contact zone. The paper concluded that the occurrence of the rotating squeal is strongly correlated with the value of the ratio, r, and r could be used to classify the low-frequency (r < 0.25)and high-frequency ($r \geq 0.25$) brake squeal.

Bryant et al. (2012) presented the experimental method and results of the brake pad under dynamic squeal conditions. Several piezoelectric beams were used on the corners of the pad, and the squeal frequencies were measured. FE modelling of the pad was also made to analyse the theoretical modal information of the pad.

Quan et al. (2019) reviewed the influence of the shape of the brake pad friction material towards the noise generated during braking. A laboratory disc brake was set up, and different shapes of frictional blocks (circle, triangle and hexagon) were used to compare the rate of squeal occurrence. The 3D accelerometer was used on the friction block holder to collect the normal and tangential vibration of the system when the friction block is compressed into the disc surface. The distribution of the pad wear characteristics and the disc/pad contact pressure were also analysed in the paper, and the conclusion was that the distribution of the wear characteristics and the contact pressure could largely influence the noise level.

Many published papers were published on the disc brake squeal through dynamic experiments, and most of the researches mainly considered the friction between the brake components. The research of the influence of the brake pad material properties was limited through the dynamic experiments. Hence the static experimental approach was reviewed.

2.3.2 Static Experimental Studies

2.3.2.1 Introduction of Compression Test

In 1660, Robert Hooke discovered a linear relationship between the extension of an elastic spring and the tension applied to it. This law is later known as the law of elasticity or Hooke's law. Hooke's law state that the change in strain (deformation) of an object is in relation to the stress (force) applied to the object. (Hooke, 1678)

The change in strain of an object is defined as the change in length of an object against the original length of the object: $\varepsilon = \dfrac{\Delta L}{L}$, which can be positive (in tension) or negative (in compression) depending on the type of static test applied to the object.

As previously reviewed in chapter 1, the brake pad friction material is made of metal fibres mixed and compressed together with strong abrasives and lubricants. With such a material structure, the friction material cannot hold the tension force but is more suitable to withstand compressive force.

Compression testing is one of the most fundamental types of static testing to determine the material properties of an object. There are many techniques to find the material's behaviour under applied compressive load; using an Instron machine is the most common compression test method. The stress-strain diagram is created during the test, which is used to determine the elastic limit, proportional limit, yield point, yield strength, and compressive strength of the test specimen. (Instron)

An Instron machine measures the change in strain of the test specimen in the same direction of the stress applied to the specimen. However, to determine the material properties of a non-isotropic material, the change in strain in the directions normal to the applied stress is also needed. Hence, if the stress applied to the specimen is assumed in the vertical direction, then the change in strain in the horizontal direction must be measured and the change in strain in the vertical direction. Many techniques could be used to measure the horizontal change in strain; the techniques of using a strain gauge and using a Digital Imaging Correlation (DIC) are demonstrated below.

Strain Gauge

The change in strain of an object can be measured with several methods, and the most common method is to use a strain gauge. Since the strain gauge is glued to the measured object (Figure 2.8), the change in strain of the object surface would produce a change of the electrical resistance in the strain gauge active grid (Keil, 2017). A strain gauge can only measure the change in strain in the longitudinal direction of the grid. Hence for an orthotropic material, more than one strain gauge is needed to measure the change in strain in all directions.
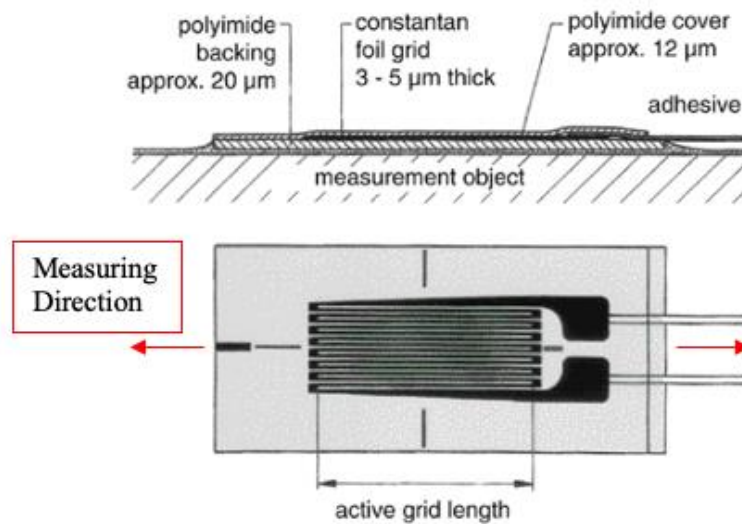
Figure 2.8 Basic design of a standard foil strain gauge (Keil, 2017)

Digital Imaging Correlation (DIC)

Digital Imaging Correlation is an innovative non-contact optical technique for measuring the strain and displacement of an object (McCormick and Lord, 2010). An example of the test setup using DIC is shown in Figure 2.9. The digital photographs of the area of interest of a test specimen are captured using the digital camera, and the change in strain and displacements are compared by tracking the blocks of pixels from the captured surface.
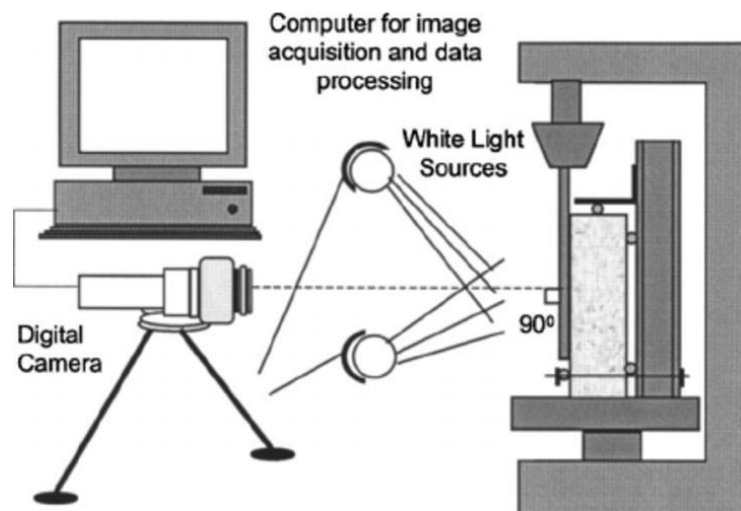
Figure 2.9 An example of the test setup using Digital Imaging Correlation (Ahmad et al., 2006)

The camera is perpendicular to a specimen with a black and white patterned measuring surface. The pattern could be naturally formed or from an applied speckle pattern. The change in surface displacement of the specimen is measured and compared with the initial undeformed specimen to build a full-field displacement measurement. (Seo et al., 2002, McCormick and Lord, 2010)

Applications of measuring the stress-strain relationship of the composite materials are shown in section 2.3.2.2 below.

2.3.2.2 Applications

The ISO 6310:2009 standard for brake lining compression test set the standard testing procedure to measure the compressibility of the brake pad lining material. Four samples were used to test the braking lining of the disc brake pads and drum brake pads. The strain gauge for measuring the accuracy of 0.01 mm reduction of thickness was attached to the sample near its centreline.

Mann et al. (2017) characterised the mechanical properties of the brake pad friction material from the compressive test using the DIC and the strain gauge. The change in strain of the specimen from the strain gauge and the DIC are compared to validate the test data. After validation, the DIC results were used to obtain the elastic and residual strain fields. The experimental data were also compared with the numerical data to validate the input elastic characterisation of the friction material.

Kumar et al. (2021) published a paper that proposed a new brake pad material with an increased heat transfer rate and better manufacturability. Different static tests were done with this proposed pad material, including hardness and compression tests. The stress-strain curve was created, showing the compressive strength of the brake pad sample. The thermal properties of the brake pad were also reviewed, and the results showed that both the mechanical and thermal properties in the developed brake pad were higher than the conventional automobile brake pads.

Saindane et al. (2021) included the fabrication and characterisation of carbon fibre based polymer composite into the brake pad friction material. Two samples of the proposed composite were manufactured with 1) plastic mould 2) mould of cast steel. The compression tests and hardness tests were done for both samples.

The paper concluded that the carbon-based polymer composite could be used as an alternative to other synthetic fibre based polymer composites.

2.4 Model Updating

As previously mentioned (Chen et al., 2003), the mechanical properties of the friction material are one of the variations that could influence the appearance of the brake squeal. Mortelette et al. (2009) also state that different types of fibres could strongly affect the rate of squeal occurrence. Five non-asbestos organics (NAO) pads with different fibre types were used to observe the impact of the mineral fibres towards brake squeal. FEM complex eigenvalue analyses correlated with the squealing frequencies from experimental results.

This section mainly focuses on identifying the determinants of non-isotropic composite materials. The identification method is based on the model updating technique, which compares the experimental data, such as the frequencies, mode shapes and damping, of the structure, and the analytical data from the FE model of the structure (Mróz and Stavroulakis, 2005).

Dorosti (2017) summarised the model updating methods into different categories (Figure 2.10 below).

There are mainly two types of model updating techniques: direct and iterative methods. Both methods aim to minimise the difference between the experimental data and the analytical results, but the direct method updates the global system matrices, and the iterative method updates the selected parameters (Lee, 2006).

The iterative model updating method can be separated to the following classes of approaches:

- The computational intelligence updating method (Marwala, 2010),
- The lease-square updating method
    - Frequency Response Function updating method (Esfandiari et al., 2010a, Sipple and Sanayei, 2014, Esfandiari et al., 2010b)
    - Modal-based updating method.

- Minimising the frequencies and mode shapes of the system (further details in section 2.4.2);
- Minimising the real-valued resonance and anti-resonance frequency residuals (D'Ambrogio and Fregolent, 2003, Jones and Turcotte, 2002);
- Minimising the complex-valued pole and zero residuals (Dorosti et al., 2018, Dorosti et al., 2017).
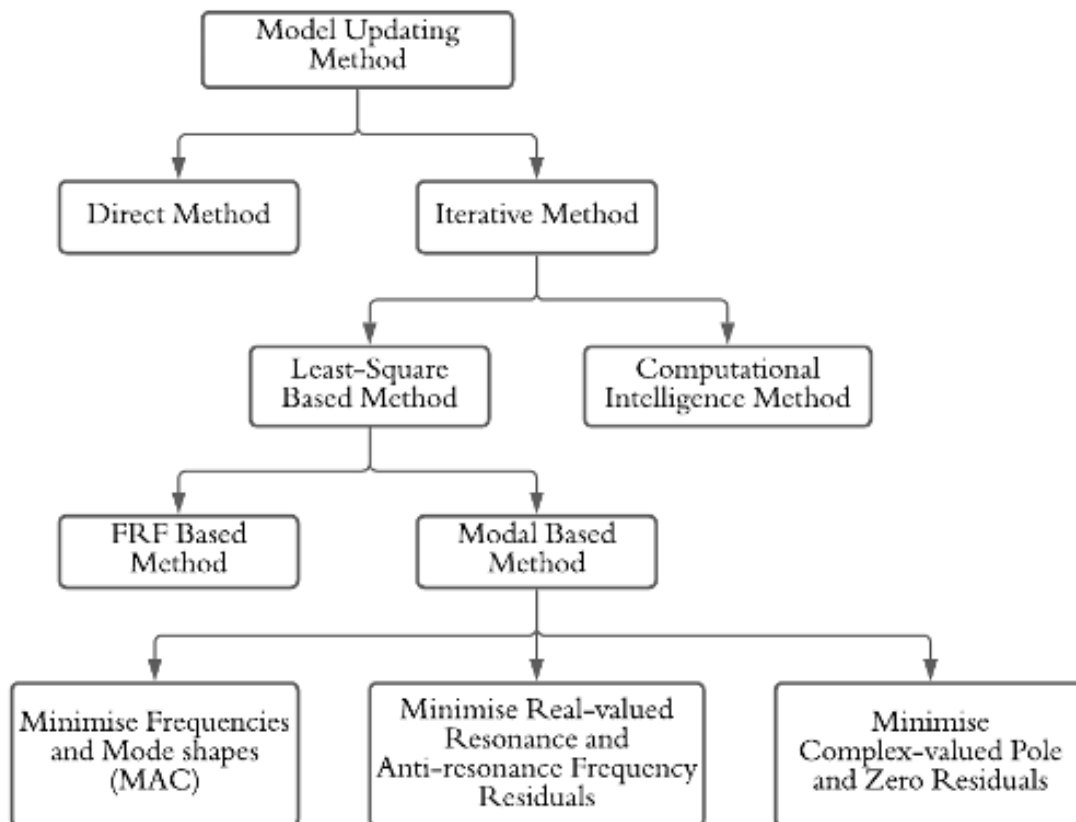
Figure 2.10 Overview of Model Updating Methods

Many papers were published on both direct model updating methods iterative model updating methods. A few of them will be selected and discussed in sections 2.4.1 and 2.4.2 below.

2.4.1 Direct Method

The direct model updating methods concentrate on updating the complete matrices (such as the mass, stiffness, damping matrices) of the structure.

Baruch (1978) proposed a direct updating method which updated the stiffness matrix of the structure while keeping the mass matrix fixed. Berman and Nagy (1983) further developed the method and updated both mass and stiffness matrices. Both methods above consists of updating one variable at a time. Wei (1990) improved on the method and updated both the mass and stiffness matrices simultaneously with the constraint of mass orthogonality and the symmetric of the updating matrices.

Fuh et al. (1984) considered the direct updating method of using the damping matrix together with the mass matrix and the constraint of orthogonality. Friswell et al. (1998) developed the method based on Fuh et al. (1984) and updated the damping and stiffness matrices with fixed mass matrix. Kuo et al. (2006) presented two algorithms updating the mass, stiffness matrices and damping, stiffness matrices. Both Carvalho et al. (2007) and Yang et al. (2016) explored a direct model updating method of an undamped system with measured modal data.

The global system matrices are needed if a direct method is used for model updating. However, it may not be possible to determine the global system matrices for a continuous system in real applications. Even if the global system matrices are determined using FE modelling, the size of the matrices could be very large, which takes much computational cost. Hence, the iterative method is used more often in the finite element model updating process.

2.4.2 Iterative Method

An iterative model updating method minimises the error between the experimental data and predicts data from the FE model by updating the desired modal parameters. The modal parameters could be physical parameters or generic parameters. In this project, the parameters which need to be identified are the material properties of the brake pad, such as the Young's Modulus, Poisson's Ratio, and Shear Modulus of the pad friction material in all directions.

The iteration method can be categorised into many sub-approaches, shown in Figure 2.10. In this section, the main focus of the updating approach would be using the frequencies and mode shapes to minimise the experimental-analytical error.

Since the research on identifying the material properties of the brake pad friction material is limited, this section mainly shows the identification of non-isotropic composite materials through the model updating method.

Nagendra and Fleury (1989) used the optimiser in the MSC/Nastran software to determine the thickness, orientation angle and material properties with laminated composite material.

Mottershead et al. (2011) published a paper reviewing the sensitivity method in FE model updating. The sensitivity analysis of the undamped frequency, undamped mode shape and input force residuals were shown in this paper. A two-DoF lumped mass undamped system was used to demonstrate the estimated results of the change in stiffness of the system using the sensitivity method. The sensitivity method was then used to determine the Young's Modulus of a Lynx helicopter airframe. The helicopter airframe was tested using 29 response points and four excitation points. The elastic moduli of the helicopter airframe were grouped into 147 groups of elements and the Young's Modulus of the most important 36 groups were determined using the sensitivity method.

Auzins et al. (2015) proposed a method that determined the Young's Modulus and Poisson's Ratio of a plate consisting of orthotropic composite material. The identified material properties were determined using the experimental frequencies and analytical frequencies from the FE model.

Elhilali et al. (2021) presented an approach to determine the most suitable natural fibre to add to the brake pad. The approach was based on the model updating method and used the static experimental data with the FE model of the pad.

2.5 Hyperelastic Material

From the compression test results of the brake pad shown in chapter 4, it can be seen that the stress-strain relationship of the friction material is nonlinear. Hence, the pad could be considered either hyperelastic or viscoelastic. The concept of

hyperelastic materials will be shown in chapter 6, and this section mainly reviews the applications and papers concerning hyperelastic materials. The viscoelastic material will be reviewed in section 2.6.

2.5.1 Introduction of Hyperelastic Models

George Green originally proposed the concept of Hyperelastic materials, and the stress-strain relationship of material could be derived from a strain energy density function. Hyperelastic materials can be classified into different models depending on strain energy density functions. Isotropic hyperelastic material models include Arruda-Boyce, Marlow, Mooney-Rivlin, Neo Hookean, Ogden, Polynomial, Van der Waals and Yeoh. Non-isotropic hyperelastic material models include Fung-Anisotropic, Fung-Orthotropic, and Holzapfel-Gasser-Ogden. (Hackett, 2018, ABAQUS, 2014)

In the past decades, many strain energy density functions were developed to investigate the mechanical behaviour of the hyperelastic material. Nowadays, hyperelastic material models are mostly used in rubber or biological tissue types of materials.

Mooney (1940) proposed a hyperelastic model characterisng rubber-like materials undergoing large strain. This model is known as the Mooney-Rivlin model and was further developed by Rivlin and Rideal (1948). A special case of the Mooney-Rivlin model is the Neo-Hookean model, which is also proposed in the paper published by Rivlin and Rideal (1948). Both the Mooney-Rivlin model and the Neo-Hookean model are special cases of the polynomial hyperelastic model.

Ogden and Hill (1972) proposed a method to correlate the theoretical and experimental results of the incompressible rubber-like material. The strain energy function was developed and validated using the test results of the rubber-like material from the tension and shear experiments. This model is later known as the Ogden material model.

Yeoh (1993) further developed a model based on the polynomial hyperelastic model (Rivlin et al., 1951), which could be used to represent the deformation of nearly incompressible, nonlinear elastic materials. This model can be considered a reduced case of the polynomial hyperelastic model.

The Arruda-Boyce hyperelastic model was published by Arruda and Boyce in 1993 (Arruda and Boyce, 1993). The deformation of rubber materials was successfully validated from the model and the experimental results.

Fung (1993) developed a hyperelastic material model, which is used to determine the mechanical properties of the preconditioned soft tissues. Fung's model considered the hyperelastic model as anisotropic or orthotropic hyperelastic materials and is largely used for biological soft tissues such as blood vessels. The mechanical properties of the biological soft tissues were also reviewed in many other papers (Holzapfel, 2000, Gasser and Holzapfel, 2002, Holzapfel and Ogden, 2003, Gasser et al., 2006).

2.5.2 Applications

In recent years, more researchers have focused on developing hyperelastic material models and applying hyperelastic models to different applications.

Hajhashemkhani and Hematiyan (2015) determined the material properties of hyperelastic materials considered both isotropic (Mooney-Rivlin) and anisotropic (Holzapfel) hyperelastic models. The FE model of a polyvinyl alcohol sample was built in ABAQUS to validate with the tension test data, and the material properties were determined using the inverse analysis and iterative process.

Cai et al. (2016) proposed a new model determining the deformation of the incompressible fibre-reinforced anisotropic hyperelastic materials. The strain energy function was proposed and validated using the uniaxial tension and shear tests. The model was based on the Mooney-Rivlin model and the polynomial hyperelastic model.

Rugsaj and Suvanjumrat (2018) determined the appropriate hyperelastic material model of the FE model of a non-pneumatic tire using ABAQUS. The tensile and compressive tests were performed, and the stress-strain relationship of the material was found. The software ABAQUS was used to predict the suitable hyperelastic material model of the tire from the compression and tensile test results. Huh et al. (2019) also used the ABAQUS FE model and static test results to determine the suitable hyperelastic model of aortic wall tissues.

42

2.6 Damping

2.6.1 Introduction of Damping Models

The vibration of a system can be classified as undamped vibration of damped vibration. If no energy is lost during cyclic oscillation, the system is an undamped vibration system. If the energy is lost or dissipated during the oscillation, it is a damped system (Rao, 2017).

The main feature of a vibration system is the cyclic transformation between the potential and kinetic energy, which is associated with the inertial and elastic properties of the system. The mass and stiffness discrete elements represent the mathematic model of an undamped system.

Another aspect that should be considered in the dynamic behaviour of a vibration system is the energy lost or dissipation in the system, which is the damping force.

"A damper is is assumed to have neither mass nor elasticity, and damping force exists only if there is relative velocity between the two ends of the damper." (Quote from Rao (2017), p.45)

The damping in the system can be modelled as the following types:

- Material Damping: The energy is dissipated and absorbed by the material. The material damping is also considered as the internal damping in the system.
- Viscous Damping: The system is vibrating in a fluid medium such as air or oil, and the energy lost in the system is caused by the residence between the fluid and the system.
- Coulomb Damping: The damping force is caused by the friction force between rubbing surfaces.

Many different theories represent the mathematical models of the damping force in the vibration system.

Bessel (1828) observed the oscillation of a pendulum in air and theoretically concluded that it is necessary to take the inertia of the air into account when calculating the motion of the pendulum (Stokes, 1850).

Poisson (1831) also considered the oscillation of a pendulum in the air. In his paper, the equation of motion of an elastic fluid was used and simplified by neglecting the insensible quantities. The found from Poisson and Bessel were similar, and the conclusion was that the time of vibration of the pendulum in a fluid is affected by the density of the fluid as well as its inertia..

Stokes (1850) derived the equation of motion of the pendulums, which considered the vis viva lost in consequence of internal friction. Stokes extended from Bessel's research and considered the friction in the wire supporting the sphere.

Maxwell (1866) measured the time of the torsional vibration of three disks, each placed between two parallel fixed disks with a small but measurable distance. The coefficient of viscosity of air and other gases were measured from the experiment proposed by Maxwell.

In 1867, Maxwell proposed a viscoelastic material in which a purely elastic spring and a purely viscous damper (dashpot) are connected in series. The Maxwell model is generalised by Wiechert, where several Maxwell elements were connected in parallel (Wiechert, 1889, Wiechert, 1893). This generalised Maxwell model is also known as the Maxwell-Wiechert model, the most general form of a linear model for viscoelasticity.

Another linear viscoelasticity model, which is often mentioned together with the Maxwell model, is the Kelvin-Voigt model, where the elastic spring is in parallel with the viscous damper instead.

Maxwell Model

The Maxwell model can be represented by a purely viscous damper and a purely elastic spring connected in series. The model can be represented by:

$$\frac{\dot{\sigma}}{E} + \frac{\sigma}{\eta} = \dot{\varepsilon}$$

where σ is the stress, ε is the strain that occurs under the given stress, E is the elastic modulus of the material and η is the viscosity of the material.
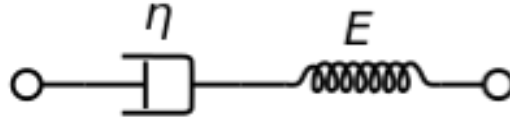
Figure 2.11 Maxwell Model (Prandina, 2010)

Kelvin-Voigt Model

The Kelvin-Voigt model can be represented by a purely viscous damper and purely elastic spring connected in parallel. The model can be represented by:

$$\sigma = E\varepsilon + \eta\dot{\varepsilon}$$
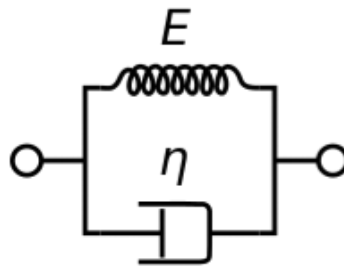
Figure 2.12 Kelvin-Voigt Model (Prandina, 2010)

Lord Rayleigh developed the damping matrix in 1878, where the coefficient of the quadratic energy dissipation function was grouped into a symmetric matrix (Rayleigh and Lindsay, 1898). The well-known proportional damping (or Rayleigh's damping) was also proposed. The proportional damping is viscous damping, where the damping matrix is proportional to a linear combination of the mass and stiffness matrices.

2.6.2 Applications

Two types of damping could be considered when determining the influence of damping in a disc brake system: the frictional damping between the brake disc and pad; and the material damping of the pad friction material.

Mottershead et al. (1997) examined and compared damping effects in the disc and pad using a model with a stationary angular disc and a pad rotating at a constant speed. Both subcritical and supercritical speeds were considered in the

numerical studies, and the effects of the mass, stiffness and damping of the pad were examined with respect to the stability of the vibration of the system. The paper concluded that both disc and pad damping influence stabilising the system at subcritical speeds.

Bajer et al. (2004) proposed that the inclusion of friction-induced damping have a significant influence on the predictions of the squeal in the disc brake system. A front disc brake system which consists of the calliper, rotor, piston, and pads, was used, and the numerical simulation and experimental results were analysed. The inclusion of the positive/negative friction-induced damping in the CEA of the brake can improve the over/under prediction of the brake squeal stability.

Kirillov (2004) developed a theory that quantitatively and qualitatively explained the destabilisation paradox of a general non-conservation system with weak damping and gyroscopic forces. The destabilisation paradox means that the non-uniform distribution of damping can reduce the stability of the system, even though the general function of the damping is to stabilise the system.

Hervé et al. published two papers seperately in (2008) and (2009) which observed the occurrence of the destabilisation paradox in the instability of clutch squeal noise. The linearised and nonlinear 2-DoF systems were considered in these two papers. The effect of the damping and the actions of the gyroscopic and circulatory were investigated.

Úradníček et al. (2021) included material-dependent damping into the disc brake FE model, which analyses the system instability prediction due to damping. Both simplified and complex disc brake models were used. This paper proposed a method that defines specific damping for each component in the brake system to achieve a non-proportional damping matrix.

2.7 Summary

This chapter reviewed the fundamental brake squeal mechanisms, including the stick-slip, sprag-slip, mode-coupling and Negative friction-velocity gradient mechanisms.

The concept of finite element modelling and the FE modelling applications of the disc brake was presented in section 2.2.

The introductions and applications of the dynamic and static experimental investigations on the disc brake system were reviewed in section 2.3.

Section 2.4 included different identification categories and common identification methods and the application of identification methods on the brake squeal problem.

The introduction of Hyperelastic material and different Hyperelastic models and their application in recent years were reviewed in section 2.5.

In section 2.6, the concept of different damping models and the effects of damping-induced instability in the brake system was reviewed.

Chapter 3 Dynamic Experimental Procedures and Data Analysis

The properties of brake pad friction materials can be determined from either the static experimental data or the dynamic experimental data. This chapter presents the fundamental theory of dynamic experimental analysis, and the main theory in this section is adapted from Maia and Montalvão e Silva (1997).

In Section 3.2, the modal data for out-of-plane vibration of a thin rectangular plate is obtained using two different experimental methods, and the difference between these two methods is observed. The analysed test data are compared to find out a more suitable dynamic experimental method. This selected method is then used to test a brake pad to collect reliable dynamic test data such as the frequencies, mode shapes and damping of the pad. These modal data are used in the identification methods to determine the brake pad's material properties.

3.1 Introduction

Experimental modal analysis plays an essential role in determining accurate modal test data of a specimen or a structure. There are different modal testing methods to acquire sufficiently accurate sets of Frequency Response Functions (FRFs). Using the measured sets of FRFs, modal properties such as a specimen's frequencies, mode shapes and damping factors can be obtained.

The available signal processing methods for modal analysis are:

- Single-Input Single-Output (SISO) Analysis
- Single-Input Multi-Output (SIMO) Analysis
- Multi-Input Multi-Output (MIMO) Analysis

In section 3.1.1 below, the SISO analysis is used to demonstrate the principle of an FRF calculation, which is used to calculate each measurement signal in a set of FRFs in SIMO and MIMO analysis.

3.1.1 The Frequency Response Function (FRF)

3.1.1.1 Fourier Analysis

The Frequency Response Function (FRF) is a fundamental measurement that isolates an object's inherent dynamic properties. Experimental modal parameters such as frequency, damping, and mode shape are also obtained from a set of FRF measurements. An FRF measurement describes the input-output relationship between a single input DOF, and a single output DOF is shown in equation (3.1) below.

Consider an equation of motion of a single-degree-of-freedom (SDOF) system subject to a general excitation force $f(t)$:

$$m\ddot{x}(t) + c\dot{x}(t) + kx(t) = f(t) \tag{3.1}$$

Where m, c, k are the mass, damping, and stiffness of an SDOF system; $x(t)$ is the corresponding response of the system. Both $x(t)$ and $f(t)$ are time-dependent.

Dynamic signals can be classified into deterministic signals, each of which can be described as a function of time. Since random signals cannot be described as a deterministic function of time, some assumptions must be made to simplify random signals, which can be processed in the Fourier analysis. In this paper, random signals will not be considered, and the assumption is that the measured signals are deterministic.

Deterministic signals are divided into periodic signals and transient signals. A periodic signal repeats itself after a period (e.g., in a dynamic test of a system using a shaker as the input excitation), and a transient signal is a signal that only lasts for a short period (e.g., in a dynamic test of a system using an impact hammer as the input excitation).

For a dynamic test that applies a periodic excitation to a system that leads to a periodic response, the Fourier series can present both the input and output signals. Equation (3.2) shows the Fourier series of any signal $f(t)$:

$$f(t) = a_0 + 2\sum_{n=1}^{\infty} (a_n \cos\frac{2n\pi t}{T} + b_n \sin\frac{2n\pi t}{T}) \tag{3.2}$$

where a_0 is the mean value of the signal over a period T; a_n and b_n can be evaluated as:

$$a_n = \frac{1}{T}\int_{-\frac{T}{2}}^{\frac{T}{2}} f(t)\frac{e^{(i2\pi n\frac{t}{T})} + e^{(-i2\pi n\frac{t}{T})}}{2} dt \tag{3.3}$$

$$b_n = \frac{1}{T}\int_{-\frac{T}{2}}^{\frac{T}{2}} f(t)\frac{e^{(i2\pi n\frac{t}{T})} - e^{(-i2\pi n\frac{t}{T})}}{2} dt \tag{3.4}$$

From equations (3.3) and (3.4), the Fourier series from equation (3.2) can be written in the exponential form:

$$f(t) = \sum_{n=-\infty}^{\infty} \frac{1}{T}(\int_{-\frac{T}{2}}^{\frac{T}{2}} f(\tau)e^{-i2\pi n\frac{\tau}{T}} d\tau)e^{-i2\pi n\frac{t}{T}} \tag{3.5}$$

When the input excitation applied to the system is a transient signal, it can be assumed that it is a periodic signal with an infinite period. As $T = \infty$, $1/T = \square\omega^{\mathrm{f}} \rightarrow d\omega^{\mathrm{f}}$ and $n/T = n\square\omega^{\mathrm{f}} \rightarrow \omega^{\mathrm{f}}$. Equation (3.5) is now written as:

$$f(t) = \int_{-\infty}^{+\infty} F(\omega^{\mathrm{f}}) e^{i2\pi\omega^{\mathrm{f}}t} d\omega^{\mathrm{f}} = \frac{1}{2\pi} \int_{-\infty}^{+\infty} F(\omega) e^{i\omega t} d\omega \tag{3.6}$$

$$F(\omega^{\mathrm{f}}) = \int_{-\infty}^{+\infty} f(t) e^{-i2\pi\omega^{\mathrm{f}}t} dt \quad \text{and} \quad F(\omega) = \int_{-\infty}^{+\infty} f(t) e^{-i\omega t} dt \tag{3.7}$$

where ω^{f} is the frequency in Hertz, [Hz], and can be converted to the frequency ω in radius per second, [rad/s]: $\omega^{\mathrm{f}} = \omega\!\!\Big/\!\!2\pi$

Equations (3.6) and (3.7) are a pair of Fourier integrals that transforms a time-domain signal to and from a frequency-domain signal.

The same Fourier analysis can be applied to arbitrary output functions $x(t)$ and form a similar equation:

$$x(t) = \frac{1}{2\pi} \int_{-\infty}^{+\infty} X(\omega) e^{i\omega t} d\omega \tag{3.8}$$

$$X(\omega) = \int_{-\infty}^{+\infty} x(t) e^{-i\omega t} dt \tag{3.9}$$

The FRF calculation $H(\omega)$ of an SDOF system is obtained as:

$$H(\omega) = \frac{X(\omega)}{F(\omega)} \tag{3.10}$$

3.1.1.2 The Laplace Transform

The Laplace transform of a function $x(t)$ is defined as:

$$X(s) = \mathsf{L}\{x(t)\} = \int_{0}^{+\infty} x(t) e^{-st} dt \tag{3.11}$$

The equation of motion of an SDOF system shown in equation (3.1), the Laplace transform of equation (3.1) is defined as:

$$\mathsf{L}\{m\ddot{x}(t) + c\dot{x}(t) + kx(t)\} = \mathsf{L}\{f(t)\} \tag{3.12}$$

$$m(s^2 X(s) - sx(0) - \dot{x}(0)) + c(sX(s) - x(0)) + kX(s) = F(s) \tag{3.13}$$

Rearranging equation (3.13)

$$(ms^2 + cs + k)X(s) = F(s) + m\dot{x}(0) + (ms + c)x(0) \tag{3.14}$$

where $x(0)$ and $\dot{x}(0)$ are the initial displacement and velocity of the system. If the initial conditions are assumed to be zero, then the system transfer function is defined as:

$$\frac{X(s)}{F(s)} = H(s) = \frac{1}{ms^2 + cs + k} \tag{3.15}$$

If the system includes damping, then the roots of the denominator of equation (3.15) are s_1 and s_1^* which are the poles of the transfer function.

$$H(s) = \frac{A}{(s - s_1)} + \frac{A^*}{(s - s_1^*)} \tag{3.16}$$

A and A^* are the complex conjugates that are defined as the residues of the transfer function. The FRF is obtained by evaluating the transfer function in the frequency domain:

$$H(\omega) = \frac{X(\omega)}{F(\omega)} = \frac{1}{(k - \omega^2 m) + \mathrm{i}\omega c} \tag{3.17}$$

3.1.2 FRF Estimators and Coherence of the System

3.1.2.1 FRF Estimators

A few advantages of using multi-input excitations or multi-output responses when obtaining a structure's modal properties. SISO modal testing may not

excite all modes if the exciting input point is close to the nodal point for some particular modes, whereas a number of modes can be excited with MIMO testing. MIMO testing can also extract the structure's mode shapes, whereas SISO can only obtain the frequencies. The mode shapes of a structure are essential when updating a structure's FE model.

Extraneous noise can be presented in both the input excitation and the output response in the FRF measurements. Three types of estimators can be used to remove random noise and nonlinearities (distortion) from the FRF estimates. The estimators would affect how the data is fit and how much each data point is adjusted to create the best fit.

- Assume noise in the output ($H_1(\omega)$): This FRF estimator assumes random noise and distortion appear in the output signals but not in the input signals. The H_1 estimator tends to underestimate the FRF if there is noise in the input. The measured output vector of a MIMO system that uses the H_1 estimator would consist of the output vector and the output noise vector. Such vector is written as:

$$\underline{X}^m(\omega) = \underline{X}(\omega) + \underline{N}^x(\omega) = \mathbf{H}_1(\omega)\underline{F}(\omega) + \underline{N}^x(\omega) \qquad (3.18)$$

- Assume noise in the input ($H_2(\omega)$): This FRF estimator assumes random noise and distortion sum to the input signals, but not the system's output signals. This estimator tends to overestimate the FRF if there is noise on the output. The measured output vector of the MIMO system that uses the H_2 estimator would consist of the measured input vector, which consists of the input vector and the input noise vector. Therefore, the measured input vector and output vector is written as:

$$\underline{F}^m(\omega) = \underline{F}(\omega) + \underline{N}^f(\omega)) \qquad (3.19)$$

$$\underline{X}^m(\omega) = \mathbf{H}_2(\omega)\underline{F}(\omega) = \mathbf{H}_2(\omega)(\underline{F}^m(\omega) - \underline{N}^f(\omega)) \qquad (3.20)$$

- Assume noise in both the Input and Output ($H_v(\omega)$): This FRF estimator assumes that random noise and distortion are summing into both the system's input and output responses. This H_v estimator provides the best

overall estimate of the frequency function but requires more computational time than the other two. The measured output vector that uses this estimator would consist of the measured input vector and the output noise vector.

$$\underline{X}^m(\omega) = \mathbf{H}_v(\omega)(\underline{F}^m(\omega) - \underline{N}^f(\omega)) + \underline{N}^x(\omega) \qquad (3.21)$$

3.1.2.2 Coherence

Consider a SISO measurement system, the $H_1(\omega)$ estimator normalizes the input signal, and the $H_2(\omega)$ estimator normalizes the output signal. If there is no noise in the input or output during the test, the result should be the same whether using the $H_1(\omega)$ estimator or the $H_2(\omega)$ estimator. Hence, the ratio of the $H_1(\omega)$ estimator and the $H_2(\omega)$ estimator should indicate the quality of the FRF analysis of a given input-output spectrum.

$$\frac{H_1(\omega)}{H_2(\omega)} = \gamma^2(\omega) \qquad (3.22)$$

The ratio $\gamma^2(\omega)$ is called the ordinary coherence function. It is a normalized correlation coefficient between the measured input force signals and the output response signals evaluated at each frequency. This ratio should be larger than 0 but smaller or equal to 1. When the ratio is smaller than 1, it indicates that there could be extraneous noise in the input or the output signals.

3.1.3 Modal Assurance Criterion (MAC) Between Mode Shapes

The Modal Assurance Criterion (MAC) concept is that if a linear relationship exists between two arbitrary complex vectors $\mathbf{a}$ and $\mathbf{b}$, the MAC value will be 1. Otherwise, if the two selected vectors are linearly independent, the MAC value will be small (close to 0).

$$MAC_{a,b} = \frac{|\mathbf{a}^T \cdot \mathbf{b}|}{(\mathbf{a}^T \cdot \mathbf{a})(\mathbf{b}^T \cdot \mathbf{b})}$$

$$(3.23)$$

The MAC calculation is useful in comparing two arbitrarily scaled mode shape vectors, and similar mode shapes will have a high MAC value. Mode shapes used in the comparison can originate from a Finite Element Analysis or an experimental modal analysis. The MAC pair modes shapes derived from analytical models with those obtained experimentally. A MAC matrix is created that compares every mode shape vector of the FE model with every mode shape vector of the experimental results.

Assume that the number of experimental mode shapes is n^m and the number of analytical mode shapes from the FE model is n^{FE}. Then the experimental mode shape matrix $\mathbf{\Phi}^m$ is obtained as:

$$\mathbf{\Phi}^m = \{\varphi_1^m, \varphi_2^m, ..., \varphi_{n^m}^m\}$$

$$(3.24)$$

and the analytical mode shapes matrix from the FE model $\mathbf{\Phi}^{FE}$ is obtained as:

$$\mathbf{\Phi}^{FE} = \{\varphi_1^{FE}, \varphi_2^{FE}, ..., \varphi_{n^{FE}}^{FE}\}$$

$$(3.25)$$

The MAC matrix that calculates $\mathbf{\Phi}^m$ and $\mathbf{\Phi}^{FE}$ is:

$$MAC_{\phi^m, \phi^{FE}} = \sum_{i=1}^{n^m} \sum_{j=1}^{n^{FE}} \frac{\left|\left(\varphi_i^m\right)^T \cdot \left(\varphi_j^{FE}\right)\right|}{\left(\left(\varphi_i^m\right)^T \cdot \left(\varphi_i^m\right)\right) \cdot \left|\left(\varphi_j^{FE}\right)^T \cdot \left(\varphi_j^{FE}\right)\right|}$$

$$= \begin{pmatrix} \dfrac{\left|\left(\varphi_1^m\right)^T \cdot \left(\varphi_1^{FE}\right)\right|}{\left(\left(\varphi_1^m\right)^T \cdot \left(\varphi_1^m\right)\right) \cdot \left|\left(\varphi_1^{FE}\right)^T \cdot \left(\varphi_1^{FE}\right)\right|} & \cdots & \dfrac{\left|\left(\varphi_1^m\right)^T \cdot \left(\varphi_{n^{FE}}^{FE}\right)\right|}{\left(\left(\varphi_1^m\right)^T \cdot \left(\varphi_1^m\right)\right) \cdot \left|\left(\varphi_{n^{FE}}^{FE}\right)^T \cdot \left(\varphi_{n^{FE}}^{FE}\right)\right|} \\ \vdots & \ddots & \vdots \\ \dfrac{\left|\left(\varphi_{n^m}^m\right)^T \cdot \left(\varphi_1^{FE}\right)\right|}{\left(\left(\varphi_{n^m}^m\right)^T \cdot \left(\varphi_{n^m}^m\right)\right) \cdot \left|\left(\varphi_1^{FE}\right)^T \cdot \left(\varphi_1^{FE}\right)\right|} & \cdots & \dfrac{\left|\left(\varphi_{n^m}^m\right)^T \cdot \left(\varphi_{n^{FE}}^{FE}\right)\right|}{\left(\left(\varphi_{n^m}^m\right)^T \cdot \left(\varphi_{n^m}^m\right)\right) \cdot \left|\left(\varphi_{n^{FE}}^{FE}\right)^T \cdot \left(\varphi_{n^{FE}}^{FE}\right)\right|} \end{pmatrix}$$

$$(3.26)$$

A structure's FE mode shapes are correlated to the structure's experimental mode shapes using the MAC correlation method. The extracted FE mode shape nodal location must be close to the experimental measurement locations to calculate the correct MAC value. Further details of the FE model shape point determination is in Chapter 5.

3.2 Modal Testing Procedure and Results of a Rectangular Plate

An excitation source like an instrumented hammer or electromagnetic shaker feeds energy into the structure in the modal testing process. Then, the structure responds to the source according to the excitation amplitude and frequency range. The structure's response may be collected as displacement, velocity or acceleration of measured nodes. Several sharp peaks in the FRF diagram are usually observed for a lightly damped structure. A higher level of damping leads to a flatter peak. These peaks indicate the locations of natural frequencies of the structure within the excitation frequency range.

Two testing methods are used to test a rectangular plate to demonstrate both methods and find a suitable method to test the brake pad. These two methods are:

1. The Accelerometer/Force FRF Test Method: to extract the out-of-plane modal data, one accelerometer is placed onto the plate, or the pad and the system are excited with an impact hammer at different points. This method is a MISO testing method as only one accelerometer is used, and the Accelerometer position remains unchanged while the excitation point changes.
   For the Accelerometer/Force FRF Test Method, the LMS test lab is used for conducting modal tests and analyses on the pad with an instrumented hammer as the input source and the accelerometer as the output source. The LMS test lab is a well known software which allows user to do dynamic test, analysis test data and generate reports. LMS uses a very well-known algorithm for post-processing of the data: Polymax. This algorithm fits a mathematical function on the collected data and produces the FRF of the test data. Polymax indicates stable poles of the fitted mathematical function, which are the frequencies of the structure.
2. The Velocity/Force FRF Test Method uses the Laser Doppler Vibrometer to record the vibratory signal while the plate is excited with the impact

hammer. A Laser Doppler Vibrometer (LDV) is a scientific instrument used to make non-contact vibration measurements of a surface. The output of an LDV is generally a continuous analogue voltage that is directly proportional to the target velocity component along the direction of the laser beam. This test method is a SIMO testing method where the excitation point remains the same while the LDV measures each point in the system that the user defines. The Velocity/Force FRF Test Method uses Polytec software for measuring the frequencies and deflection shapes of the plate and the pad.

3.2.1 Experiment Setup

The modal testing method was initially studied using a thin rectangular steel plate. The thin rectangular plate (shown in Figures 3.1, 3.2 and 5.6) was used to study two types of testing methods, the Acceleration/Force FRF method and the Velocity/Force FRF method. The size of the plate is 153mm (height) $*$ 305mm (width) $* 3.06\text{mm}$ (thickness), and the density of the plate is assumed to be constant throughout the plate, which is calculated from the mass and volume of the plate: $7885.44\,\text{kg/m}^3$. The plate is tested under free-free conditions, and the number of exciting points is different for the two testing methods. The plate is made of mild steel which is selected because it is a similar material to the backplate of the pad. Hence the test results could be used to calibrate and verify the steel backplate.

The first test is done using the Acceleration/Force FRF method (as shown in Figure 3.1). There are 77 exciting points, and a 1D accelerometer is positioned behind the plate at point 77 on the grid to measure the plate's out-of-plane frequencies and mode shapes. Each marked point is excited three times to collect an average and reduce the noise of a measurement.

57
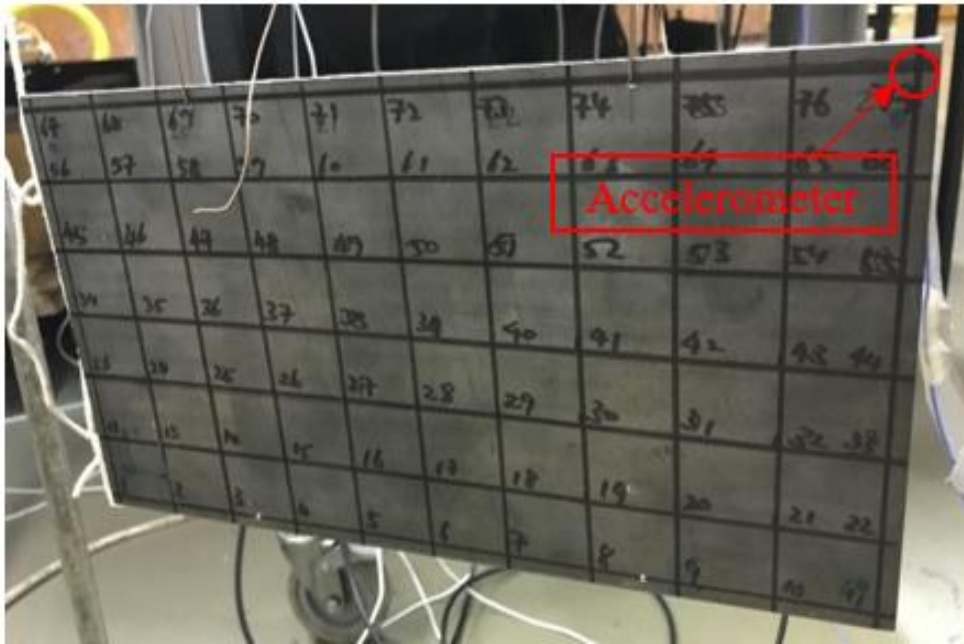
Figure 3.1 Modal test set up for the plate using an accelerometer
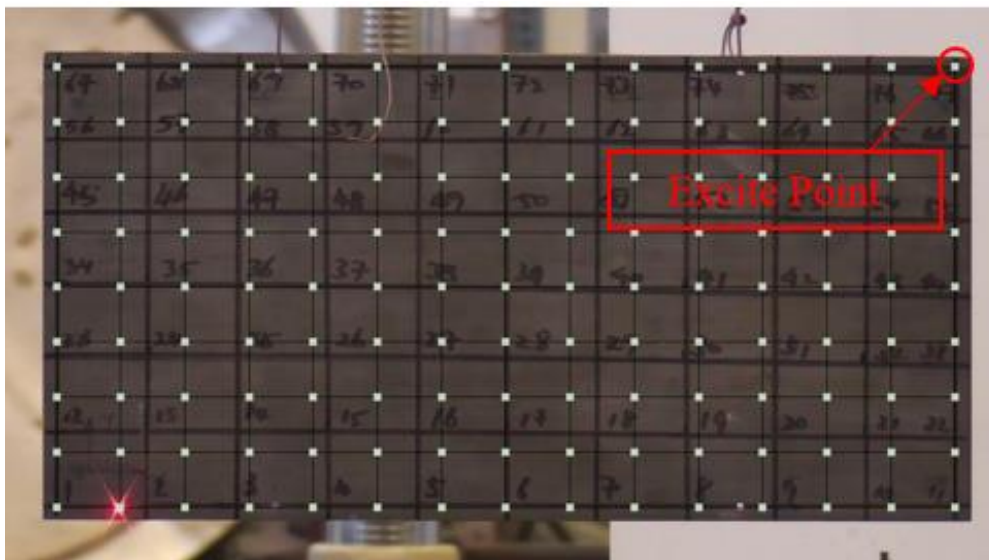
Figure 3.2 Modal test set up for the plate using a laser vibrometer

The second test was done using the Velocity/Force FRF method, a 1D laser vibrometer is used to measure the plate's out-of-plane frequencies and mode shapes, and the number of testing points is 135. This test's input excitation point is set up at the same location as the accelerometer from the previous test, and point 1 from this test is also at the same location as the previous test, so the coherence at point 1 can be compared between both tests as the input and output

signal location is the same. For this test, each point is also tested three times to reduce the negative effect of the measured signals' noise.

3.2.2 Data Analysis

Table 3.1 shows the results of the frequencies of the plate from both tests. The plate is tested to measure the first ten frequencies after 1000Hz. This range is chosen to observe the plate test results, such as the frequency, mode shape and the coherence from both tests in the higher frequency range because the pads frequencies are generally 1000Hz and above. The H_v FRF estimator is used for the FRF measurements in both tests as there could be noise in both input excitation and output response during the test. The plate is excited manually with an impact hammer, and each point is measured three times to reduce the error in the test.

Table 3.1 Comparisons between natural frequencies find from two tests

Mode Number	Natural Frequencies [Hz]		Relative Difference between Acceleration/Force and Velocity/Force Methods Test Data [%]
	Acceleration/Force FRF method	Velocity/Force FRF method	
1	1166	1170	0.34
2	1308	1313	0.34
3	1587	1588	0.03
4	1642	1652	0.60
5	1920	1924	0.20
6	1989	1994	0.24
7	2105	2119	0.69
8	2167	2174	0.29
9	2389	2397	0.33
10	2420	2426	0.22
Maximum Relative Error:			0.69

The difference between the plate's test frequencies found from the Acceleration/Force FRF method and the Velocity/Force FRF method is very small (the maximum relative error is less than 1%) and can be neglected. However, if the noise between the two tests methods is compared, the difference is large.

Figures 3.3 and 3.4 show the coherence measurement at point 1 on the grid for the Acceleration/Force FRF test and the Velocity/Force FRF test. The diagrams show that the Velocity/Force FRF test has a larger noise level than the Acceleration/Force FRF test. Due to the large output noise during the Velocity/Force FRF test, these results could occur. The Amplitude in Figure 3.3 and 3.4 is normalised and calculated based on equation 3.16 and 3.17. Hence there is no unit for the Amplitude shown in these figures.
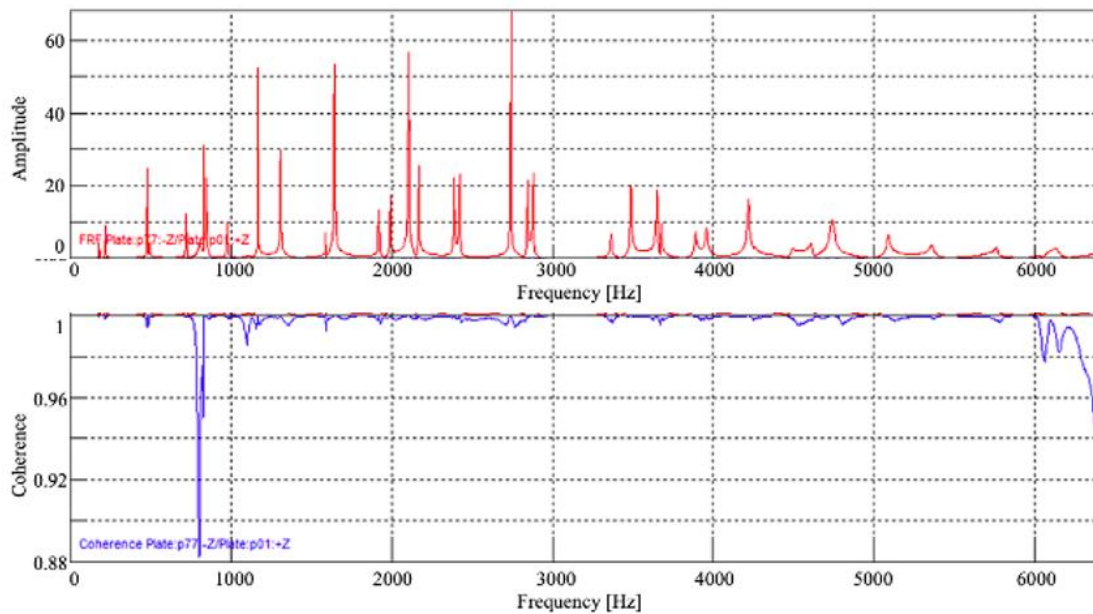
Figure 3.3 FRF Analysis and Coherence of point 1 on the plate using Acceleration/Force FRF test method
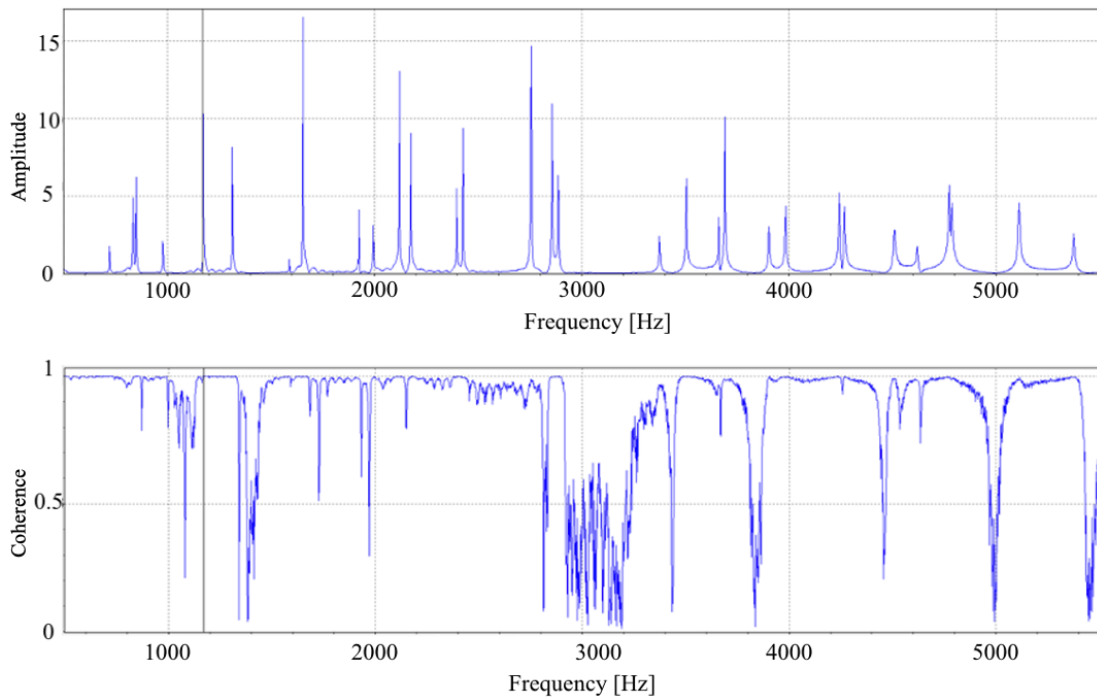
Figure 3.4 FRF Analysis and Coherence of point 1 on the plate using Velocity/Force FRF test method

The plate is in free-free condition, so it may swing as well as vibrate when a hammer hits it. The Velocity/Force FRF test uses a laser vibrometer as the output transducer, and it is a non-contact device; the laser's measured point could vary when the plate swing and twists, and the laser could measure the swing as part of the output response. These reasons could give additional noises to the output signal and lead to larger coherence. In comparison, the Acceleration/Force FRF test uses an accelerometer as the output transducer, glued to the plate surface. This could reduce the effect caused by the swinging and make sure the measuring output location remains the same throughout the experiment.

The Velocity/Force FRF test using the laser vibrometer is more suitable for modal tests using a shaker because the input force is continuous, and the noise caused by the plate's swinging effect would reduce.

3.3 Modal Testing Procedure and Results of Brake Pad

3.3.1 Experiment Setup

The Acceleration/Force FRF testing method is used to test the selected brake pad model FER7217, as shown in Figure 3.5. The pad is placed onto a foam plate to provide an almost free-free testing condition. This is because the brake pad is very small and difficult to hang. A 1D accelerometer is placed onto the pad's backplate located as shown, and the pad is excited using a robotic hammer. The size of the pad shown in Figure 3.5 is approximately 152mm*70mm*17mm(7mm backplate and 10mm friction material).
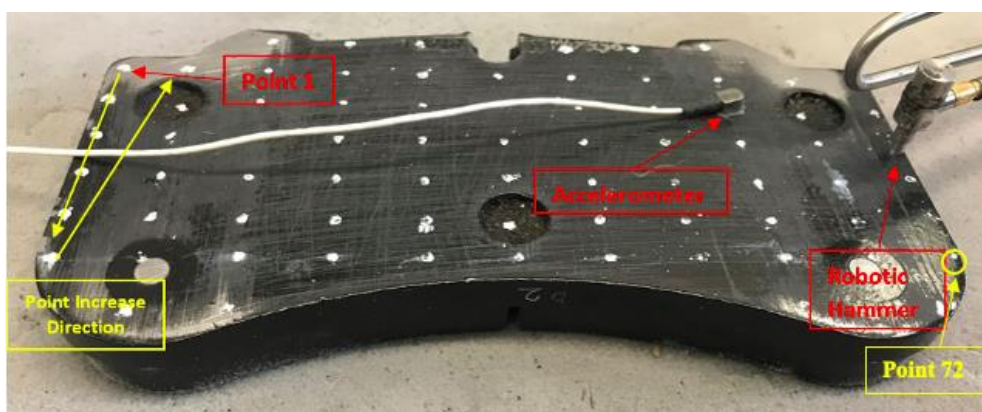
Figure 3.5 Modal test set up for the pad model FER7217 using an accelerometer

This test is a MISO test where the accelerometer's position remains unchanged during the test, and the robotic hammer's position changes to test each marked point on the pad. Each measuring point is repeated three times to average the output response measurement and reduce the input noise. The robotic hammer's location remains the same when repeating the test for one point, and the force applied to the points is controllable and the same throughout the test. This use of the robotic hammer effectively reduces the possible noise from the input force and minimizes the noise for each measurement.

The measuring frequency range of the pad is from 0 Hz to 20000Hz. Such a large range is chosen because the pad friction material is non-isotropic. There can be up to 9 updating parameters for characterizing its material properties in the identification process, i.e. if the pad is considered as an orthotropic material. The number of reliable test frequencies must be greater or equal to 9 for orthotopic material identification, and a small testing range may not cover enough reliable

modal data. The pad friction material can be considered transversely isotropic if the measured modal data is less than 9, then the minimum reliable testing frequencies and mode shapes required are 6.

Figure 3.6 gives an example of the FRF diagram and coherence of a point (point 72 indicated in Figure 3.5). The noises from both input and output signals are minimized, so the coherence is close to 1 in most frequency ranges.
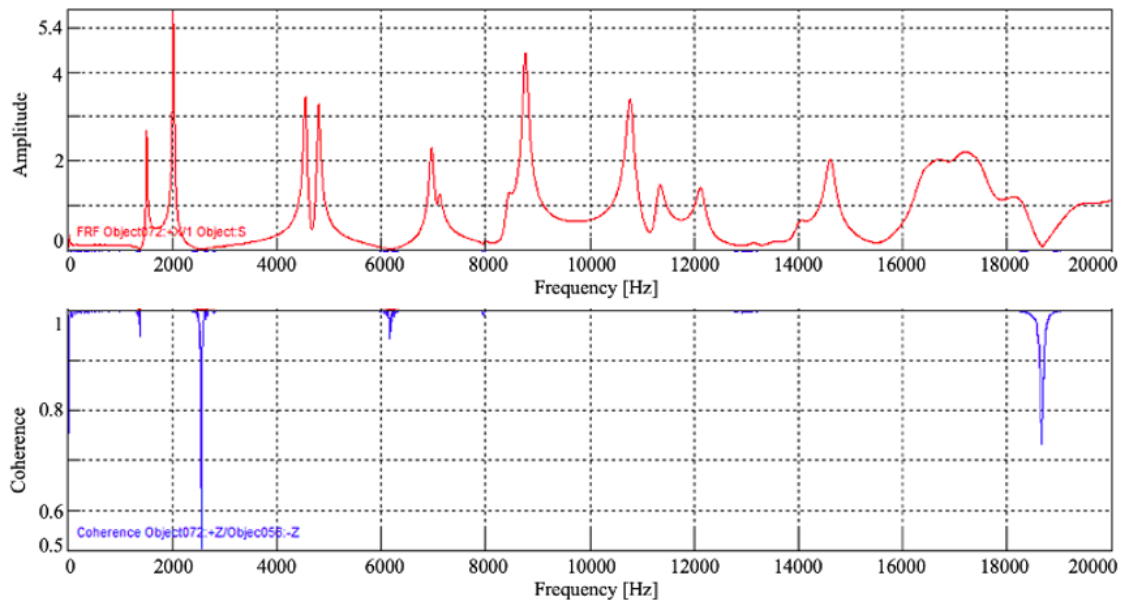
Figure 3.6 FRF Analysis and Coherence of point 72 on the pad using Velocity/Force FRF test method

3.3.2 Experiment Procedures and Data Extraction Technique using Developed Matlab Programs

Flowchart 1 shows the experimental procedures to collect the dynamic data such as the frequencies, mode shapes and damping ratios of the pad. The steps in the flowchart standardise the dynamic test of the pad and allow the developed MATLAB code to extract the experimental frequencies and mode shapes from the experimental data file.

A few steps are highlighted as they are important when trying to use the developed MATLAB code; these steps are explained below:
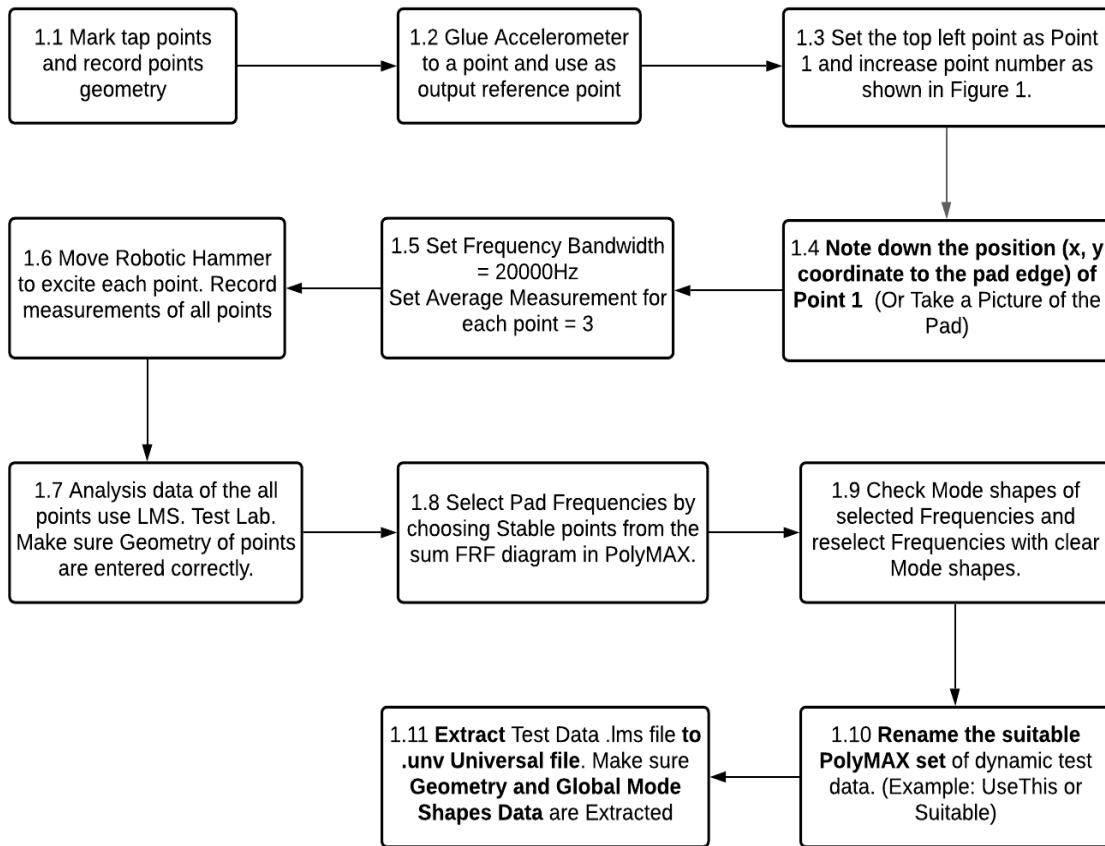
Figure 3.7 Flowchart of Acceleration/Force FRF testing process for the brake pad

Step 1.4: The position of the first testing point must be recorded because the geometry of the other test points is in the relative position of Point 1 in the experimental data file. Hence the location of all test points can be determined in the FE model if the location of Point 1 is given.

For example, in Figure 3.5, the location of test point 1 is on the top left corner of the pad. When running the MATLAB code, if the node ID of a point close to testing point 1 is entered (Figure 3.8), then the geometry of all test points can be determined and grouped as a nodal set (Figure 3.9). The analytical mode shape of the pad is extracted from this node set and can be compared with the experimental mode shape using MAC.
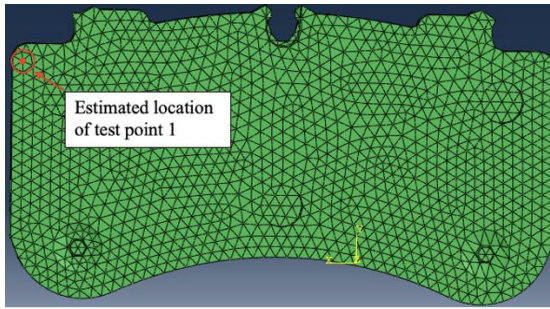
Figure 3.8 Brake pad FER 7217 FE model with selected estimated location of test point 1
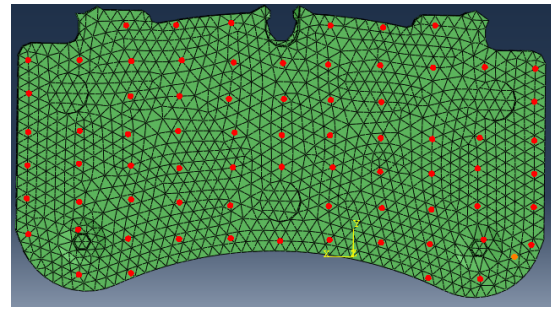
Figure 3.9 Brake pad FER 7217 FE model with selected estimated location of all test points

The global coordinate systems of the FE and test models are determined and matched depending on the maximum length and width of the model from point 1. For example, if the length of the pad is considered as the x-axis in the test and y in the FE model, they will be matched by changing the orientation of the pad in the FE input file. The x and y distance between each point in the FE model is calculated after considering the ratio between the maximum x and y distance in the test data and FE model.

Step 1.7 – 1.9: The raw data of the pad from the dynamic test is analysed using the software LMS. Test Lab. This will be further explained in section 3.3.3.

Step 1.10: This is not a necessary step, but it would be easier to rename the PolyMAX set containing the experimental data used in the material property updating procedure (as shown below).
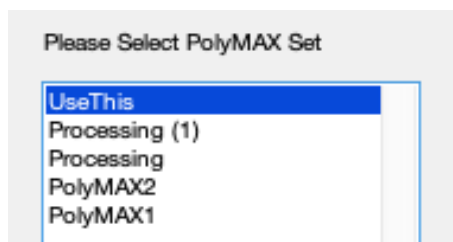
Step 1.11: The developed MATLAB code that reads the experimental file can only determine the data from the universal file. Hence a .unv type of file must be extracted after selecting the suitable test frequencies and mode shapes.

3.3.3 Data Analysis

The LMS Test Lab is used to simulate the raw data of the dynamic test and extract the frequencies and mode shapes of the pad. LMS uses a well-known algorithm, PolyMAX, for the post-processing of the test data. The sum FRF of the pad measured by the robotic hammer and the accelerometer is analyzed using the build-in mathematical function PolyMAX in the LMS test lab, and its stable poles are shown in Figures 3.9 and 3.10 with the frequency range between 0 Hz and 10000 Hz; and between 10000 Hz and 20000 Hz, respectively. It is worth mentioning that this test has been done several times, and the best result is shown here.
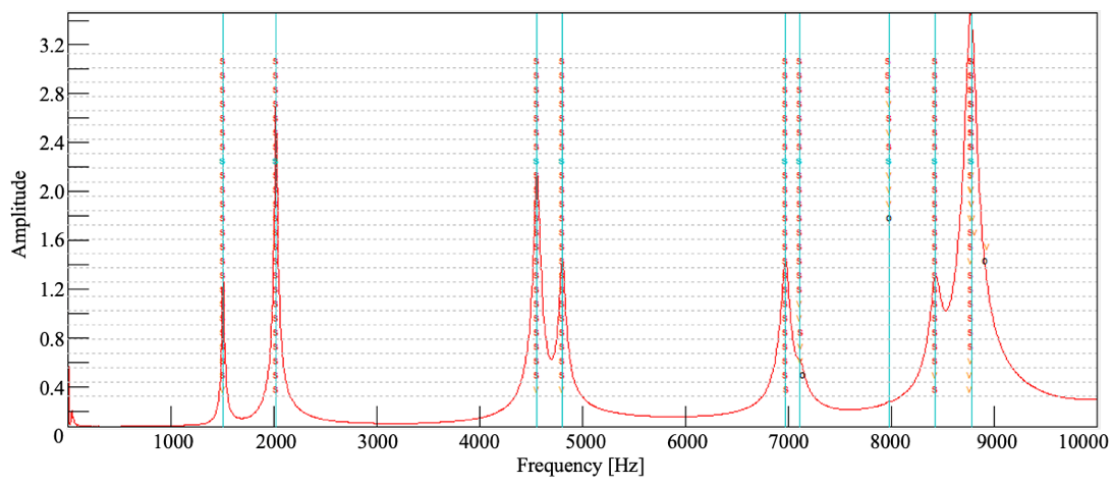
Figure 3.10 The sum FRF of the pad from 0 Hz to 10000 Hz using LMS
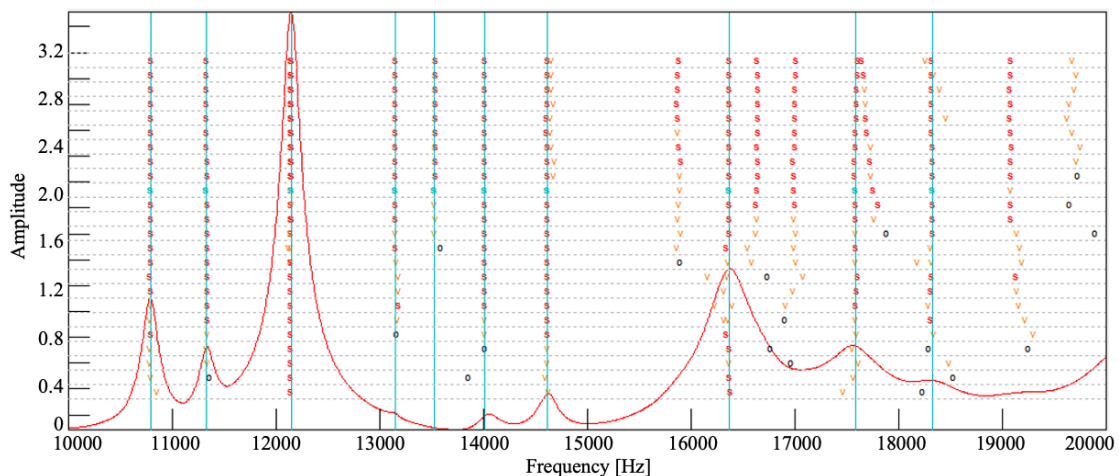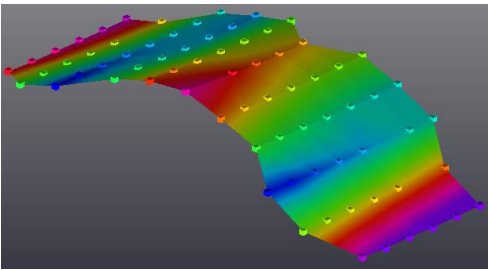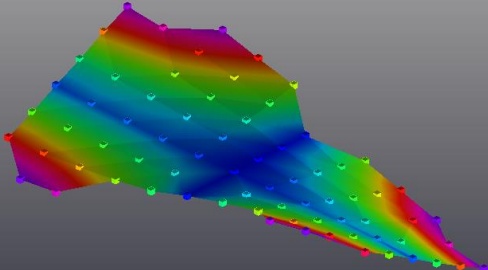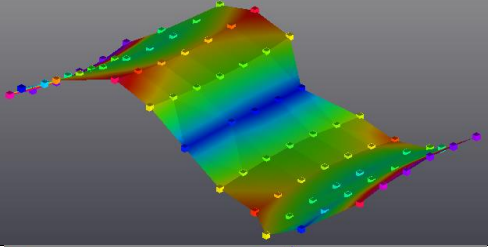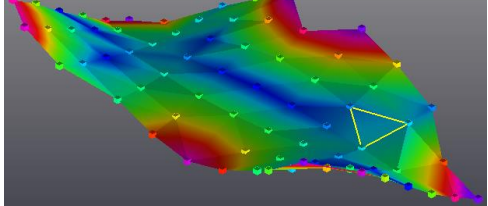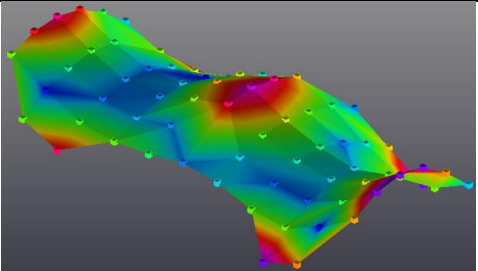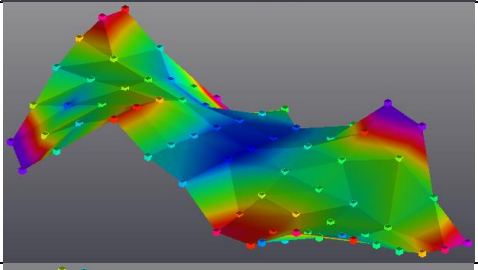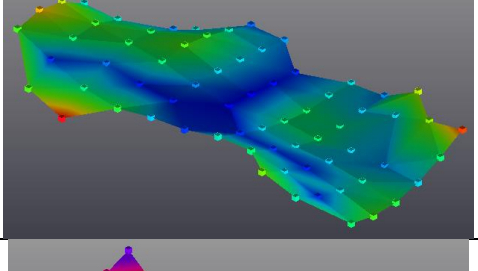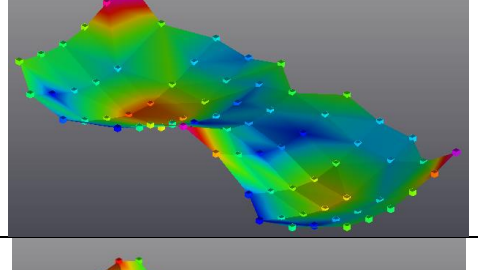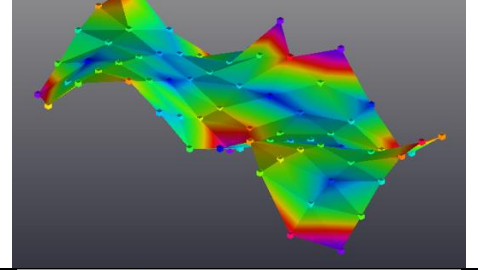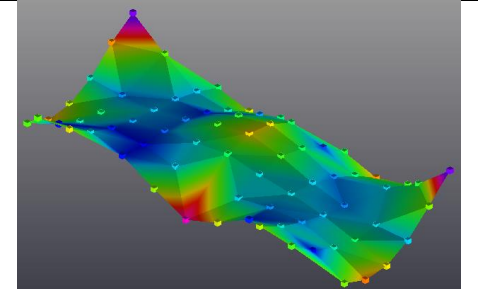
Figure 3.11 The sum FRF of the pad from 10000 Hz to 20000 Hz using LMS
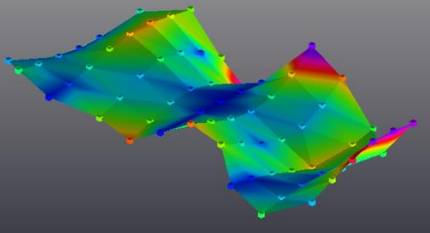
The reliably measured frequencies, damping and mode shapes of pad model FER7217 are listed in Table 3.2. These data are simulated from LMS PolyMAX and will be extracted to the universal file to use in the material identification procedure in Chapter 5.

Table 3.2 Measured frequencies, damping and mode shapes of the pad using LMS software

Mode Number	Measured Undamped Frequency (Hz)	Damping Coefficient (%)	Mode Shape
1	1507	0.66	
2	2020	0.71	
3	4556	0.72	
4	4803	0.69	

5	6970	0.69	
6	7113	0.71	
8	8429	0.72	
9	8775	0.62	
10	10788	0.74	
11	11332	0.70	

| 12 | 12140 | 0.62 | |

3.4 Summary

The fundamental theories of the dynamic experimental modal analysis are presented in this chapter. A suitable experimental testing procedure is found by comparing the test results of a plate from the Acceleration/Force FRF testing method and Velocity/Force FRF testing method. The Acceleration/Force FRF testing method is found to be more reliable and therefore is used to test the brake pad model FEF7217. The standard testing procedure for the brake pad is presented in section 3.3.2, and the collected dynamic experimental data is shown in section 3.3.3.

Chapter 4 Static Experimental Procedures and Data Analysis

The properties of brake pad friction materials can be determined from either the static experimental data or the dynamic experimental data. This chapter introduces the fundamental theories of the stress-strain relationship of non-isotropic materials, the strain gauge and Digital Imaging Correlation (DIC). In Section 4.2, the compression test procedure and results of the brake pad using the glued strain gauge to measure the longitudinal change in strain. Section 4.3 shows the compression test procedure and results of the brake pad using the DIC to measure the longitudinal change in strain. The reliable compression test results are used to estimate the Young's Modulus and Poisson's Ratio of the brake pad FER7217.

4.1 Introduction

In this chapter, compression tests were done to measure the material properties of pad materials at different pressures. The mechanical properties of the brake pad material can be calculated from the stress-strain relationship of the compression test. The calculated mechanical properties, including the Young's Modulus and Poisson Ratio of the brake pad, can be used as the initial updating parameters in the material properties identification method in chapter 5. the stress-strain relationship of the pad friction material is also useful in the simulation of the friction material as Hyperelastic material.

4.1.1 Stress-Strain Relationship for Non-isotropic Materials

The generalised Hooke's Law can be written as:

$$\boldsymbol{\sigma} = \mathbb{C}\boldsymbol{\varepsilon} \tag{4.1}$$

where $\boldsymbol{\sigma}$ is the change in stress, $\mathbb{C}$ is the stiffness tensor matrix that provides the relationship between the stress and the strain of the structure, and $\boldsymbol{\varepsilon}$ is the change in strain of a system. For an anisotropic linear elastic material, the stiffness tensor matrix can be written as:

$$\mathbb{C} = \begin{bmatrix} C_{11} & C_{12} & C_{13} & C_{14} & C_{15} & C_{16} \\ C_{12} & C_{22} & C_{23} & C_{24} & C_{25} & C_{26} \\ C_{13} & C_{23} & C_{33} & C_{34} & C_{35} & C_{36} \\ C_{14} & C_{24} & C_{34} & C_{44} & C_{45} & C_{46} \\ C_{15} & C_{25} & C_{35} & C_{45} & C_{55} & C_{56} \\ C_{16} & C_{26} & C_{36} & C_{46} & C_{56} & C_{66} \end{bmatrix} \tag{4.2}$$

where C_{ij} is the elastic constant of a system and can be converted to the engineering constants such as Young's Modulus, Poisson's Ratio and Shear Modulus. In this general stiffness tensor matrix, there are 21 independent elastic constants due to matrix symmetry. A sufficient number of test data (more than 21) must be obtained to determine the material properties, which is too many. Hence, most of the time, the material is considered as orthotropic instead:

$$\begin{bmatrix} \sigma_{11} \\ \sigma_{22} \\ \sigma_{33} \\ \sigma_{12} \\ \sigma_{13} \\ \sigma_{23} \end{bmatrix} = \begin{bmatrix} C_{11} & C_{12} & C_{13} & 0 & 0 & 0 \\ C_{12} & C_{22} & C_{23} & 0 & 0 & 0 \\ C_{13} & C_{23} & C_{33} & 0 & 0 & 0 \\ 0 & 0 & 0 & C_{44} & 0 & 0 \\ 0 & 0 & 0 & 0 & C_{55} & 0 \\ 0 & 0 & 0 & 0 & 0 & C_{66} \end{bmatrix} \begin{bmatrix} \varepsilon_{11} \\ \varepsilon_{22} \\ \varepsilon_{33} \\ 2\varepsilon_{12} \\ 2\varepsilon_{13} \\ 2\varepsilon_{23} \end{bmatrix} \qquad (4.3)$$

This stiffness tensor matrix in equation 4.3 consists only of 9 independent elastic constants, which would be much easier to determine than general anisotropic materials; hence this is the first option for modelling the brake pad material.

The elastic constants C_{ij} of the orthotropic object defined in equation 4.3 can be calculated from the E_i, ν_{ij} and G_{ij} using the equations below:

$$C_{11} = \frac{1 - \nu_{yz} * \nu_{zy}}{E_y * E_z * \Delta} \qquad (4.4)$$

$$C_{12} = \frac{\nu_{yx} + \nu_{yz} * \nu_{zx}}{E_y * E_z * \Delta} \qquad (4.5)$$

$$C_{13} = \frac{\nu_{zx} + \nu_{yx} * \nu_{zy}}{E_y * E_z * \Delta} \qquad (4.6)$$

$$C_{22} = \frac{1 - \nu_{xz} * \nu_{zx}}{E_x * E_z * \Delta} \qquad (4.7)$$

$$C_{23} = \frac{\nu_{zy} + \nu_{yz} * \nu_{zx}}{E_x * E_z * \Delta} \qquad (4.8)$$

$$C_{33} = \frac{1 - \nu_{xy} * \nu_{yx}}{E_x * E_y * \Delta} \qquad (4.9)$$

$$C_{44} = G_{xy} \qquad (4.10)$$

$$C_{55} = G_{xz} \qquad (4.11)$$

$$C_{66} = G_{yz} \qquad (4.12)$$

$$\Delta = \frac{1 - \nu_{xy} * \nu_{yx} - \nu_{yz} * \nu_{zy} - \nu_{xz} * \nu_{zx} - 2 * \nu_{yx} * \nu_{zx} * \nu_{xy}}{E_x * E_y * E_z} \qquad (4.13)$$

The pad friction material can be further simplified to transversely isotropic materials, which reduces the number of independent unknowns in the stress-

strain law from 9 to 6. As transversely isotropic materials (or layerwise isotropic material), it is assumed that the pad is a composite material-built layer by layer, and within each layer, the material is isotropic. The benefit of this assumption is that the mechanical properties can be assumed as isotropic within the layer of isotropic material.

For example, if the materials alone the x-y plane is said to be isotropic, then the Young's Modulus in the x-direction would equal to Young's Modulus in the y-direction, $E_x = E_y$; the Poisson ratio of the x-direction to z-direction would be the same as the Poisson ratio of the y-direction to the z-direction, $\nu_{xz} = \nu_{yz}$; and the Shear Modulus in the x-z plane is the same as the Shear Modulus in the y-z plane, $G_{xz} = G_{yz}$。

After the above assumption, the reduced stress-strain relationship of the pad is:

$$
\begin{bmatrix} \sigma_{11} \\ \sigma_{22} \\ \sigma_{33} \\ \sigma_{12} \\ \sigma_{13} \\ \sigma_{23} \end{bmatrix} = \begin{bmatrix} C_{11} & C_{12} & C_{13} & 0 & 0 & 0 \\ C_{12} & C_{11} & C_{13} & 0 & 0 & 0 \\ C_{13} & C_{13} & C_{33} & 0 & 0 & 0 \\ 0 & 0 & 0 & C_{44} & 0 & 0 \\ 0 & 0 & 0 & 0 & C_{55} & 0 \\ 0 & 0 & 0 & 0 & 0 & C_{55} \end{bmatrix} \begin{bmatrix} \varepsilon_{11} \\ \varepsilon_{22} \\ \varepsilon_{33} \\ 2\varepsilon_{12} \\ 2\varepsilon_{13} \\ 2\varepsilon_{23} \end{bmatrix}
\tag{4.14}
$$

The six unknown mechanical properties would be the Young's Modulus in the x and y directions, E_x, Young's Modulus in the z-direction, E_z, the Poisson Ratio in the x-y direction, ν_{xy}, the Poisson Ratio in the x-z and y-z direction, ν_{xz}, and the Shear Modulus in the x-z and y-z direction, G_{xz}.

4.2 Compression Test With Attached Strain Gauge

The stress and strain relationship of the pad friction material is useful in terms of understanding the mechanical properties of the pad. Compression tests were done to measure the change in strain of the test sample of the pad in different directions under different loading pressure. In this section, the compression tests were done using rectangular specimens from the pad model. The specimens have a backplate on, and the change in strain of the pad in the lateral direction is measured using strain gauges.

4.2.1 Experiment Setup

An Instron machine was used to apply a compressive force to a cuboid specimen, and the specimen was cut from a brake pad. Figure 4.1 shows the overview of the Instron Machine. During the compression rate test, the top block of the Instron machine was pressed down to apply a compressive force onto the specimen. The direction of the compression force was set to be the z-direction of the system.

The change in strain in z-direction could be measured from the Instron machine. The Strain Indicator and Recorder (Figure 4.2) was used to measure the change in strain determined from the strain gauges glued onto the specimen. Figure 4.3 shows the pad specimen, and a few strain gauges were attached to the specimen to measure the change in strain of the specimen in x and y-direction. This machine included four channels and could automatically read the change in strain from four strain gauges.

The compressive force was added at a rate and set up before the test. The results were collected at a standard time rate which would also be set up. The maximum force applied onto the specimen was set up to be the stopping condition of the test. After setup the machine, the Instron machine would apply compressive force at a constant compression rate; the results collected from the Instron machine were the time, force applied, and the change in length of the specimen.
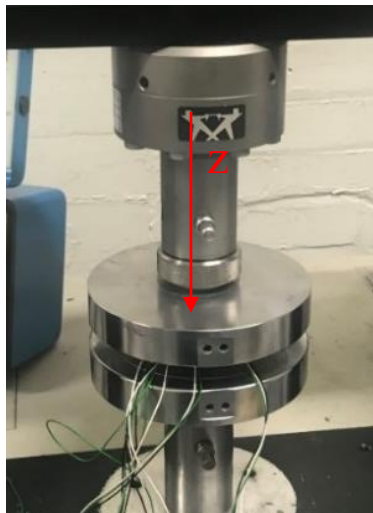
Figure 4.1 Instron Machine

Figure 4.2 Strain Indicator and Recorder

Figure 4.3 Specimen in the Instron Machine
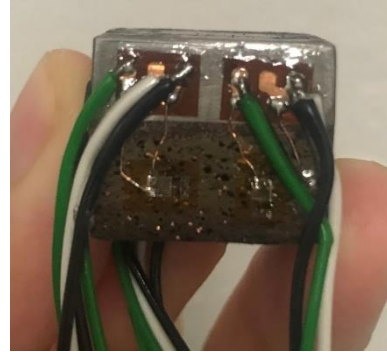
Figure 4.4 Specimen surface with two strain gauges

Figure 4.5 Specimen surface with one strain gauges
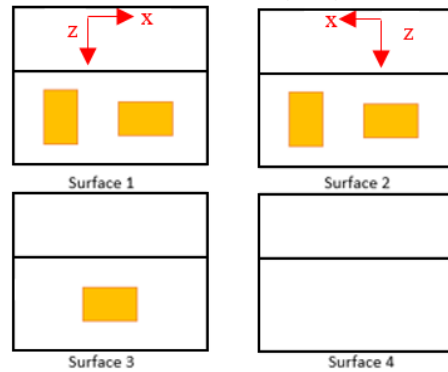
Figure 4.6 Simple Diagram of Specimen Surfaces with Strain Gauges

	Length [mm]	Width [mm]	Thickness [mm]
Specimen Size	20	20	7 (Backplate) 10 (Friction Material)
Strain Gauge Model Number	Micro Measurements EA-06-031CE-350		

The details of the test specimen are shown in Figures 4.4, 4.5, and 4.6. Two strain gauges were applied on surfaces 1 and 2, and surface 1 is parallel to surface 2. For example, in surface 1, a strain gauge was applied to measure the change in strain in the x-direction, and the other was used to measure the strain in the vertical (z) direction. A single strain gauge was applied on the surface 3 in the y-direction. The vertically applied strain gauges were to validate the test results

75

of the vertical strain collected from the Instron machine and the attached strain gauges.

Note that the steel backplate of the pad was kept on the measuring specimen. This is because the friction material itself is too thin, and it would be very difficult to glue the strain gauges and the terminals onto the friction material without the backplate. A comparison between the vertical change in strain with and without the backplate was made using the data collected from the Instron machine and the vertical strain gauges.

By measuring the change in strain in the x, y and z-direction under stress in the z-direction, an estimation of the pad material's Poisson's Ratio and Young's Modulus in x, y and z-direction could be determined. Assuming the direction of the compressive force is the z-direction (shown in Figure 4.1), the material's Young's Modulus E_x, E_y (using strain gauges) and E_z (from Instron machine) could be calculated as well as its Poisson's Ratio ν_{xz} and ν_{yz}.

4.2.2 Test Results – Instron Machine

The compression rate was set to 1.5mm/s for this specimen; this value was referred to as the ISO Standard Compression Rate (ISO 6310:2009 standard for brake lining compression test). The time to collect each measurement is 0.1s, and the maximum force applied to the specimen is 3000N.

The results of the extension of the specimen could be converted to the change in strain in the z-direction (Figure 4.3) from the equation $\varepsilon = \frac{\Delta L}{L}$, where L is the thickness of the specimen. The loading force results can be converted to the stress applied in the z-direction of the specimen from the equation $\sigma = \frac{F}{A}$ where F is the force applied onto the test specimen, and A is the cross-section area of the specimen. Hence, a stress-strain curve could be drawn from the Instron machine data, as shown in Figures 4.7 and 4.8.
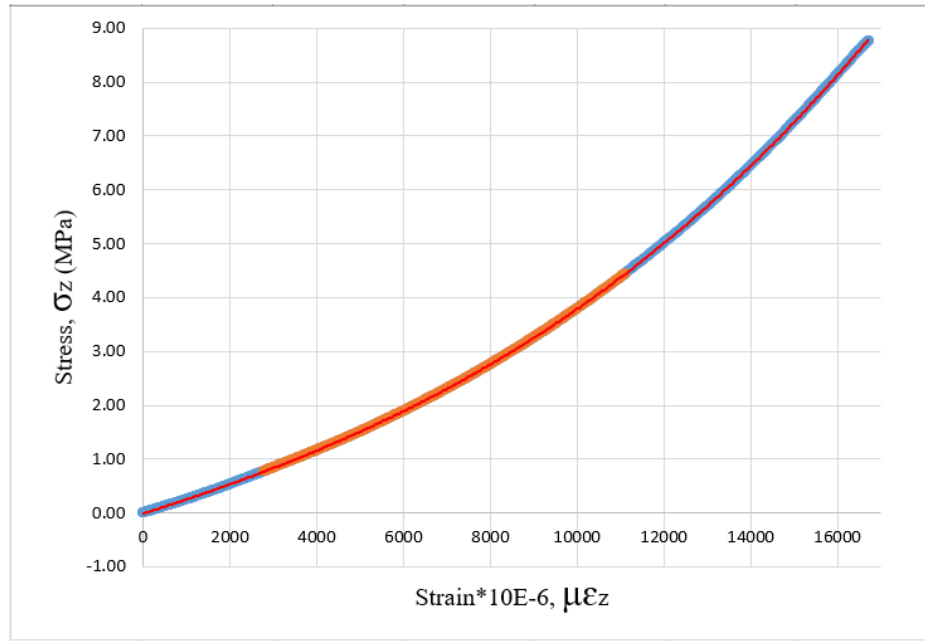
Figure 4.7 Stress vs Strain curve in the z-direction of test 1 of the specimen
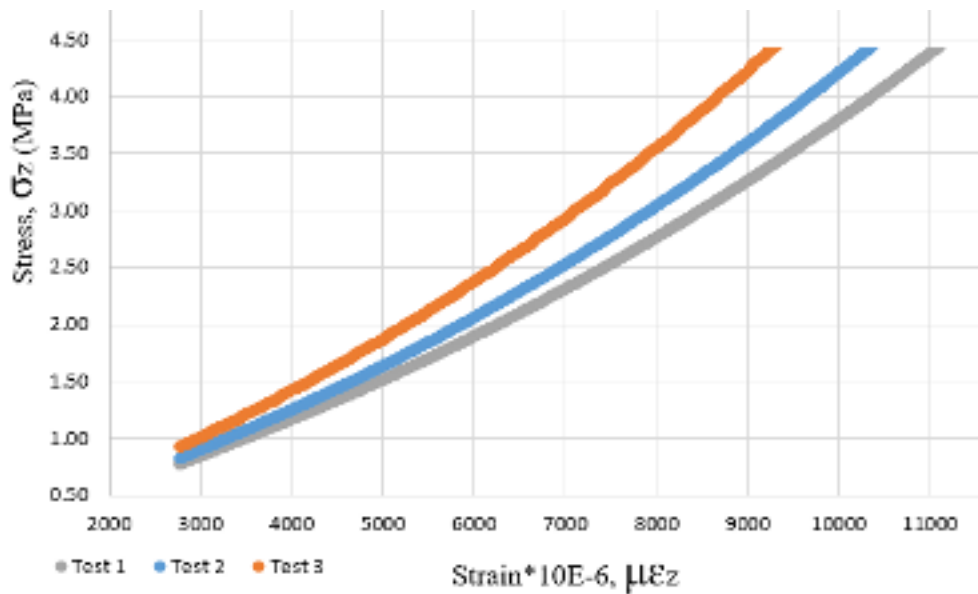
Figure 4.8 Stress vs Strain curve comparison of three tests of the specimen

Figure 4.7 shows the stress-strain relationship of the pad specimen in compression test 1. This is a stress-strain curve for a typical elastic material displaying nonlinear behaviour. The data in blue shows the stress-strain curve of the full test range, and the data in orange is the stress-strain relationship of the specimen between the testing time of 20 seconds and 80 seconds. This test data

77

range was chosen to eliminate the inaccurate results at the beginning of the test (where the change in strain is 0), and at the end of the test, there could be a possibility that the stress applied to the material has passed yield point. Now use the selected time range above to compare the stress-strain curves from different compression tests, as shown in Figure 4.8.

The three curves in Figure 4.8 shows the stress-strain behaviour of the same specimen from Test 1 (grey), Test 2 (blue), and Test 3 (orange). Note that the change in strain of the specimen in each test is the same; in other words, the time range of the data is the same. However, as more tests were done, the change in strain reduced with the same stress applied to the specimen.

There could be two possibilities for this behaviour. Firstly, the specimen would recover to its original thickness in time. However, the recovery time between each test could be too short, and the specimen did not recover to its original shape before the next test. Therefore extra force was needed for the specimen to have the same change in strain. If this case is considered as the true behaviour of the pad material, then the pad could be assumed as hyperelastic material where the response is fully path independent and reversible, and the stress is derived from a strain (or stored) energy potential.

Secondly, the specimen would not recover to its original shape in time and energy dissipated during the test process. Due to this energy dissipation, loading and unloading behaviours are not identical, and loading moduli could be determined separately from unloading moduli.

4.2.3 Test Results – Strain Gauge

A Strain Indicator and Recorder was used to measure the change in strain determined from the strain gauges (Figure 4.2). This machine included four channels and could automatically read the change in strain from four strain gauges.

In the beginning, the four strain gauges from Surface 1 and 2 (from Figure 4.6) were used. However, the measured test data were not very reliable. For example, in most cases, if the vertical strain gauges determined a negative change in strain, then the horizontal strain gauges should determine the positive change in strain so that the Poisson's ratio is positive. However, the determined vertical and

horizontal changes in strain were both negative. Negative Poisson's ratio is possible in other cases, but the pad friction material was expected to have a positive Poisson's ratio.

Another compression test was done after the horizontal strain gauge in Surface 3 replaced the horizontal strain in surface 1. This test measured the change in strain measured from both the horizontal (from surfaces 3) and vertical strain gauges. Hence this data was used to analyse the test data.

The vertical change in strain of the whole specimen and the friction material is shown in Figure 4.9 below. This Figure shows that the overall strain rate increases more than the strain rate in the friction material under the same pressure. Hence, the backplate impacts the overall change in strain, and the change in strain measured from the strain gauges should be used when calculating the material properties of the friction material.
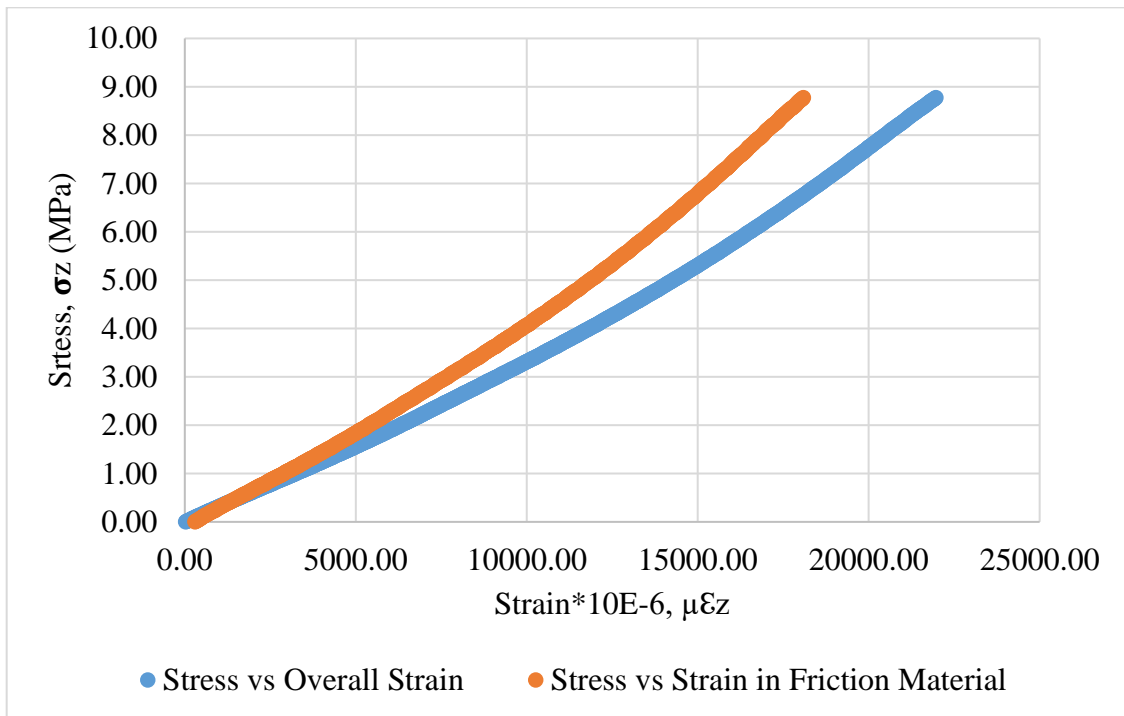
Figure 4.9 Stress vs Strain curve comparison of three tests of the specimen

The Young's modulus of the friction material in different directions could be determined from $E_i = \dfrac{\sigma_i}{\varepsilon_i}$ where i is the selected direction, and the stress-strain

79

relationships in different directions were measured from the compression test by turning the sample 90 degrees.

However, because this particular test sample has more than one material (the backplate and the pad), only Young's modulus of the friction material in z-direction could be determined as the compression test results of the friction material in the x and y-direction could be affected by the backplate. Figure 4.10 shows Young's modulus of the friction material with respect to time. Note this Young's modulus was calculated from the strain data collected by the strain gauge.
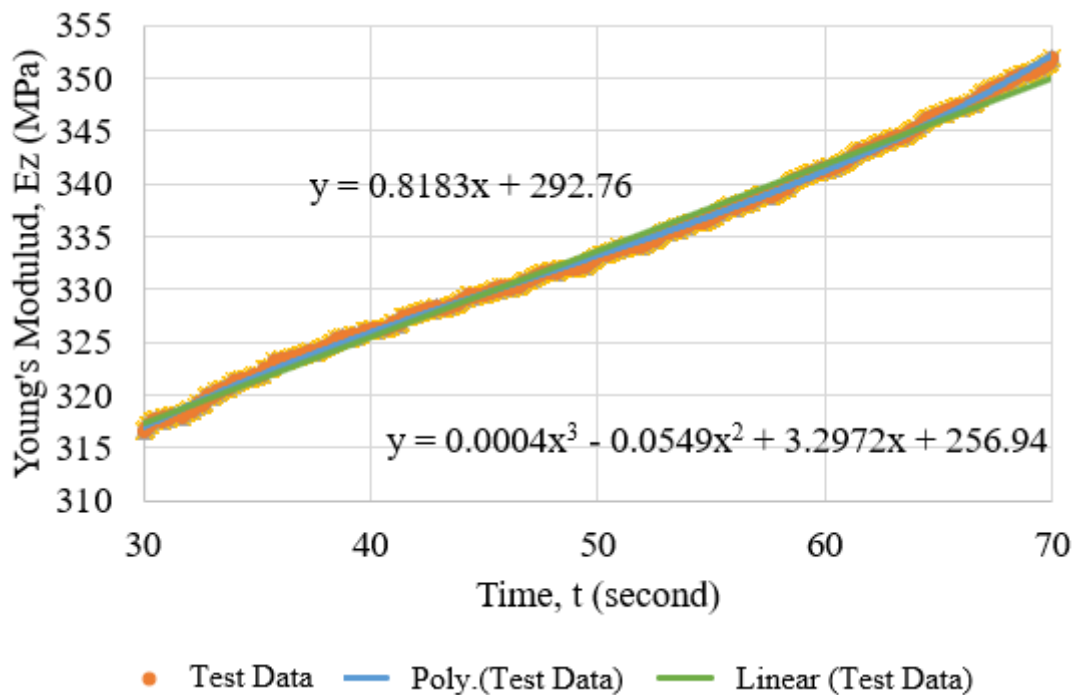
Figure 4.10 Young's Modulus Ez vs Time t

Two trendlines were applied to the test data: a linearly fitted trendline and a polynomial trendline. The equations of both trendlines are shown in Figure 4.10, and the Least square error between the actual data and the data using different trendlines are shown in table 4.2 below (Definition of Least square error could be found in section 5.3.2.1).

Table 4.1 Least squares error between the estimated Young's modulus and measured Young's modulus.

	Linear Trendline	Polynomial Trendline
Least Squares Error	1.63E-03	1.21E-02

Young's modulus in the z-direction varies with time, and table 4.2 shows that the linear prediction of Young's modulus in the z-direction is better than the nonlinear prediction of the friction material.

The Poisson's ratio in different directions could be calculated from $v_{ij} = \dfrac{\partial \varepsilon_j}{\partial \varepsilon_i}$ where ε_j is the lateral strain and ε_i is the axial strain. The lateral strain data was measured from the strain gauge in surface 3, and the axial strain was measured from the average vertical strain from surfaces 1 and 2. Figure 4.11 shows the variation of the Poisson's ratio v_{yz} with respect to time t.
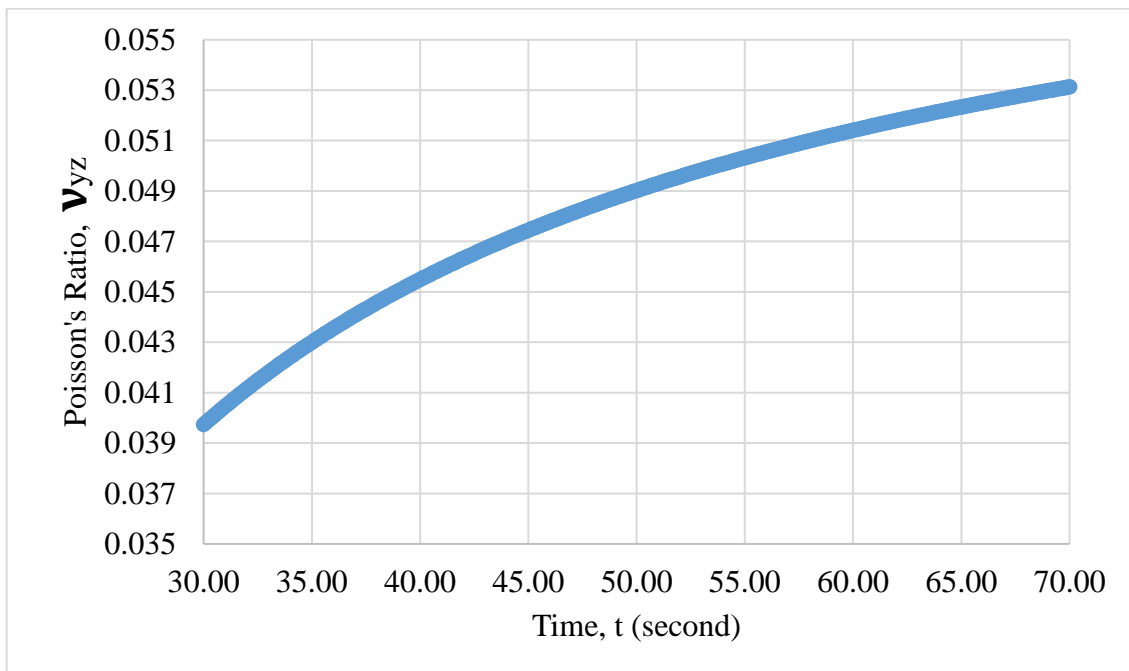
Figure 4.11 Poisson's Ratio v_{yz} vs Time t

Figure 4.11 shows that the Poisson's ratio determined from this compression test was very small, and the results needed further validation with other compression test results.

81

There are many disadvantages to using strain gauges to measure the compression test data of the friction material: the extra boundary conditions created by glueing the strain gauge on the friction material surface and the size of the strain gauges are too large considering the small sample thickness of the pad. Also, although some oil was put as a lubricant between the contact surface of the pad and the Instron machine, the friction between the pad surface and the Instron machine contact surface could still be very large because of the small specimen size. If the friction between the specimen surface and the Instron Machine contact surface is very large, then boundary conditions are applied to the edge of the specimen. Since the strain gauges were very close to the edge of the specimen, the data collected from the strain gauges could be largely affected.

Due to the above concerns that could affect the compression test data of the friction material, another method was proposed using the non-contact measuring technique Digital Image Correlation (DIC) to determine the change in strain of the friction material.

4.3 Compression Test With Digital Image Correlation

Digital Image Correlation (DIC) are now widely used to measure the change in strain of a structure, and it has many advantages compared with the strain gauges. DIC consists of finding the transformation between the reference picture and the distorted picture by analysing the pixel displacement of the applied surface speckle pattern observed by the camera during loading.

DIC is a non-contact measuring technique, so there are no additional mass or glue applied to the sample structure, and the mechanical properties of the sample would not be affected. DIC also provides an full field of the change in strain of the whole measuring surface rather than just a small part. With these advantages, compression tests of the friction material were set up, and the strain data were measured using DIC and the Instron machine.

4.3.1 Experiment Setup

The friction material of the pad model FER7217 is cut into three cuboid-shaped samples, as shown in Figure 4.12 below.
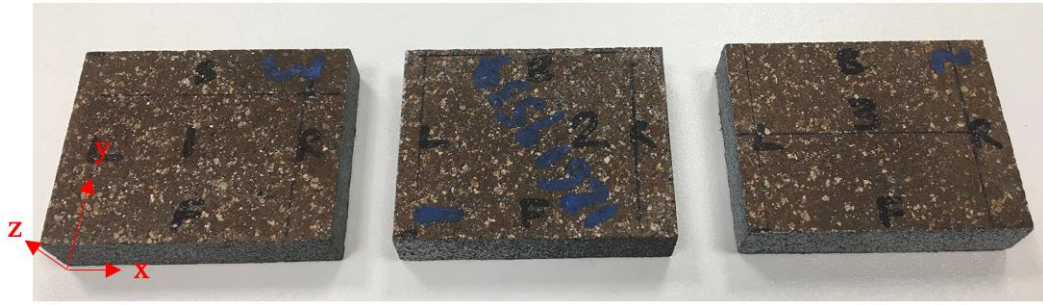
Figure 4.12 Sample 1, 2 and 3 used in the compression test

Note that the samples were blocks containing the friction material without the backplate. The coordinate system of the experiments was set up as shown in Figure 4.12 in red, and the sizes of all samples were measured and listed in table 4.3:

Table 4.2 DIC Experiment Sample Sizes

	Average Width, x [mm]	Average Depth, y [mm]	Average Thickness, z [mm]	Cross Section Area [mm^2]		
				Compress surface x	Compress surface y	Compress surface z
Sample 1	50.23	40.04	11.45	458.46	575.13	2011.21
Sample 2	50.24	40.09	11.21	449.41	563.19	2014.12
Sample 3	50.16	40.04	11.39	456.06	571.32	2008.41

The compression tests were done using the Instron machine, and because the size of each sample in the z-direction was very small, two large blocks were added above and below the sample to give a better side view and more accurate horizontal strain change measurement. Different forces were applied to each test sample in different directions.

Figure 4.13 and 4.14 shows the test setup of a sample with force applied to z and x-direction. The force applied to the sample was controlled using the Instron machine, and the change in strain of the sample was measured using the Digital Image Correlation (DIC) technique.
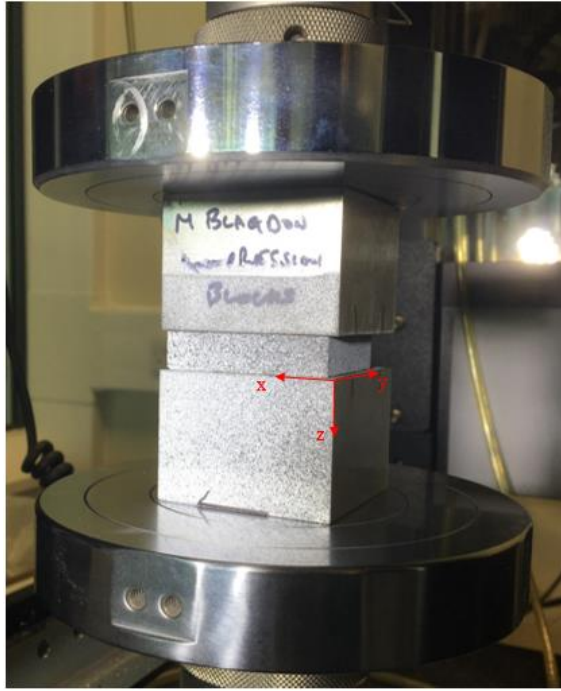
Figure 4.13 Compression test with force applied in the z-direction
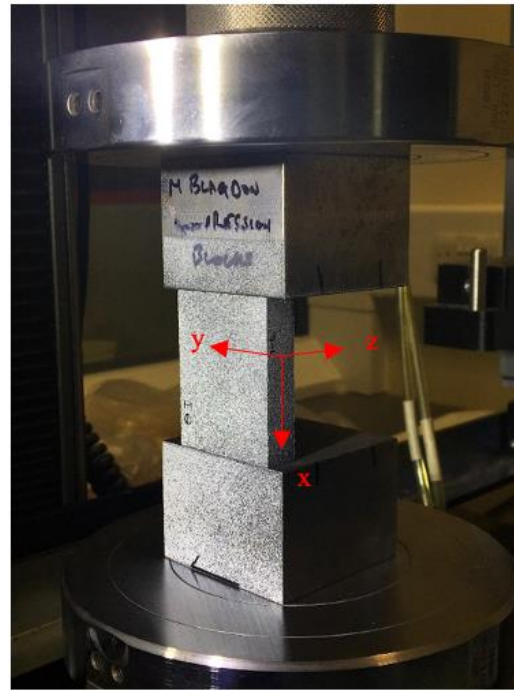
Figure 4.14 Compression test with force applied in the x-direction

The maximum forces applying to the samples were set up in the Instron machine, and different compression directions have different maximum applying loads (as shown in table 4.4). Different loading forces were set up in each direction because of the different cross-section areas in the compressing direction. The general maximum pressure applied to all directions were about 6MPa. The compression forces were set up in different levels to observe the behaviour of the friction material under different pressure.

Table 4.3 DIC Experiment Maximum Force Setup

Direction of compression force	x	y	z
Maximum force applying on the sample	2 kN	1.5 kN	3 kN
	4 kN	3 kN	6 kN
			9 kN
			12 kN

The time increment to collect the compression test data was set as 0.02 seconds for the Instron machine and 1 second for the DIC camera. The changes in vertical strain were measured using both Instron machine and DIC, and the results from

84

both measurements were compared in Figure 4.19. The changes in horizontal strain were measured using DIC and shown in section 4.3.2.

A test sample must rotate 90 degrees four times to measure the horizontal change in strain in all four surfaces. For example, if the force was applied in the z-direction, at least four tests must be done to measure the horizontal change in strain, and the sample would rotate 90 degrees in x (or y) direction after each test.

The Poisson's ratios v_{xy} and v_{xz} could be determined when the stress was applied in the x-direction and the change in strain in x, y and z-direction were measured (as shown in Figure 4.15) $v_{xy} = \frac{\varepsilon_y}{\varepsilon_x}$, $v_{xz} = \frac{\varepsilon_z}{\varepsilon_x}$. The Poisson's ratio v_{yz} is calculated by applying the stress in the z-direction and measuring the strain in the y-direction (Figure 16), $v_{yz} = \frac{\varepsilon_z}{\varepsilon_y}$.
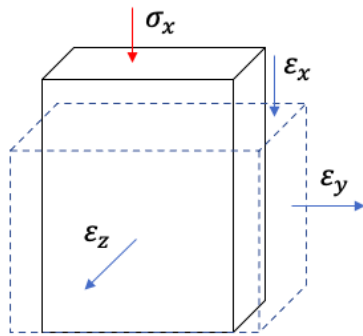
Figure 4.15 Applying stress in the x-directions
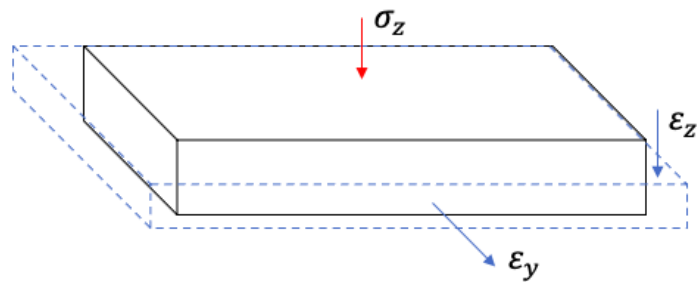
Figure 4.16 Applying stress in the z-directions

4.3.2 Test Results

Measured compression test data from the DIC camera were analysed using the software GOM Correlation and Figure 4.17 shows an example of the data collected from the DIC camera. A few points were selected on the friction material surfaces to observe the changes in the strain of the sample in the axial and lateral directions at different points. Points on the upper and lower metal blocks were selected to observe whether the overall changes in vertical strain contains the changes in the vertical strain of the blocks.
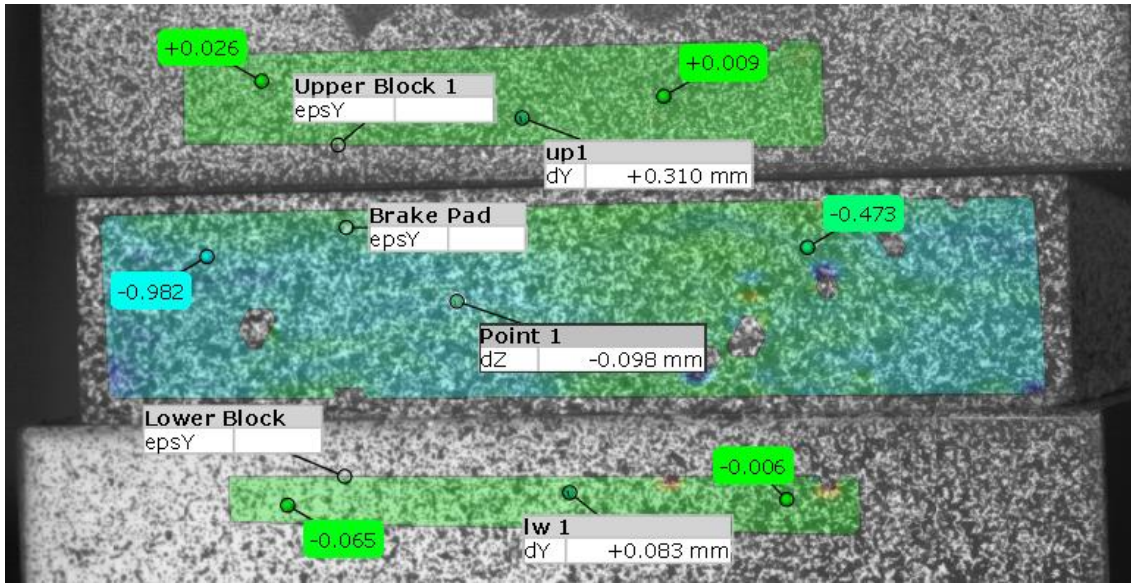
Figure 4.17 GOM correlate of sample 1 from DIC measurement

The test results shown in this section were the lateral change in strain measurements from sample 1. There were 12 tests done with this sample, and the force vs displacement diagrams for each testing direction are shown in Figures 4.18 to 4.20 below.

Figure 4.18 presents the strain changes in x and y-directions while applying forces in the z-direction. Note that the strain changes in x and y-directions were similar under the same loading force. Hence, it could be assumed that the changes in strain in the x-direction are equal to the change in strain in the y-direction, and the Poisson's ratio v_{xz} could equal the Poisson's ratio v_{yz}. The pad friction material could be assumed as transversely isotropic material, with the isotopic plane being the xy-plane. Figure 4.19 shows the strain changes in x and z-directions while applying forces in the y-direction. The diagram shows that the average strain changes in the x-direction and z-direction were very different. The results from Figure 4.19 concluded that the Poisson's ratio v_{xy} and v_{zy} of the friction material would be different. Figure 4.20 shows the strain changes in y and z-directions while applying forces in the x-direction. The conclusion drawn from Figure 4.10 was similar to Figure 4.19, with the Poisson's ratio v_{xz} different from v_{xy} of the friction material.
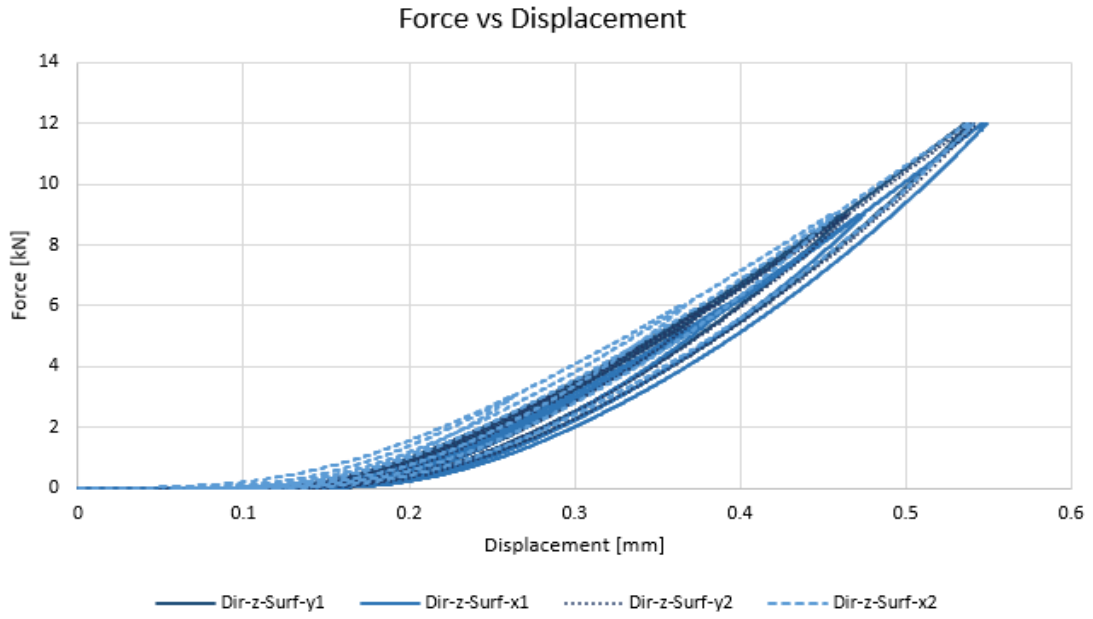
Figure 4.18 Force vs Displacement diagrams when applying force in the z-direction
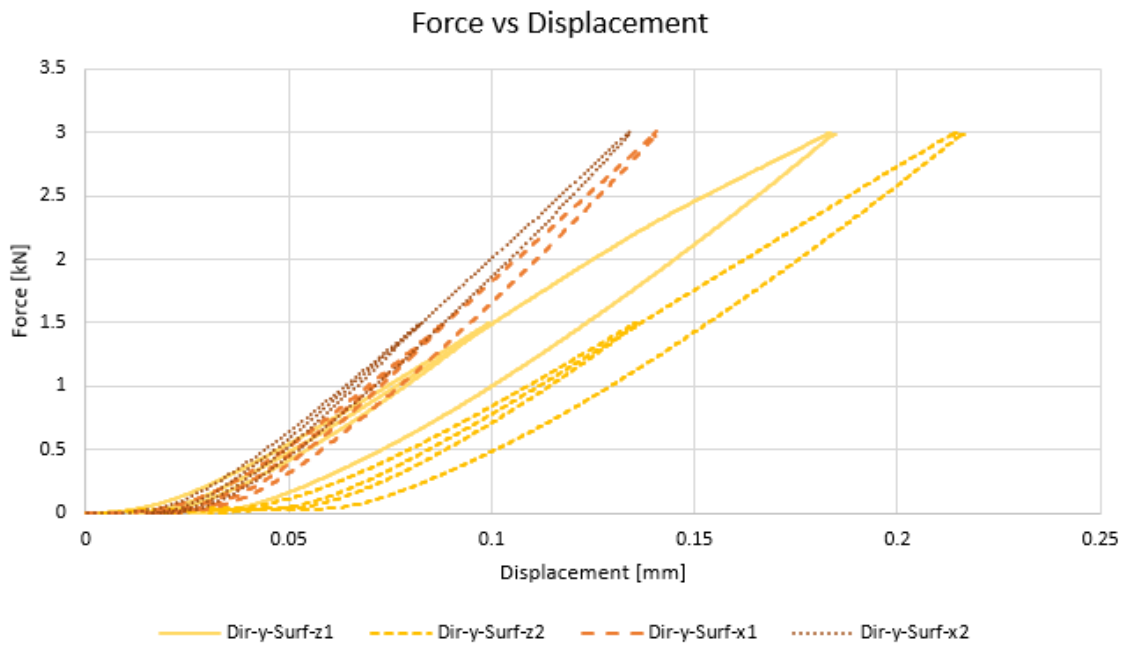
Figure 4.19 Force vs Displacement diagrams when applying force in the y-direction

87
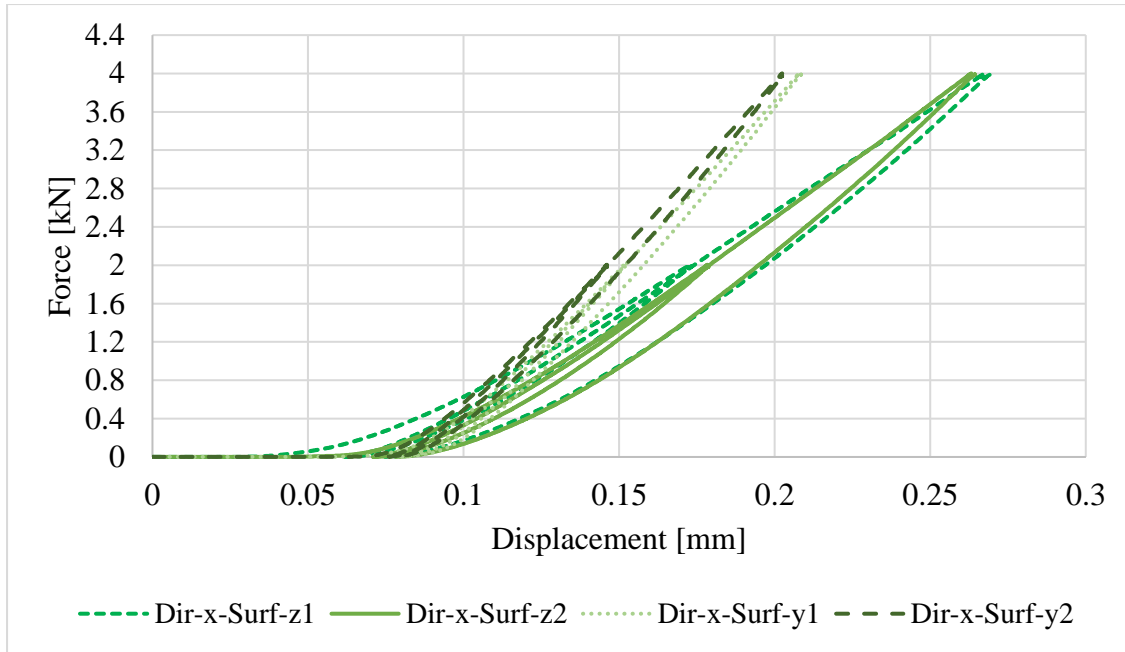
Figure 4.20 Force vs Displacement diagrams when applying force in the x-direction

Figures 4.21 show the stress in x-direction versus the strain in x, y and z-directions, respectively. The strain changes shown in the Figure are the average change in strain in the corresponding direction from the parallel and opposite surfaces. The best fit lines with the corresponding equations were shown on the diagrams. The stress-strain relationships are shown in different colours with σ_x vs ε_x shown in blue, σ_x vs ε_y shown in orange, and σ_x vs ε_y shown in black. The results mentioned above were measured from the DIC camera. The data collected from the DIC camera is a lot less than from the Instron machine and more randomised. Hence, the data trend from the DIC camera is less clear, and the stress-strain relationship was assumed to be linear.

The comparison between the stress-strain relationship σ_x vs ε_x from the Instron machine and the DIC camera is also shown in Figure 4.21. The measurements of the strain in the x-direction from the Instron machine are shown in green. The data of the strain in the x-direction from the Instron machine correlated with the data from the DIC camera, and the small error between them could be caused by the extra blocks added above and below the sample.

88
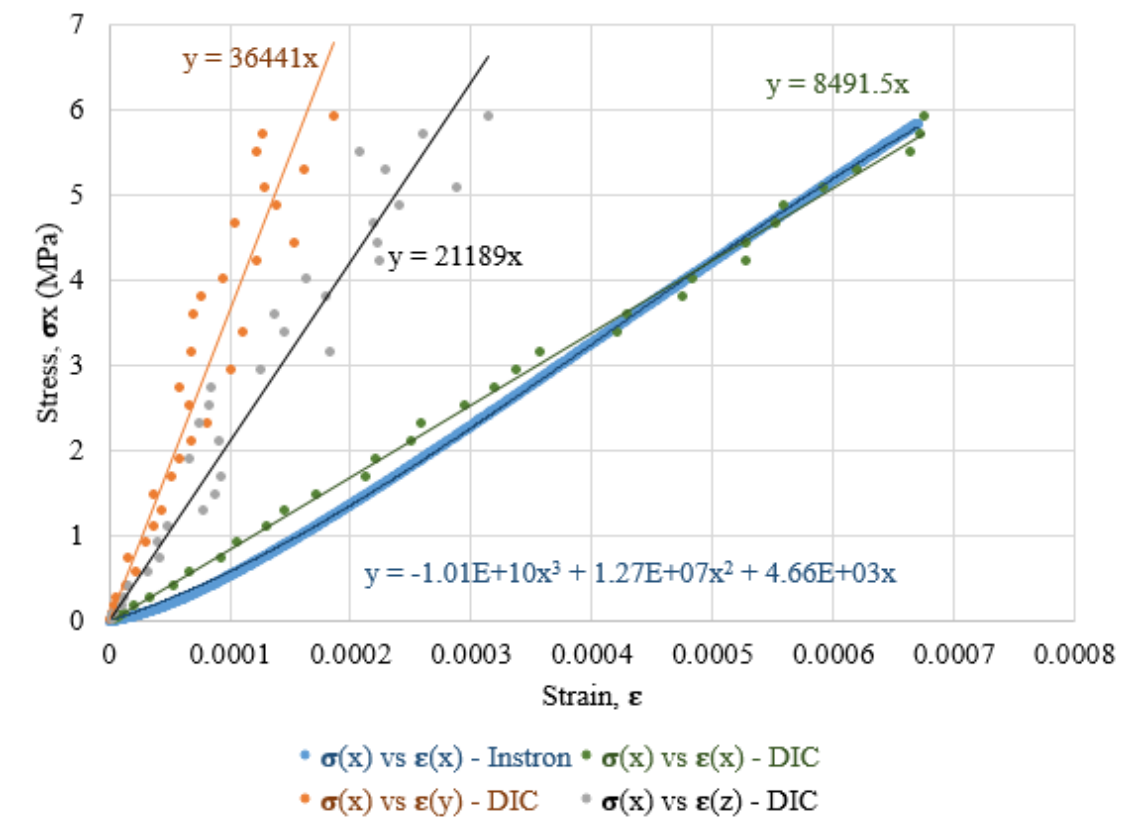
Figure 4.21 Stress in the x-direction vs Strain in x, y, z direction for sample 1

Figure 4.22 shows the calculated Poisson's ratios from tests in Figures 4.13 and 4.14, as mentioned in section 4.3.1. Poisson's Ratio v_{xy}, and v_{xz} were determined from the data shown in Figure 4.21 and v_{yz} is calculated from the test as shown in Figure 4.13. The distributions of the Poisson's ratios shown in Figure 4.22 are unclear, and the linear best fit line was created to observe the trend of the data. From Figure 4.22, it could be seen that the best fit line of v_{xz} and v_{yz} are close to each other and are larger than v_{xy}, these data matched with the material properties identified in Chapter 5.

$y = 0.0018x + 0.3457$

$y = 0.0012x + 0.3746$

$y = 0.0008x + 0.2125$

- V(xy) • V(xz) • V(yz)
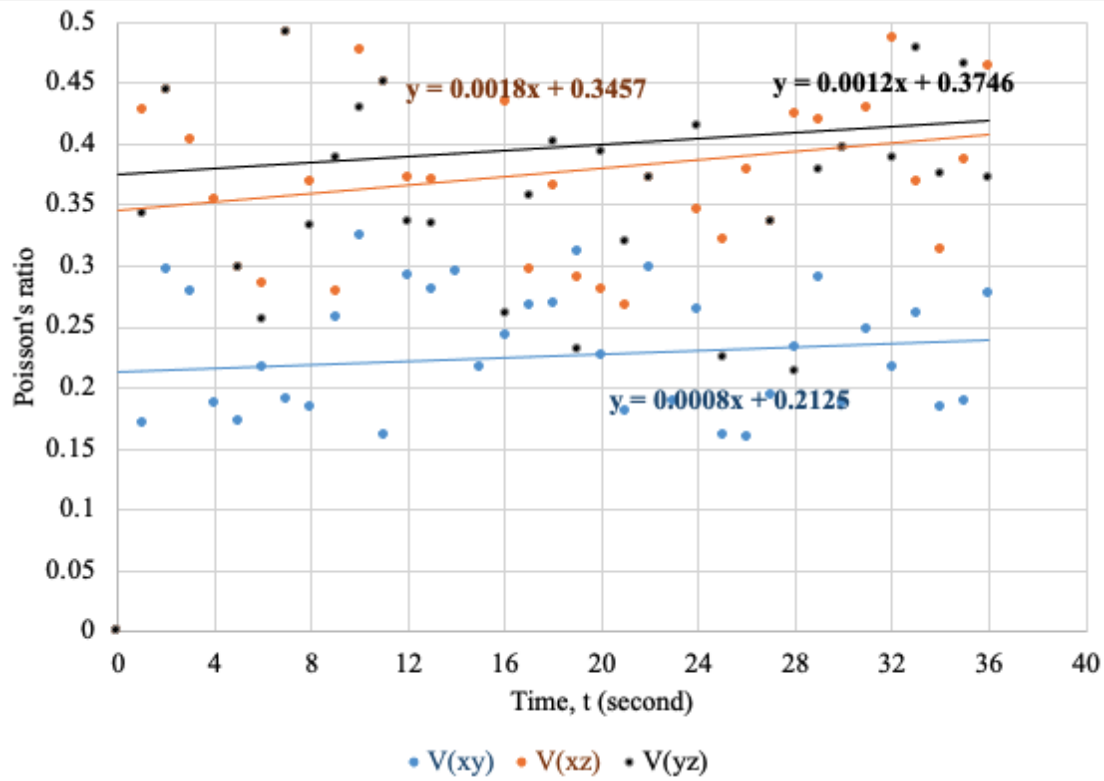
Figure 4.22 Poisson's ratio in all directions vs time

Young's modulus in x-direction was determined from the stress-strain relationship when the forces were applied in the x-direction, as shown in Figure 4.19. Young's modulus in y and z-direction was determined by respectfully rotating the sample and applying compression forces in the y and z-directions. Figure 4.13 shows the set-up of the compression test in the z-direction, which was used to determine the Young's Modulus in the z-direction. Young's modulus in the y-direction was also determined by compressing the sample in the y-direction.

90
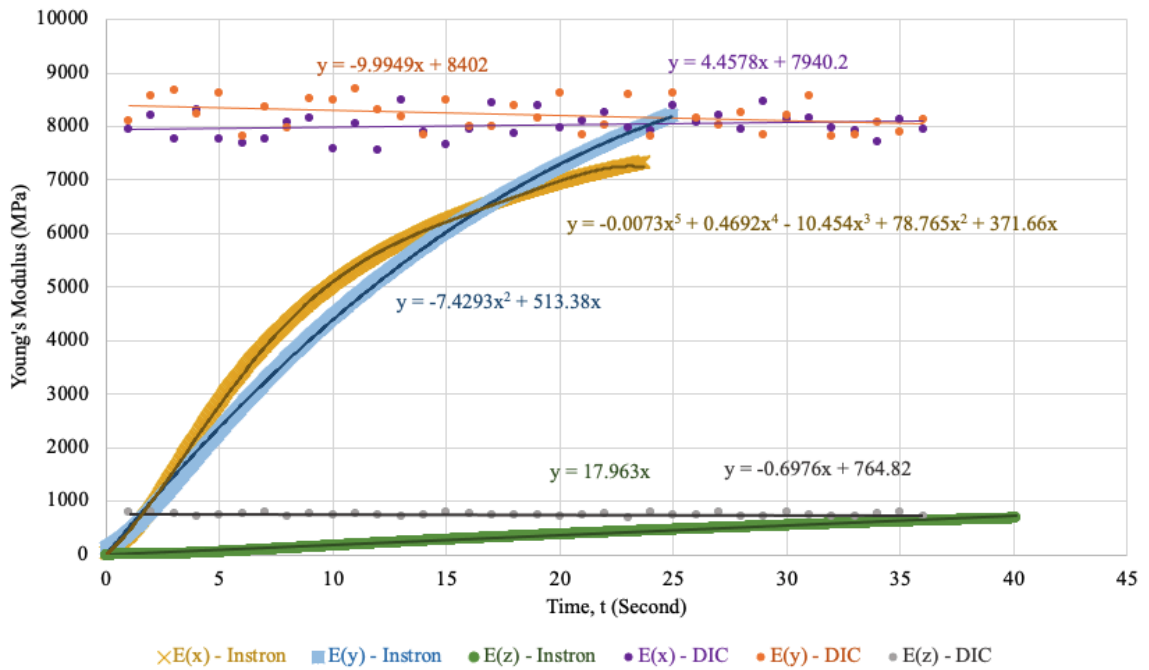
Figure 4.23 Young's modules in all directions vs time

Figure 4.23 shows the calculated Young's modulus E_x, E_y, and E_z using data from the Instron machine and the DIC camera. Note that the trend of Young's modulus calculated from the DIC camera are assumed to be linear because the stress-strain relationships from the DIC data were assumed to be linear. The trend of Young's modulus determined from the Instron machine are nonlinear.

In Chapter 5, the pad friction material would be assumed to be linear. The initial guesses of Young's Modulus E_x, E_y, and E_z and Poisson's ratio v_{xy}, v_{xz}, and v_{yz} of the friction material were the measured data from this section.

The compression data measured from the DIC camera in this chapter would also be used to determine the material properties of the pad friction material as hyperelastic material in chapter 6.

4.4 Summary

The properties of brake pad friction materials could be identified directly from the static experimental data or the model updating method using the dynamic experimental data. This chapter first introduced the fundamental theories of the stress-strain relationship of non-isotropic materials.

Section 4.2 presented the compression test procedure and test data of the brake pad specimens using the strain gauge. Several strain gauges were glued to the measuring surface of the specimen to measure the vertical and horizontal change in strain while stress was applied to the specimen. The data measured from the Instron machine and the strain gauges were presented and analysed. The analysed results were discussed and needed further validation. Therefore, another set of tests was done using a DIC camera to measure the vertical and horizontal change in strain of the test sample.

Section 4.3 showed the information of the test sample, the compression test procedure and test results of the sample measured by the Instron machine and the DIC camera. The graphs of stress-strain relationships of the sample in x, y and z-direction while applying stress in x-direction were shown in Figure 4.21. The Poisson's Ratio v_{xy}, v_{xz}, and v_{yz} and Young's Modulus E_x, E_y, and E_z were estimated and shown in Figures 4.22 and 4.23, respectively.

Chapter 5 Identification of Brake Pad Material Properties

In this chapter, the fundamental theories of the model updating methods using the Sensitivity method and Nastran build-in optimisation algorithm were studied. The main theories for the sensitivity method in this chapter were adapted from (Maia and Montalvão e Silva, 1997) and (Mottershead et al., 2011). The theories and information for the Nastran build-in optimisation method were adapted from the MSC/Nastran software user guildline (MSCSoftware, 2012).

Both model updating methods compare the experimental frequencies and mode shapes of a structure with the analytical ones from the FE model. The Matlab codes were developed for the Sensitivity method and the Nastran Optimisation method to determine the material properties of the selected structure.

Section 5.1 provides the fundamental theories related to the model updating methods, such as the Sensitivity method and the Nastran build-in optimisation algorithm. The procedures of implementing the Sensitivity method and the Nastran build-in optimisation algorithm into Matlab were presented in section 5.2. Section 5.3 shows the implementation of different model updating methods using a rectangular steel plate. In section 5.4, the model updating methods such as the Sensitivity method and the Nastran optimisation method were applied to the brake pad model FER7217 with the dynamic and static tests data shown in chapters 3 and 4. The pad friction material was assumed to be either orthotropic or transversely isotropic in the identification process, and the stress-strain relationship of the pad material was used in the identification process. The updated material properties of the pad friction material using different methods and different material types were implemented in the pad FE model to analyse the frequencies and mode shapes of the pad. These analysed results were compared to determine the material properties of the pad friction material.

5.1 Introduction

The vibration tests were done on the pad using the accelerometer and the robotic hammer to detect the experimental frequencies and mode shapes of the pad (Chapter 3). The FE model of the same pad was created using the software ABAQUS to calculate the theoretical frequencies and mode shapes of the pad section 5.3. Matlab codes were programmed to identify the material properties of the pad using the theoretical frequencies, experimental frequencies with an initial guess of the material properties of the pad and different model updating methods. This section provides the fundamental theories related to the model updating methods, such as the Sensitivity method and the Nastran build-in optimisation algorithm.

5.1.1 Vibration Theory

There are usually n natural frequencies, each associated with its own mode shape, for a MDOF system having n degrees of freedom. The method of determining the natural frequencies from the characteristic equation obtained by equating the determinant to zero also applies to these systems. However, as the number of degrees of freedom increases, the solution of the characteristic equation becomes more complex. The mode shapes exhibit a property known as orthogonality, which often simplifies the analysis of MDoF systems. In this chapter, the pad friction material was assumed to be linear and undamped.

The standard MDoF model of an undamped, autonomous vibrating system is given by the vector differential equation.

$$\mathbf{M}\ddot{\mathbf{x}}(t) + \mathbf{K}\mathbf{x}(t) = \mathbf{0} \tag{5.1}$$

where t denotes the time; $\mathbf{M}$ is an n x n mass matrix, $\mathbf{K}$ is an n x n stiffness matrix, and $\mathbf{x}$ is an n x 1 vector of displacements, or generalized coordinates, each element of which corresponds to a degree of freedom. The over dots denote time derivatives so that $\ddot{\mathbf{x}}$ represent the n x 1 vector of accelerations.

The modal properties associated with equation 5.1 are determined by assuming a solution of the form $\mathbf{x}(t) = \boldsymbol{\varphi}e^{i\omega t}$ where ω is the system natural frequency, i =

$\sqrt{-1}$ and $\boldsymbol{\varphi}$ is the mode shape vector. This substitution yields the algebraic equation.

$$(\mathbf{K} - \omega^2\mathbf{M}) \, \boldsymbol{\varphi} = \mathbf{0} \tag{5.2}$$

Equation 5.2 is called the eigenequation, which is a set of homogeneous algebraic equations for the eigenvector components and forms the basis for the eigenvalue problem. The generalised eigenvalue problem is usually stated as $(\mathbf{A} - \lambda\mathbf{B})\boldsymbol{\varphi} = \mathbf{0}$ where $\mathbf{A}$ and $\mathbf{B}$ are two general square matrixes, and λ is an eigenvalue.

In structural analysis, the representations of stiffness and mass in the eigenequation result in the physical representations of natural frequencies and mode shapes. Therefore, the eigenequation is written in terms of $\mathbf{K}$, ω, and $\mathbf{M}$ as shown in equation 5.2 can be calculated from

$$\det(\mathbf{K} - \omega^2\mathbf{M}) = 0 \tag{5.3}$$

Which leads to n solutions of the eigenvalues, ω_j^2, and eigenvectores, $\boldsymbol{\varphi}_j$, where $j = \{1,2,\dots,n\}$. Mode shape vectors, $\boldsymbol{\varphi}_j$, are normally grouped into the modal matrix $\boldsymbol{\phi}$. Through the concept of orthogonality of normal modes, the MDOF system can be uncoupled to n SDOF system with the following properties:

$$\boldsymbol{\phi}^{\mathrm{T}}\mathbf{M}\boldsymbol{\phi} = \begin{bmatrix} \ddots & 0 & 0 \\ 0 & M_j & 0 \\ 0 & 0 & \ddots \end{bmatrix} \text{ where } j = \{1,2,\dots,n\} \tag{5.4}$$

$$\boldsymbol{\phi}^{\mathrm{T}}\mathbf{K}\boldsymbol{\phi} = \begin{bmatrix} \ddots & 0 & 0 \\ 0 & K_j & 0 \\ 0 & 0 & \ddots \end{bmatrix} \text{ where } j = \{1,2,\dots,n\} \tag{5.5}$$

Diagonal matrices in Equations (5.4) and (5.5) are a result of the orthogonality of the normal modes. These orthotropic properties uncoupled the MDOF system to n SDOF systems. Applying mass-normalisation to equations 5.4 and 5.5:

$$\widetilde{\boldsymbol{\phi}}^{\mathrm{T}}\mathbf{M}\widetilde{\boldsymbol{\phi}} = \mathbf{I} \tag{5.6}$$

$$\widetilde{\boldsymbol{\phi}}^{\mathrm{T}}\mathbf{K}\widetilde{\boldsymbol{\phi}} = \begin{bmatrix} \ddots & 0 & 0 \\ 0 & \omega_j^2 & 0 \\ 0 & 0 & \ddots \end{bmatrix} \text{ where } j = \{1,2,\dots,n\} \tag{5.7}$$

where $\widetilde{\boldsymbol{\phi}}$ is the mass-normalised modal matrix and equation 5.2 can be solved as n uncoupled SDOF systems.

5.1.2 Least Squares Error

The Least squares error is widely used when comparing the difference between two data sets. The Least squares error equation is given as:

$$LS = \sum_{i=1}^{n} r_i{}^2 \tag{5.8}$$

where the squared residuals, $r_i{}^2$, are defined as the relative error between the selected data, in this case, would be the experimental frequencies of the pad and the theoretical frequencies predicted from the FE model:

$$r_i = \frac{\omega_i^{\mathrm{m}} - \omega_i^{\mathrm{FE}}}{\omega_i^{\mathrm{m}}} \tag{5.9}$$

where ω_i^{m} is the i-th element in the experimental frequency vector $\boldsymbol{\omega}^{\mathrm{m}}$ and ω_i^{FE} is the i-th element in the theoretical frequency vector $\boldsymbol{\omega}^{\mathrm{FE}}$. Hence the relative error vector $\mathbf{r}$ between $\boldsymbol{\omega}^{\mathrm{m}}$ and $\boldsymbol{\omega}^{\mathrm{FE}}$ is:

$$\mathbf{r} = \frac{\boldsymbol{\omega}^{m} - \boldsymbol{\omega}^{FE}}{\boldsymbol{\omega}^{m}} \tag{5.10}$$

And the Least squares error can be rewritten as the following:

$$LS = \mathbf{r}' * \mathbf{r} \tag{5.11}$$

where $\mathbf{r}'$ is the transpose vector of $\mathbf{r}$.

The equation of the Least square error between the experimental and theoretical frequencies of the pad friction material was used, and the error was minimised in the Nastran build-in optimisation method.

5.1.3 Applying Constraints to Initial Parameters

The idea of applying equality constraints between parameters is to specify the relationship between parameters and reduce the space of the domain of the feasible solutions in optimisation. Doing so, in theory, is more likely to find a suitable solution of the desired parameters. Three cases were studied and applied in the optimisation method: 1) applying stress-strain relationship between parameters; 2) implementing transversely isotropic instead of orthotropic material for pad via constraints; 3) combining both types of equality constraints.

Applying Stress-Strain Relationship as Constraints

The general stress-strain equation for orthotropic materials is given previously. Some equations (as shown in equation 5.12) are used as equality constraints between parameters among the six.

$$\begin{bmatrix} \sigma_{11} \\ \sigma_{22} \\ \sigma_{33} \end{bmatrix} = \begin{bmatrix} C_{11} & C_{12} & C_{13} \\ C_{12} & C_{22} & C_{23} \\ C_{13} & C_{23} & C_{33} \end{bmatrix} \begin{bmatrix} \varepsilon_{11} \\ \varepsilon_{22} \\ \varepsilon_{33} \end{bmatrix} \tag{5.12}$$

The stress-strain relationship can be found by doing static tests on the pad. The static testing method will be explained later. The general idea of the static test is to find the strain $\varepsilon_{11}, \varepsilon_{22}$ and ε_{33} in x, y and z-direction while applying stress σ_{11} in the x-direction.

Hence the three equality constraints from equation 5.12 are:

$$C_{11} = \frac{\sigma_{11}}{\varepsilon_{11}} - \frac{C_{12} * \varepsilon_{22}}{\varepsilon_{11}} - \frac{C_{13} * \varepsilon_{33}}{\varepsilon_{11}} \tag{5.13}$$

$$C_{22} = -\frac{C_{12} * \varepsilon_{11}}{\varepsilon_{22}} - \frac{C_{23} * \varepsilon_{33}}{\varepsilon_{22}} \qquad\qquad (5.14)$$

$$C_{33} = -\frac{C_{13} * \varepsilon_{11}}{\varepsilon_{33}} - \frac{C_{23} * \varepsilon_{22}}{\varepsilon_{33}} \qquad\qquad (5.15)$$

Pad modelled as Transversely Isotropic Material

As mentioned in section 4.1.1, the three equality constraints can be specified as:
$C_{11} = C_{22}, C_{13} = C_{23}, C_{55} = C_{66}$

Some results are given below with these three additional constraints (referred to as Material constraints).

Combination of All the Six Constraints

The six equality constraints are combined as five in Nastran as the dependent parameters cannot be defined twice. From section 5.4.1 and Appendix A, the parameter C_{22} is more sensitive to out-of-plane frequencies than C_{11}, so equation 5.13 would be updated as equation 5.16 instead.

$$C_{11} = \frac{\sigma_{11}}{\varepsilon_{11}} - \frac{C_{12} * \varepsilon_{22}}{\varepsilon_{11}} - \frac{C_{23} * \varepsilon_{33}}{\varepsilon_{11}} \qquad\qquad (5.16)$$

$$C_{13} = C_{23} \qquad\qquad (5.17)$$

$$C_{22} = \frac{\sigma_{11}}{\varepsilon_{11}} - \frac{C_{12} * \varepsilon_{22}}{\varepsilon_{11}} - \frac{C_{23} * \varepsilon_{33}}{\varepsilon_{11}} \qquad\qquad (5.18)$$

$$C_{33} = -\frac{C_{23} * \varepsilon_{11}}{\varepsilon_{33}} - \frac{C_{23} * \varepsilon_{22}}{\varepsilon_{33}} \qquad\qquad (5.19)$$

$$C_{55} = C_{66} \qquad\qquad (5.20)$$

Other constraints, such as the range of the updating parameters, are defined as ±50% of the initial parameters, whereas the initial parameters are found in static tests.

5.1.4 Sensitivity Method

The sensitivity method is to linearise the non-linear relationship between the measured outputs, such as frequencies and mode shapes of a structure and the selected parameters of the model in need of correction.

Assume a system with a set of initial input parameters, $\boldsymbol{\theta}^0$ and a set of target frequencies, $\boldsymbol{\omega}^m$ (m denotes measured frequencies), the initial output frequencies, $\boldsymbol{\omega}^0$, are calculated from $\boldsymbol{\theta}^0$. The sensitivity method is an optimisation process so that after each iteration, the updated input parameters should reduce the error between $\boldsymbol{\omega}^m$ and the updated output frequencies. Applying the sensitivity method allows a good estimate of the system parameters, $\boldsymbol{\theta}^n$, after n iterations, when the error between the estimated final output frequencies, $\boldsymbol{\omega}^n$, and $\boldsymbol{\omega}^m$ are very small and within a tolerance range.

The sensitivity method is derived from Taylor's Expansion:

$$\omega_i^{k+1} = \omega_i^k + \sum \frac{\partial \omega_i}{\partial \theta_j}\bigg|_{\theta_j} \left(\theta_j^{k+1} - \theta_j^k\right) \tag{5.21}$$

where ω_i^k is the k-th iteration of the i-th frequency and $\boldsymbol{\theta}_j$ is the j-th parameter of the system in the k-th iteration (k denotes the number of iterations calculated for initial input parameters, $k = 0$). The sensitivity matrix $\sum \frac{\partial \omega_i}{\partial \theta_j}$ is normally written as **S** and is defined as:

$$\mathbf{S} = \sum \frac{\partial \omega_i}{\partial \theta_j} = \begin{bmatrix} \dfrac{\partial \omega_1}{\partial \theta_1} & \dfrac{\partial \omega_1}{\partial \theta_2} & \cdots & \dfrac{\partial \omega_1}{\partial \theta_j} \\ \dfrac{\partial \omega_2}{\partial \theta_1} & \dfrac{\partial \omega_2}{\partial \theta_2} & \cdots & \dfrac{\partial \omega_2}{\partial \theta_j} \\ \vdots & \vdots & \ddots & \vdots \\ \dfrac{\partial \omega_i}{\partial \theta_1} & \dfrac{\partial \omega_i}{\partial \theta_2} & \cdots & \dfrac{\partial \omega_i}{\partial \theta_j} \end{bmatrix} \tag{5.22}$$

Theoretically, the sensitivity matrix can be calculated using the mass and stiffness matrices of the system. Each $\frac{\partial \omega_i}{\partial \theta_j}$ in the Sensitivity matrix can be

rewritten into the mass and stiffness matrices of the system shown in equation 5.23 below:

$$\frac{\partial \lambda_i}{\partial \theta} = \frac{\boldsymbol{\varphi}_i^{\mathrm{T}}(\frac{\partial \mathbf{K}}{\partial \theta} - \lambda_i \frac{\partial \mathbf{M}}{\partial \theta})\boldsymbol{\varphi}_i}{\boldsymbol{\varphi}_i^{\mathrm{T}}\mathbf{M}\boldsymbol{\varphi}_i}$$

(5.23)

If modes are mass-normalised, the eigenvalue sensitivity becomes

$$\frac{\partial \lambda_i}{\partial \theta} = \boldsymbol{\varphi}_i^{\mathrm{T}}(\frac{\partial \mathbf{K}}{\partial \theta} - \lambda_i \frac{\partial \mathbf{M}}{\partial \theta})\boldsymbol{\varphi}_i$$

(5.24)

However, in real-world applications, the structures are complicated, and it is often very difficult or inconvenient to use the mass and stiffness matrices of the model to determine sensitivities. So approximate sensitivities are found using the finite-difference. In this case, for each column of matrix $\mathbf{S}$, $\boldsymbol{\theta}_j$ is changed slightly by $\delta\boldsymbol{\theta}_j$, and the frequencies $\boldsymbol{\omega}_j^{\mathrm{new}}$ at $(\boldsymbol{\theta}_j + \delta\boldsymbol{\theta}_j)$ are calculated. Therefore, the values of the i-th row and j-th column of sensitivity matrix $\mathbf{S}$ is calculated as:

$$\frac{\partial \omega_i}{\partial \theta_j} \cong \frac{\omega_i^{\mathrm{new}} - \omega_i}{\delta \theta_j}$$

(5.25)

This method to find the sensitivity matrix $\mathbf{S}$ is used in the following examples for the thin rectangular plate and the full brake pad.

Equation 5.21 above shows that the measured frequencies $\boldsymbol{\omega}^{\mathrm{m}}$ can be written as a function of the theoretical frequencies, experimental frequencies and system parameters. Equation 5.21 can be rearranged to yield the improved system parameter vector, $\boldsymbol{\theta}^{k+1}$ as shown in equation 5.26 below.

$$\boldsymbol{\theta}^{k+1} = \boldsymbol{\theta}^k + (\mathbf{S}^{\mathrm{T}}\mathbf{S})^{-1}\mathbf{S}^{\mathrm{T}}(\boldsymbol{\omega}^{\mathrm{m}} - \boldsymbol{\omega}^k)$$

(5.26)

The number of frequencies used should always be equal to or greater than the number of parameters to be updated. Case 1: if the number of frequencies used is equal to the number of parameters used, the sensitivity matrix $\mathbf{S}$ would be a square matrix and rearranging the equation is simple. Case 2: if the number of frequencies used is larger than the number of parameters used, the sensitivity

matrix **S** would be a rectangular matrix with the number of rows > the number of columns. In the second case, equation 5.21 cannot be rearranged because the sensitivity matrix cannot be inverse in the same way as the square matrix. Therefore, equation 5.21 becomes equation 5.26, where the inverse of the sensitivity matrix is obtained as $(\mathbf{S}^T\mathbf{S})^{-1}\mathbf{S}^T$.

5.1.5 Nastran Build-in Optimisation Method

Another way of identifying the parameters, such as the material properties of the pad friction material, is to use the Nastran build-in optimisation algorithm. Nastran uses SOL 200 solution sequence, a powerful method mostly used for shape optimisation.

An optimisation problem minimises a real function $f(x)$ by systematically choosing input values from within an allowed set and computing the value of the function. In this case, the real function $f(x)$ is the Least squares error between the theoretical frequencies and the experimental frequencies of the pad.
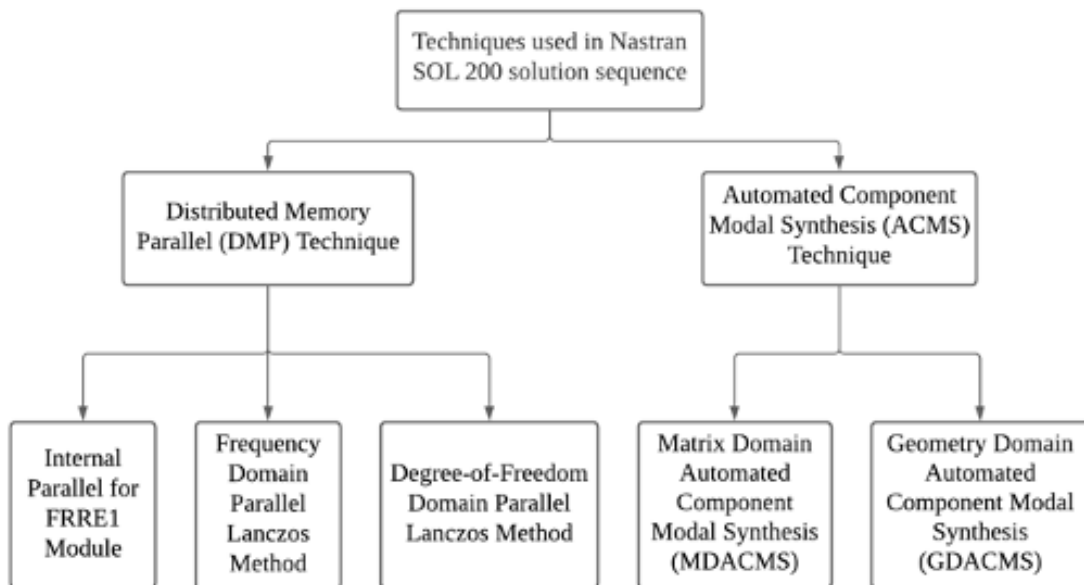
Figure 5.1 Flowchart of Techniques used in Nastran SOL 200

Nastran SOL 200 solver involves the Distributed Memory Parallel (DMP) technique and the Automated Component Modal Synthesis (ACMS) Technique. As shown in the flowchart in Figure 5.1, the DMP technique can be divided into three types: Internal parallel for FRRE1 module, Frequency domain parallel Lanczos method, and DoF domain parallel Lanczos method; and ACMS can be divided into two types: Matrix domain ACMS and Geometry domain ACMS.

The techniques used in the identification process for the material properties of the pad friction material are the Frequency domain parallel Lanczos method or the DoF domain parallel Lanczos method. The Lanczos algorithm is an iterative method that finds the m eigenvalues and eigenvectors of an $n*n$ Hermitian matrix (Lanczos, 1950). The Lanczos algorithm computes an orthonormal basis $\{\mathbf{q}_1, \mathbf{q}_2, \dots\dots, \mathbf{q}_m\}$ of the Krylov subspace $\mathcal{K}^m(\mathbf{x})$.

In general, the natural basis of the Krylov subspace $\mathcal{K}^j(\mathbf{x}) = \mathcal{K}^j(\mathbf{x}, \mathbf{A})$ is evidently $\{\mathbf{x}, \mathbf{Ax}, \dots\dots, \mathbf{A}^{j-1}\mathbf{x}\}$. Since the vectors $\mathbf{A}^k\mathbf{x}$ converge to the direction of the eigenvector corresponding to the largest eigenvalue of $\mathbf{A}$, the above basis is often badly conditioned with increasing dimension j. Hence, the Gram-Schmidt orthogonalisation process is applied to the natural basis of the Krylov subspace, as shown in equation 5.27.

$$\mathbf{y}_j := A^j\mathbf{x} - \sum_{i=1}^{j} \mathbf{q}_i\mathbf{q}_i^* A^j\mathbf{x} \tag{5.27}$$

$$\mathbf{q}_{j+1} = \frac{\mathbf{y}_j}{\|\mathbf{y}_j\|} \tag{5.28}$$

where $\{\mathbf{q}_1, \mathbf{q}_2, \dots\dots, \mathbf{q}_i\}$ is the orthonormal basis for $\mathcal{K}^i(\mathbf{x})$, $i \leq j$. By normalizing the resulting vector as shown in equation 5.28, the orthonormal basis of $\mathcal{K}^{j+1}(\mathbf{x})$ is determined as $\{\mathbf{q}_1, \mathbf{q}_2, \dots\dots, \mathbf{q}_{j+1}\}$, which is called the Arnoldi basis in the most general case. If matrix $\mathbf{A}$ is symmetric or Hermitian, then this basis is known as the Lanczos basis.

Below is how the Krylov subspace is converted from the natural basis to the orthonormal basis.

$$\mathcal{K}^{j+1}(\mathbf{x}, \mathbf{A}) = \mathcal{R}([\mathbf{x}, \mathbf{Ax}, \dots\dots, \mathbf{A}^j\mathbf{x}]) \qquad (\mathbf{q}_1 = \mathbf{x}/\|\mathbf{x}\|)$$

$$\mathcal{K}^{j+1}(\mathbf{x}, \mathbf{A}) = \mathcal{R}([\mathbf{q}_1, \mathbf{Aq}_1, \dots\dots, \mathbf{A}^j\mathbf{q}_1]) \qquad (\mathbf{Aq}_1 = \alpha\mathbf{q}_1 + \beta\mathbf{q}_2, \beta \neq 0)$$

$$\mathcal{K}^{j+1}(\mathbf{x}, \mathbf{A}) = \mathcal{R}([\mathbf{q}_1, \alpha\mathbf{q}_1 + \beta\mathbf{q}_2, \mathbf{A}(\alpha\mathbf{q}_1 + \beta\mathbf{q}_2), \dots\dots, \mathbf{A}^{j-1}(\alpha\mathbf{q}_1 + \beta\mathbf{q}_2)])$$

$$\mathcal{K}^{j+1}(\mathbf{x}, \mathbf{A}) = \mathcal{R}([\mathbf{q}_1, \mathbf{q}_2, \mathbf{A}\mathbf{q}_2, \ldots \ldots, \mathbf{A}^{j-1}\mathbf{q}_2])$$

$$\vdots$$

$$\mathcal{K}^{j+1}(\mathbf{x}, \mathbf{A}) = \mathcal{R}([\mathbf{q}_1, \mathbf{q}_2, \mathbf{q}_3, \ldots \ldots, \mathbf{q}_{j-1}, \mathbf{A}\mathbf{q}_j])$$

Converting from equations 5.27 and 5.28, the component $\mathbf{r}_j$ of $\mathbf{A}\mathbf{q}_j$ orthogonal to $\{\mathbf{q}_1, \mathbf{q}_2, \ldots \ldots, \mathbf{q}_j\}$ is given by

$$\mathbf{r}_j = \mathbf{A}\mathbf{q}_j - \sum_{i=1}^{j} \mathbf{q}_i(\mathbf{q}_i^* \mathbf{A}\mathbf{q}_j) \tag{5.29}$$

$$\mathbf{q}_{j+1} = \frac{\mathbf{r}_j}{\|\mathbf{r}_j\|} \tag{5.30}$$

If $\|\mathbf{r}_j\| > 0$ then equation 5.29 can be rewritten as

$$\mathbf{A}\mathbf{q}_j = \sum_{i=1}^{j+1} \mathbf{q}_i(\mathbf{q}_i^* \mathbf{A}\mathbf{q}_j) = \sum_{i=1}^{j+1} \mathbf{q}_i h_{ij} \tag{5.31}$$

where $h_{ij} = \mathbf{q}_i^* \mathbf{A}\mathbf{q}_j$

Suppose $\mathbf{Q}_k = \{\mathbf{q}_1, \mathbf{q}_2, \ldots \ldots, \mathbf{q}_k\}$ and $\mathbf{H}_k \in \mathbb{F}^{(k+1) \times k}$, then

$$\mathbf{A}\mathbf{Q}_k = \mathbf{Q}_k \mathbf{H}_k \tag{5.32}$$

$$\mathbf{Q}_k^* \mathbf{A}\mathbf{Q}_k = \mathbf{Q}_k^* \mathbf{Q}_k \mathbf{H}_k = \mathbf{H}_k \tag{5.33}$$

And $\mathbf{H}_k$ is either symmetric or Hermitian for the Lanczos algorithm.

The Nastran SOL 200 provides an automatic optimisation process to identify the desired parameters. The basic theory of the Lanczos method is presented in this section without further details of the procedure within the Nastran software.

5.2 Matlab Programs for Model Updating Methods

Two sets of Matlab programs were developed, one for the Sensitivity method and the other for the Nastran SOL 200 algorithm. The basic ideas and processes for each developed set of programs are explained in this section.

103

5.2.1 Matlab Procedures for Sensitivity Method

The theory behind the Sensitivity method was explained in section 5.1.4. Equation 5.26 was used as the function of the iteration process in the Matlab program.

Figure 5.2 shows the flowchart of the procedures involved in the Matlab codes for the Sensitivity method, and the steps are explained in detail below.

Note that the blocks shown in white are the manual processes that need the user to operate; the blocks in green are the automatic processes computed in Matlab. In the procedure, MS is a short term for Manual procedures of the Sensitivity method and AS means Automatic procedure for the Sensitivity method. MN in Figure 5.3 is the short term for Manual procedures of the Nastran optimisation method, which are used in section 5.2.2.
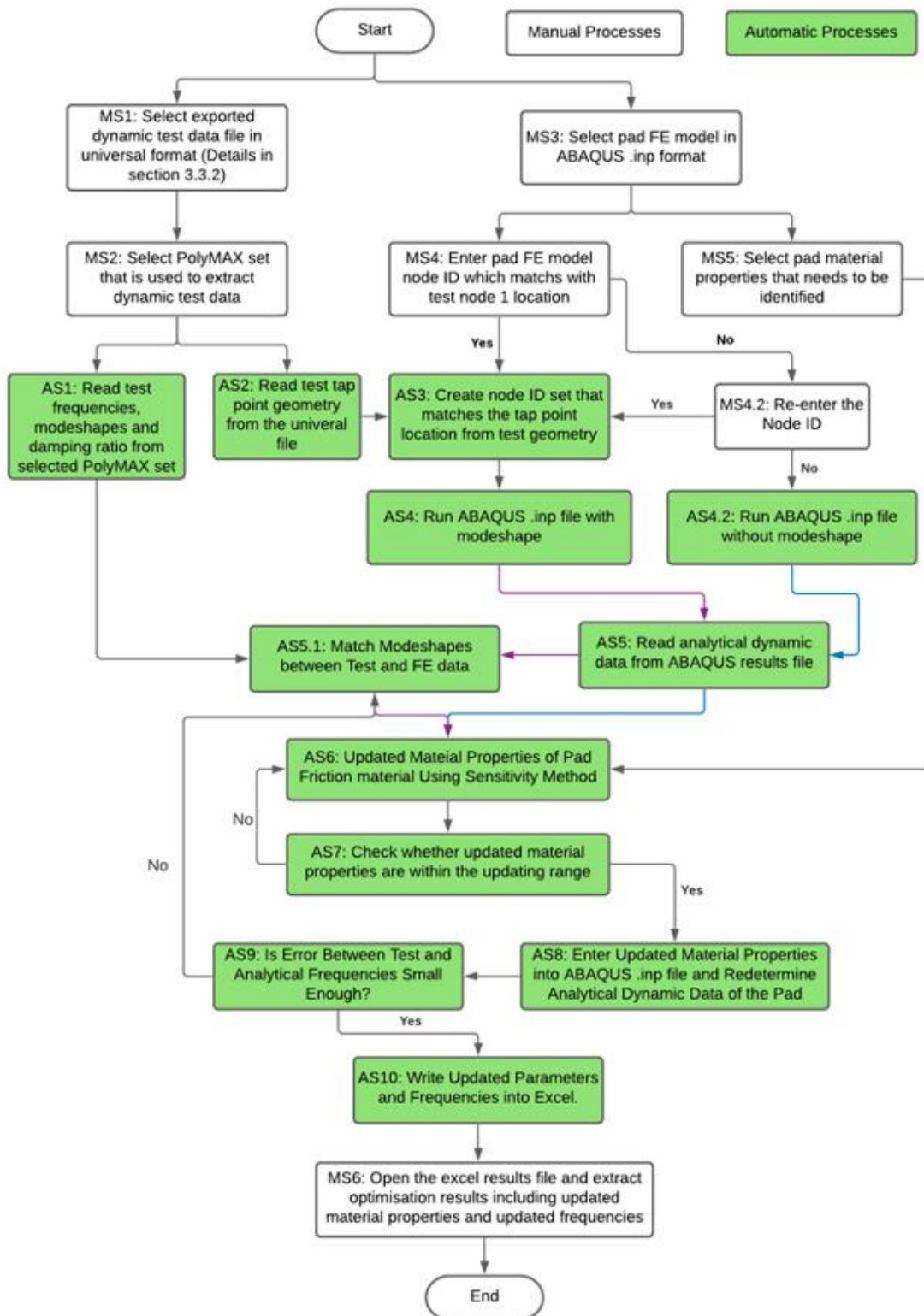
Figure 5.2 Overview of the Matlab Procedures using Sensitivity Method

105
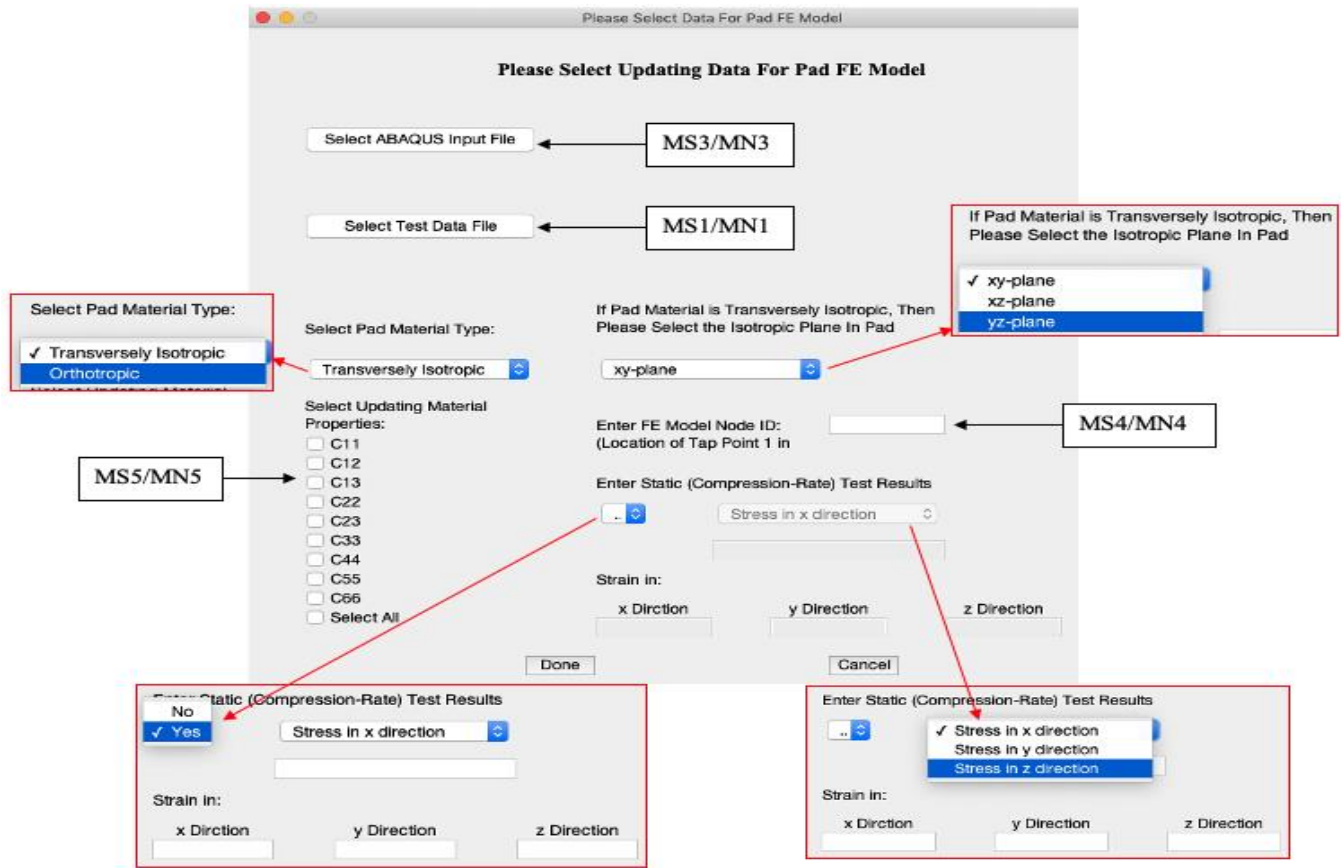
Figure 5.3 Manual Process to select updating FE model and test data in Matlab

Figure 5.3 shows the input window of the developed Matlab program, and steps MS1, 3, 4 and 5 are presented in the Figure. The pad friction material could be updated as either orthotropic or transversely isotropic materials. If the pad material is selected as transversely isotropic material, the isotropic plane could be selected depending on the global coordinate system of the pad. The compression test data could be entered as additional constraints of the updating process (section 5.1.3).

MS1, MS2, MS4, AS1, AS2 and AS3 are explained in section 3.3.2.

MS3: The FE model of the brake pad would be selected, and the file would be in .inp format, which is the input file for the ABAQUS software.

MS4.2:

MS5: Select the material properties that are needed to be updated. If the pad is said to be transversely isotropic, for example, in the xy-plane, then if C11 is selected for updating, C22 would be updated as C11=C22 is a constraint in this case.

AS4: Call ABAQUS software within Matlab code.

AS5: Frequencies (and mode shapes) analysed from ABAQUS would be summarised in the data file format .dat. Matlab reads the analytical frequencies and mode shapes from the .dat file automatically.

AS5.1: If the analytical mode shapes are available, the test and analytical mode shapes are matched. The frequencies with matched mode shapes are used in the Sensitivity method to update the selected material properties. The program will stop with a warning sign if the number of independent material properties selected is larger than the number of matched mode shapes. Users need to either enter constraints to reduce the number of independent updating parameters or collect more reliable test mode shapes for the updating process. Otherwise, the iteration method would proceed without matching the mode shapes and assume the test and analytical modes matches in ascending order.

AS6: Equation 5.26 in section 5.14 is the equation used for the optimisation process. The latest updated material properties, θ^{k+1}, of the pad from the iteration process are calculated and compared with the material properties from

the previous step, $\boldsymbol{\theta}^k$. The stoping criteria would be the Least squares error between $\boldsymbol{\theta}^{k+1}$ and $\boldsymbol{\theta}^k$, smaller or equal to 0.01%.

The size of the sensitivity matrix depends on the number of paired test and analytical frequencies and the selected updating material properties. If the data for both the test mode and FE mode shapes are collected, the frequencies would be paired using MAC values mentioned in section 3.1.3; this match between the test and analytical modes would occur in every iteration. Otherwise, the test and analytical frequencies and mode shapes of the same mode number would be matched.

When calculating the Sensitivity matrix $\mathbf{S}$, the used test, analytical frequencies and material properties are normalised using the analytical data from the initial inputted parameter.

AS7: As mentioned in section 5.1.4 before, the mass and stiffness matrix of a large FE model of a system could be difficult to find and costly for computational implementation. Therefore, the approximate sensitivity matrix with a small increment of $\delta\boldsymbol{\theta}_j$ was used in the sensitivity matrix (equation 5.25). Theoretically, $\delta\boldsymbol{\theta}_j$ should be infinitely small, but in reality, the value of $\delta\boldsymbol{\theta}_j$ could be set large, which lead to incorrect updating results. An example is shown in Figure 5.4, $\delta\boldsymbol{\theta}_j^1$ leads to an incorrect updating result whereas $\delta\boldsymbol{\theta}_j^2$ approach to the desired answer.
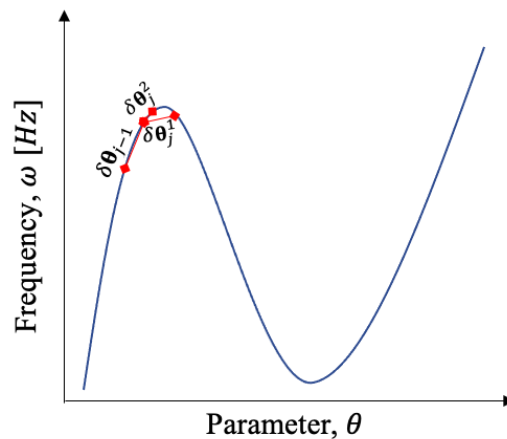
Figure 5.4 Example of the effect of different $\delta\boldsymbol{\theta}_j$ values towards updated results

Constraints must be applied to the parameters so the updated parameters are within a reasonable range. Because the updating parameters have physical

meanings and unsuccessful updated parameters (i.e. Poisson's ratio larger than 1) would fail to update the FE model.

Therefore the process in AS7 checks whether the updated parameters are within the set range, which are +/- 50% of the initial parameters from the compression test. If the parameter exceeds the range, the value of $\delta\theta_j$ reduces, and the updating process would repeat from the updated results determined from the previous iteration.

AS8: The parameters are implemented into the pad FE model to update the frequencies and mode shapes of the pad.

AS9: Updated analytical mode shapes are compared with the test mode shapes to avoid any shifts between analytical modes during the updating process. The Least squares error is calculated between matched updated analytical and test frequencies. The stopping criteria in the Sensitivity method is soft convergence. A soft convergence means that if the selected design variables have not changed significantly after a few iterations, the results of the variables from the previous analysis would be assumed as the satisfactory outcome, and the optimisation would stop with the currently updated variables (Mscsoftware, 2012). If the stoping criteria is not met, the process repeat from step AS5.1 or AS6 depending on whether the mode shapes matching process was used in the previous procedure or not.

AS10: Read and extract updated material properties and frequencies from the ABAQUS data file. Write original material properties, updated material properties, test frequencies, original analytical frequencies with relative error, and updated analytical frequencies with relative error into an excel file.

5.2.2 Matlab Procedures for Nastran SOL 200 Algorithm

The theory behind the Nastran SOL 200 optimisation method is shown in section 5.1.5. Since the optimisation method is built within the Nastran software and the procedures are running automatically during the updating process, this section does not explain the optimisation method in detail. The Matlab codes developed for this method mainly convert the ABAQUS and Nastran input and output files because of the different set-up between the two software.
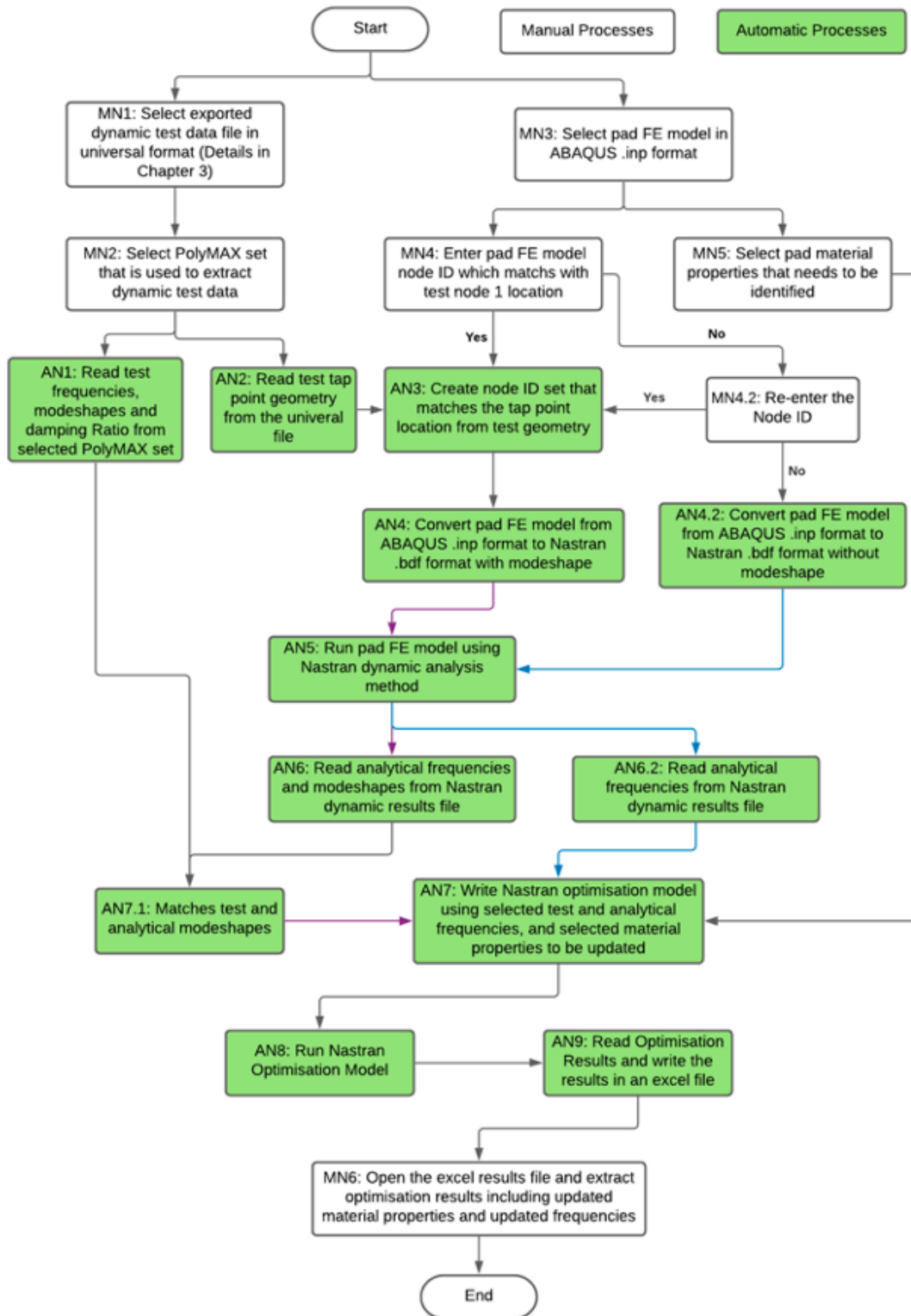
Figure 5.5 Overview of the Matlab Program Procedures using Nastran SOL 200

110

The input window of the Nastran updating procedure is the same as for the Sensitivity method in Figure 5.3 section 5.2.1. However, the procedures in Matlab are very different. The flowchart in Figure 5.5 shows the procedures involved in the Matlab codes for the Nastran build-in method, and the steps are explained in detail below.

Note that the blocks shown in white are the manual processes that need the user to operate; the blocks in green are the automatic processes computed in Matlab. In the procedure, MN is a short term for manual procedures of the Nastran Method, and AN means Automatic procedure for the Nastran Method.

MN1, MN2, MN3, MN4, MN4.2, MN5, AN1, AN2, AN3, and AN7.1 are the same steps with the Sensitivity Method.

AN4: The format between the FE model input file in ABAQUS and Nastran are very different. ABAQUS provides a function to convert from the ABAQUS input file to the NASTRAN input file. However, many problems occur when using this function provided by ABAQUS.

Firstly, the maximum number of digits accepted in ABAQUS is nine and in Nastran is 8. Hence, a problem would occur when the node IDs of the FE model in ABAQUS are in digits of 9. For example, if the node IDs are 100000000 and 100000001 in ABAQUS, they would both occur as 10000000 in Nastran, which would be considered as the same point. Therefore, the node IDs are renumbered when converting the input file. If the mode shapes are considered within the updating process, then the node ID selected for test point 1 would be numbered as node ID 1 in the FE model and the estimated mode shape points in the FE model would be numbered regarding the test point numbers.

Another important format difference between the two software is that ABAQUS allows the user to define transversely isotropic materials using the material type called ENGINEERING CONSTANT, which uses the Engineering constants such as Young's Modulus, Poisson's Ratio and Shear Modulus of the pad friction material; whereas in Nastran, the material can also be defined as transversely isotropic material using MAT9 but using Elastic constants (equation 4.4-4.13). The ABAQUS built-in file-converting method does not transfer the ENGINEERING CONSTANT material card into the Nastran input file, and the

developed Matlab code ensured that the input material was correctly converted with the correct orientation system.

The possibility of the global coordinate system difference between the two software is also considered in the Matlab code where the ABAQUS converting system did not consider.

AN5: Call the Nastran software from Matlab code.

AN6: Read the pad analytical frequencies and mode shapes from the FE model in the Nastran output .f06 format.

AN7/AN7.1: The optimisation process in the Nastran software is automatic, but a few inputs must be set up before the optimisation procedure; these setups are shown in Figure 5.3 and explained below:

1. The selected material properties for an update in MN5 are read from the input file selected in MN3, and the upper and lower updating boundary conditions (+/- 30%) are set up depending on the initial parameters input.

2. If the constraints of the parameters are selected, for example, the transversely isotropic material is chosen, and the xy-plane is the isotropic plane, then if both C11 and C22 are selected as updating parameters, the updated C11 and C22 are equal.

3. If a node ID is entered in MN4, then test and analytical mode shapes and matched, and the frequencies with matched mode shapes are used for updating. If the number of matched mode shapes are smaller than the number of updating parameters, the progress will check whether there are constraints between material properties, reducing the number of independent parameters. If the number of independent parameters is larger, the program will stop, and the user needs to either reduce the number of independent updating parameters or increase the number of reliable test mode shapes. Alternatively, users can update material properties without matching mode shapes by not entering the node ID in MN4.

4. The Least squares error function between the test and analytical frequencies is written in the optimisation file, calculated in the iteration process.

AN8: Once the optimisation file is created, the Matlab code calls the Nastran software and automatically determine the suitable parameters which minimise

112

the Least squares error function. The stopping criteria in the Nastran optimisation method is soft convergence. The explaination of soft convergence is in section 5.2.1 step AS9. The soft convergence is the default converging method in Nastran SOL 200.

AN9: The updated parameters would be saved in the file in .csv format, extracted and applied to the pad FE model to determine the updated analytical frequencies. A final optimisation results file will be created in excel format with '_Results_Comparison' at the end of the file name.

fer7217_no_mode_all_para_transiso_Results_Comparison

The results file would contain two sheets:

1. Info: The information about the selected FE model, selected test data file, selected pad material type, and the updated pad material properties.

2. Results: This contains the original and updated material properties. The columns highlighted in blue are the selected material properties that are updated. The resulting file also shows the test frequencies, the original and updated analytical frequencies from the pad FE model, and the relative error between (matched) test and original/updated analytical frequencies.

5.3 Different Material Identification Methods

Vibration test data of the pad and the plate were previously collected from Chapter 3, and compression test data of the pad friction material were collected from Chapter 4. These test data are used in the model updating process in this chapter.

5.3.1 Material Identification of Steel Plate

The thin rectangular plate shown in Figures 3.1 and 3.2 is used to study two types of parameter updating methods, the Sensitivity method and the Nastran optimisation method. More information about the size and density of the plate can be found in section 3.2.1. Since the shape of the plate is simple, and the

number of testing mesh grids is limited (11*7), the FE meshing grid of the plate in ABAQUS is also not dense (22*14), as shown in Figure 5.6.
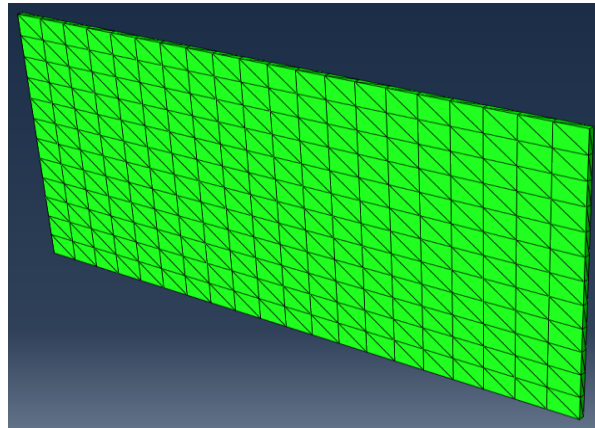
Figure 5.6 ABAQUS FE Model of The Thin Rectangular Steel Plate

5.3.1.1 Sensitivity Method

It is assumed that the material of the plate is isotropic and probably made of mild steel. The updating material properties are the Young's Modulus, *E*, and Poisson's Ratio, ν, in all directions. An initial estimation of the material properties of the plate was made: E = 190GPa and ν = 0.2. The sensitivity method was applied to the plate using equation 5.26. The first ten analytical frequencies above 1000Hz were determined with each set of updated parameters.

Since the number of updating parameters is two, two or more paired analytic and test frequencies must be used in the identification process. The test and analytical frequencies were paired using the Modal Assurance Criterion (MAC) value mentioned in section 3.1.3. MAC values were calculated using measured and analytical eigenvectors, and the modes are paired if the MAC value is near 1.

Four sets of paired frequencies were used to calculate the Sensitivity matrix and determine the material properties of the plate. Moreover, the analytical frequencies of the plate in the higher range were estimated using the updated material properties. The estimated analytical frequencies were compared with the test frequencies, and the Least squares error between the paired frequencies were calculated to observe the predictability of the analytical frequencies.

Figure 5.7 shows the Least squares error using updated plate material properties after each iteration for 1) four paired test and analytical frequencies, 2) ten paired

tests and estimated analytical frequencies. Note that the calculated Least squares errors from using ten paired frequencies are larger than using four paired frequencies because: firstly, the error between the estimated analytical frequencies and the test frequencies are larger than between the paired frequencies used in the identification method; also, the error between the higher analytical and test frequencies is larger than between the lower paired frequencies. However, although the Least squares errors from 10 paired frequencies are larger in comparison, they are still within satisfactory range (0.0185%). Hence, the updated material properties of this plate are Young's modulus, E = 211.813GPa and Poisson ratio v = 0.271.
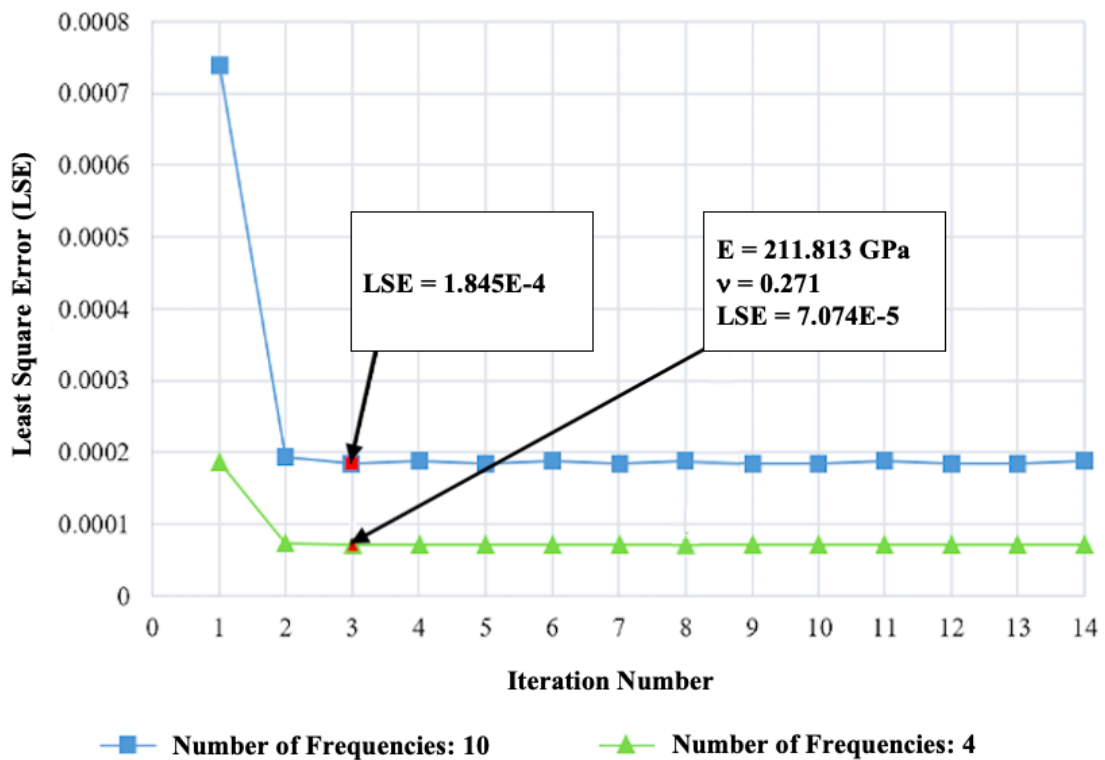
Figure 5.7 Least Squares Error calculated using different number of frequencies vs Iteration Number from the Sensitivity method

The identification process of the plate material properties using the Sensitivity method stopped at iteration five because the updating parameters have not changed significantly after three iterations. However, a few more iterations were run, which showed no significant changes in the updating parameters after the fifth iteration and validated the stopping criteria of the program.

115

5.3.1.2 Nastran Optimisation Method

The FE model used in the Nastran optimisation method was based on the ABAQUS FE model shown in Figure 5.6 and converted into the Nastran readable format (explained in section 5.2.2). The initial estimation of the updating parameters was the same as in section 5.3.1.1: E = 190GPa and ν = 0.2.

The optimisation function was defined using the Least squares error between frequencies. A constraint was applied to the updating parameters to ensure that the updated material properties would not go out of range and lose their physical meanings. The constraint for Young's Modulus is that 190GPa $\leq$ E $\leq$ 220GPa, and the constraint for Poison's Ratio is 0.2 $\leq$ ν $\leq$ 0.4. These constraints are slightly wider than their actual ranges. Six iterations were run for 2 minutes, and the first four paired analytical and test frequencies above 1000Hz were used to calculate the updated parameters from the Least squares error function. Furthermore, Least squares errors were calculated with all ten frequencies to observe the predictability of higher frequencies using this method.
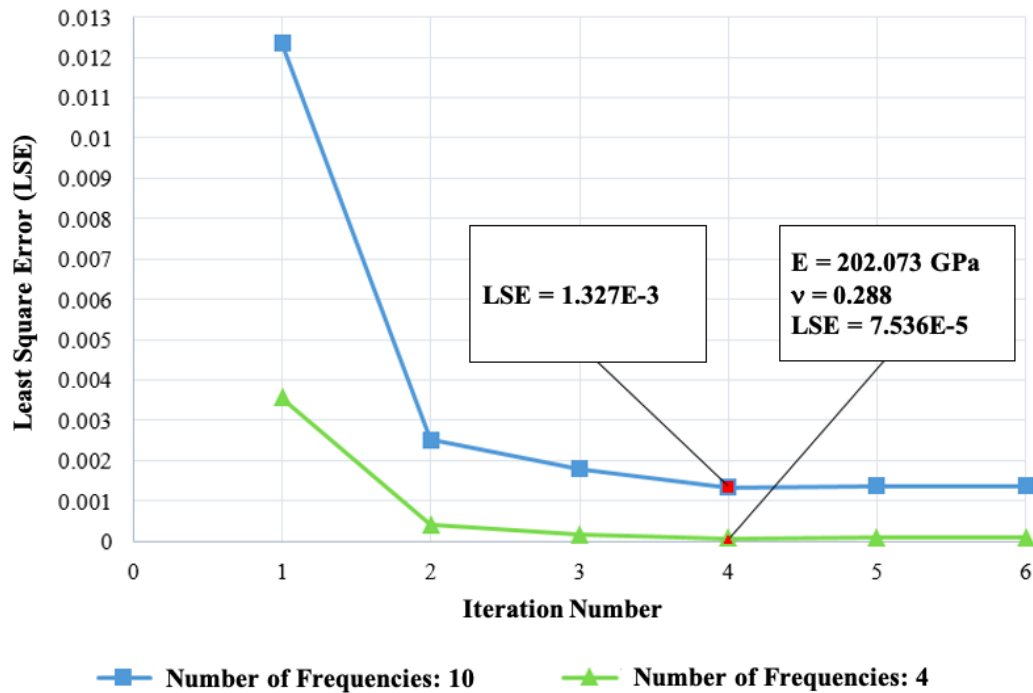
Figure 5.8 Least Squares Error calculated using different number of frequencies vs Iteration Number from Nastran Software

Figure 5.8 shows the calculated Least squares error for different frequencies with updated parameters from each iteration. The Least squares error between the plate's experimental frequencies and the theoretical frequencies, including all the predicted higher frequencies, was found to be 0.1327%. This error is very small and acceptable considering the high-frequency range. Therefore the estimated material properties of this plate using the Nastran optimisation method are Young's modulus, $E = 202.073$GPa and Poisson ratio, $\nu = 0.288$.

5.3.1.3 Comparison of updated parameters from two updating procedures

Table 5.1 and Table 5.2 show the comparison of results from the two updating methods, including the initial and updated parameters, the time and number of iterations taken, the test and updated frequencies and their relative Least squares errors.

Table 5.1 shows the results of the chosen updated parameters based on the Least squares error of 4 frequencies. Nastran software ran the updating method faster, but the Least squares error is larger (still very small and within the acceptable range).

Table 5.2 shows the results of the chosen updated parameters based on the Least squares error of 10 frequencies. The calculated Least squares errors from using ten paired frequencies are larger than four, as explained previously in section 5.3.1.1. The Sensitivity method takes longer to run but gives more accurate predictability of the frequencies in the higher range. The Least squares error of 10 paired frequencies from the Nastran optimisation method is about seven times larger than from the Sensitivity method, but the computation time is also decreased by six times.

Table 5.1 Comparison of results from two updating methods considering only 4 frequencies

Parameters				
Engineering Constant	**Initial Parameters**	**Updated Parameters**		
		Sensitivity Method		**Nastran software**
E (GPa)	190	211.813		202.073
ν	0.2	0.271		0.287506
Iteration Number		5		4
Total Run time (Minutes)		12		2
Frequencies				
Mode Number	**Test Frequencies**	**Frequencies Estimated from Sensitivity Method**	**Relative Error between Test and Estimated Frequencies**	**Frequencies Estimated from Nastran Software**	**Relative Error between Test and Estimated Frequencies**
1	1165.903	1173.3962	6.43E-03	1168.378	2.12E-03
2	1307.999	1307.19895	-6.12E-04	1313.882	4.50E-03
3	1587.405	1578.86356	-5.38E-03	1585.075	-1.47E-03
4	1642.384	1641.83579	-3.34E-04	1653.818	6.96E-03
Least Squares Error using 4 Frequencies		7.07E-05		7.54E-05

Table 5.2 Comparison of results from three updating methods considering 10 frequencies

Parameters					
Engineering Constants	**Initial Parameters**	**Updated Parameters**			
		Sensitivity Method		**Nastran software**	
E (GPa)	190	211.796		202.073	
ν	0.2	0.273		0.287506	
Iteration Number		5		4	
Total Run time (Minutes)		12		2	
Frequencies					
Mode Number	**Test Frequencies**	**Frequencies Estimated from Sensitivity Method**	**Relative Error between Test and Estimated Frequencies**	**Frequencies Estimated from Nastran Software**	**Relative Error between Test and Estimated Frequencies**
1	1165.903	1173.369	6.40E-03	1168.378	2.12E-03
2	1307.999	1306.979	-7.80E-04	1313.882	4.50E-03
3	1587.405	1578.831	-5.40E-03	1585.075	-1.47E-03
4	1642.384	1642.26	-7.55E-05	1653.818	6.96E-03
5	1919.936	1914.78	-2.69E-03	1938.812	9.83E-03
6	1989.356	1988.947	-2.06E-04	1965.283	-1.21E-02
7	2104.627	2112.88	3.92E-03	2106.961	1.11E-03
8	2167.463	2170.975	1.62E-03	2231.129	2.94E-02
9	2388.614	2397.166	3.58E-03	2416.976	1.19E-02
10	2420.473	2399.426	-8.70E-03	2425.304	2.00E-03
Least Squares Error using 10 Frequencies		1.85E-04		1.33E-03	

Hence, the advantage and disadvantages of both methods are observed using this thin rectangular steel plate.

The Sensitivity method:

- Advantages:
    - o The updated parameters calculated give a better prediction of the analytical frequencies of the system.
    - o The updating process allows pairing between test and analytical frequencies and mode shapes.
- Disadvantages:
    - o Larger computational cost
    - o More time-consuming.
    - o When the number of updating parameters increases, the updated parameter could be out of the given range. This disadvantage could either cause longer computation time and cost or be unable to calculate suitable updating parameters with physical meaning.

The Nastran optimisation method:

- Advantages:
    - o Less iteration to approach the final updated parameters.
    - o Less time-consuming and less computational cost.
    - o The method is processed automatically within Nastran software, so the updated parameters are always within the given range.
- Disadvantages:
    - o Less accurate prediction of the analytical frequencies from the updated parameters.
    - o Unable to pair between test and analytical frequencies and mode shapes within the updating process could lead to larger errors or inaccurate updated variables.

5.3.2 Material Identification of Full Brake Pad

5.3.2.1 Parameter Sensitivity

The pad could be treated as an orthotropic material in the general case with nine independent updating parameters in the optimisation method. These nine independent parameters are $C_{11}, C_{12}, C_{13}, C_{22}, C_{23}, C_{33}, C_{44}, C_{55}$ and C_{66} where C_{ij} represents the elastic stiffness tensor in the *i-j* direction. For example, C_{12} is the elastic stiffness tensor in the *x-y* direction. Figure 5.9 shows the FE model of the pad and the local coordinate system of the friction material.
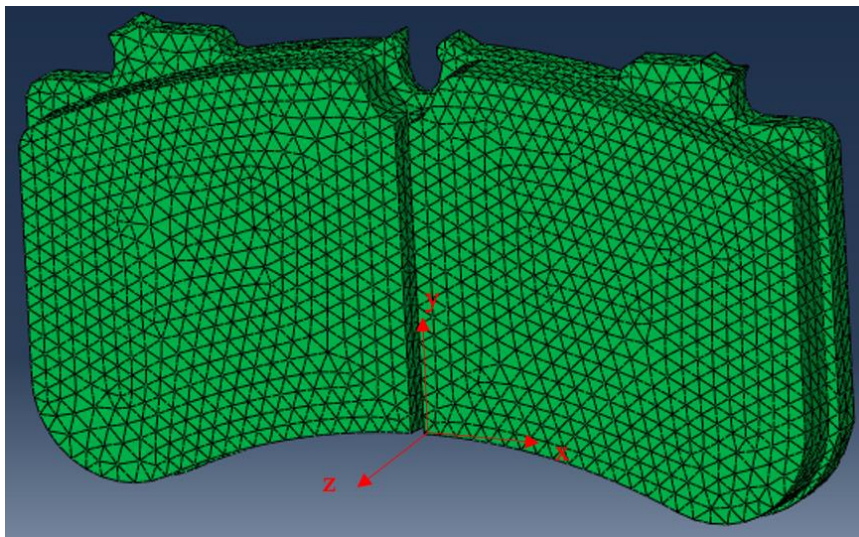
Figure 5.9 The local coordinate system of a brake pad.

Appendix A shows the sensitivity of each parameter to out-of-plane frequencies. Note that the y axis range is the same for all nine graphs. Therefore, the comparison of the sensitivities can be observed clearly between parameters.

The sensitivity analysis of each material property of the brake pad shows that the out-of-plane frequencies of the pad to some material properties of the pad are less sensitive. The insensitivity of these material properties means that it is difficult to identify these parameters using the optimisation method that compares the theoretical and experimental out-of-plane frequencies.

5.3.2.2 Sensitivity Method

As mentioned previously, the pad friction material can be assumed as orthotropic material or transversely isotropic material. The updating procedure could include the experimental results from the compression test in chapter 4 to further reduce the number of independent updating parameters.

The updating parameters are the engineering constants of the pad friction material, including the Young's Modulus, Poisson's ratio, and Shear Modulus in x, y and z-direction, $E_x, E_y, E_z, v_{xy}, v_{xz}, v_{yz}, G_{xy}, G_{xz}, G_{yz}$.

Figure 5.3 shows the pop-up window from the Matlab program of the Sensitivity and Nastran optimisation methods. Note that the selection of the updating material properties in Figure 5.3 is shown in the form of elastic constants such as C_{11}. The convergence from the engineering constants to the elastic constants is only necessary if the Nastran optimisation updating method is used. Further details are previously explained in sections 5.2.1 and 5.2.2.

Since the engineering constants can be directly used in the Sensitivity updating method, the updating material properties are shown in Figure 5.3 state for $C_{11} = E_x, C_{12} = E_y, C_{13} = E_z, C_{22} = v_{xy}, C_{23} = v_{xz}, C_{33} = v_{yz}, C_{44} = G_{xy}, C_{55} = G_{xz}, C_{66} = G_{yz}$. Note that due to the different formats in the ABAQUS and Nastran input files, the order of the material properties in the engineering constants format is important.

The dynamic and static experimental measurements of the pad are shown in chapters 3 and 4, and the analytical dynamic results, such as the frequencies and mode shapes, are determined from the pad FE model using ABAQUS (Figure 5.9).

Appendix B shows the updated parameters and frequencies from using the Sensitivity method. These results are summarised in section 5.3.2.4 and compared with the updated results from using the Nastran optimisation method.

Table B.1 shows the updated material properties in the form of underline engineering constant, the test frequencies, the updated analytical frequencies, and the relative Least between the test and updated analytical frequencies. The pad material type is selected as transversely isotropic material, the mode shapes were not

matched during the optimisation process, and only dynamic test data were used in the updating process.

Table B.2 shows the updated material properties in the form of engineering constant, the test frequencies, the updated analytical frequencies, and the relative Least squares error between the test and updated analytical frequencies. The pad material type is selected as transversely isotropic material, the mode shapes were matched during the optimisation process, and only dynamic test data were used in the updating process.

Table B.3 shows the updated material properties in the form of engineering constant, the test frequencies, the updated analytical frequencies, and the relative Least squares error between the test and updated analytical frequencies. The pad material type is selected as orthotropic material, the mode shapes were matched during the optimisation process, and only dynamic test data were used in the updating process.

Table B.4 shows the updated material properties in the form of engineering constant, the test frequencies, the updated analytical frequencies, and the relative Least squares error between the test and updated analytical frequencies. The pad material type is selected as transversely isotropic material, the mode shapes were matched during the optimisation process, and both dynamic and static test data were used in the updating process.

The compression (static) test data of the relationship between the stress in the x-direction and the strain in the x, y, and z-directions for the pad friction material was shown in Figure 4.21. The linear stress-strain relationships are used with equations 5.16 to 5.20 to apply extra constraints to the parameters and reduce the number of independent updating parameters in the identification process.

The procedures that convert the constraint equations 5.16-5.20 from elastic to engineering constants are shown below.

Known equalities when assuming pad friction material is transversely isotropic:

$E_x = E_y, \ v_{xy} = v_{yx}, \ v_{xz} = v_{yz}, \ v_{zx} = v_{zy}, \ G_{xz} = G_{yz}, \ v_{zx} = \frac{E_z}{E_x} v_{xz}$

From the above equalities, the convergence from elastic constants to engineering constants are:

$$E_x = E_y = \frac{C_{33}(C_{11}^2 - C_{12}^2) - 2C_{13}^2(C_{11} - C_{12})}{C_{11}C_{33} - C_{13}^2} \tag{5.34}$$

$$E_z = C_{33} - \frac{2C_{13}^2}{C_{11} + C_{12}} \tag{5.35}$$

$$\nu_{xy} = \nu_{yx} = \frac{C_{33}C_{12} - C_{13}^2}{C_{11}C_{33} - C_{13}^2} \tag{5.36}$$

$$\nu_{xz} = \nu_{yz} = \frac{C_{13}(C_{11} - C_{12})}{C_{11}C_{13} - C_{13}^2} \tag{5.37}$$

$$\nu_{zx} = \nu_{zy} = \frac{C_{13}}{C_{11} + C_{12}} \tag{5.38}$$

Combining equations 5.16 to 5.20 with equations 5.34 to 5.38, the constraint equations applying to the pad friction material in terms of engineering constants using the transversely isotropic material constraints and the stress-strain relationship are:

$$E_x = \frac{E_z \nu_{xz}(\nu_{xz}\varepsilon_{11} - \nu_{xz}\varepsilon_{22} + \nu_{xz}\varepsilon_{33} + \varepsilon_{33})}{\sqrt{1 + \dfrac{\nu_{xz}(1 + \nu_{xz})(\varepsilon_{11} + \varepsilon_{22})}{\varepsilon_{33}}\varepsilon_{11} - \varepsilon_{22}}} \tag{5.39}$$

$$E_y = \frac{E_z \nu_{xz}(\nu_{xz}\varepsilon_{11} - \nu_{xz}\varepsilon_{22} + \nu_{xz}\varepsilon_{33} + \varepsilon_{33})}{\sqrt{1 + \dfrac{\nu_{xz}(1 + \nu_{xz})(\varepsilon_{11} + \varepsilon_{22})}{\varepsilon_{33}}\varepsilon_{11} - \varepsilon_{22}}} \tag{5.40}$$

$$\nu_{xy} = \sqrt{1 + \frac{\nu_{xz}(1 + \nu_{xz})(\varepsilon_{11} + \varepsilon_{22})}{\varepsilon_{33}}} \tag{5.41}$$

$$\nu_{yz} = \nu_{xz} \tag{5.42}$$

$$G_{yz} = G_{xz} \tag{5.43}$$

5.3.2.3 Nastran Optimisation Method

The dynamic and static experimental measurements of the pad are in chapters 3 and 4, as mentioned in section 5.3.2.2. The analytical dynamic results of the pad are determined from the FE model using Nastran (Figure 5.9).

The convergence from the engineering constants to the elastic constants is necessary as the Nastran optimisation updating method is used. Further details are previously explained in sections 5.2.1 and 5.2.2. The convergence from the engineering constants to the elastic constants is explained in section 4.1.1.

Appendix C shows the updated parameters and frequencies using the Nastran optimisation method. These results are summarised in section 5.3.2.4 and compared with the updated results from using the Sensitivity method.

Table C.1 shows the updated material properties in the form of <u>elastic constant</u>, the test frequencies, the updated analytical frequencies, and the relative Least between the test and updated analytical frequencies. The pad material type is selected as <u>transversely isotropic material</u>, the <u>mode shapes were not matched</u> during the optimisation process, and <u>only dynamic test data</u> were used in the updating process.

Table C.2 shows the updated material properties in the form of <u>elastic constant</u>, the test frequencies, the updated analytical frequencies, and the relative Least squares error between the test and updated analytical frequencies. The pad material type is selected as <u>transversely isotropic material</u>, the <u>mode shapes were matched</u> during the optimisation process, and <u>only dynamic test data</u> were used in the updating process.

Table C.3 shows the updated material properties in the form of <u>elastic constant</u>, the test frequencies, the updated analytical frequencies, and the relative Least squares error between the test and updated analytical frequencies. The pad material type is selected as <u>orthotropic material</u>, the <u>mode shapes were matched</u> during the optimisation process, and <u>only dynamic test data</u> were used in the updating process.

Table C.4 shows the updated material properties in the form of <u>elastic constant</u>, the test frequencies, the updated analytical frequencies, and the relative Least squares error between the test and updated analytical frequencies. The pad material type is selected as <u>transversely isotropic material</u>, the <u>mode shapes were matched</u> during the optimisation process, and <u>both dynamic and static test data</u> were used in the updating process. The compression (static) test data were used to apply extra constraints to the parameters, explained in detail in section 5.3.2.2 above.

5.3.2.4 Results and Discussion

Appendix B and C shows the updated material properties and analytical frequencies using different updating criteria.

The results from table B.1, B.2, B.3, and B.4 shows that:

- Comparing Table B.1 and B.2: If the test and analytical frequencies are not paired in the updating process, the Least squares error between the two sets of frequencies are larger than the paired frequencies. This increase in relative error is largely due to mode 13, and a few reasons could cause this; i) the accuracy of the test frequencies and mode shapes decreases in the high frequency range; ii) the analytical frequency and mode shape in mode 13 could be the in-plane mode, which does not match with the out-of-plane test frequency and mode shape.

- Comparing Table B.2 and B.3: If pad material is considered as orthotropic material, the error between the paired updated test and analytical frequencies is smaller. Therefore, if the reliable test frequencies and mode shapes are enough (more than 9), it is better to consider the pad friction material as an orthotropic material.

- Comparing Table B.2 and B.4: If the pad friction material is considered transversely isotropic material, then the error from the updated results with additional stress-strain constraints is smaller than the error from the updated results using dynamic test data only. The number of independent updating parameters is reduced with the additional stress-strain constraints.

The conclusion is drawn from the results in table C.1, C.2, C.3, and C.4 are similar to table B.1, B.2, B.3, and B.4. From the comparison between the error calculated from tables in Appendix B and Appendix C, it is also noticeable that the updated analytical frequencies determined from the Sensitivity method are better than from the Nastran optimisation method. This observation matches with the discussion in section 5.3.1.3.

5.4 Summary

The fundamental theories of the model updating methods, such as the Sensitivity method and the Nastran Optimisation method, were studied. The developed Matlab program was discussed with the step-to-step explanation of the used model updating method in the code.

The isotropic material properties of a thin rectangular steel plate were determined in which the experimental frequencies and mode shapes were compared with the analytical data from the FE model. This is to validate the model updating methods.

The material properties of the friction material of the brake pad were identified using the given FE model and the experimental data. The pad friction material was considered as orthotropic material or transversely isotropic material. The model updating results from two material identification methods were shown and discussed in section 5.3.2.4, and the Least square error between the paired test frequencies and FE analysed frequencies were compared.

Chapter 6 Hyperelastic Materials

This chapter presents the fundamental theories of different types of Hyperelastic materials, including the isotropic and anisotropic Hyperelastic materials. The equations and theories are mainly adapted from (ABAQUS, 2014) and (Hackett, 2018).

Firstly, the concept of the hyperelastic material is presented, and the formulas of different strain energy potential functions are used in ABAQUS.

Then, the measured stress-strain data of the brake pad friction material from the compressibility tests are used in ABAQUS to apply the pad friction material as a Hyperelastic material.

6.1 Introduction

The concept of elasticity must be understood before understanding the concept of hyperelasticity. A fundamental property of elastic materials is that the stress depends only on the current level of the strain. The perfect elasticity exists in theory where the material is reversible, path independent and not accompanied by any energy dissipation during the loading and unloading process.

If the loading and unloading stress-strain curves are identical and the original shape of the material is recovered upon unloading, then the strains are said to be reversible. If the stress state in a material is independent of the history of the material point, the behaviour of the material is said to be path independent. In a purely mechanical theory, reversibility and path independence also imply the absence of energy dissipation in the process of deformation(Hackett, 2018).

The concept of finite strain elasticity is that finite elasticity is a theory of elastic materials capable of undergoing large deformations (Hackett, 2018). The finite strain theory (also called large strain theory or large deformation theory) deals with deformations in which strains and/or rotations are large enough to invalidate assumptions inherent in infinitesimal strain theory.

Many different constitutive relationships have been developed for multiaxial elasticity in the finite strain elasticity. The widely accepted finite strain elasticity formulations can be classified into three formats—algebraic, integral, and differential (Hackett, 2018).

- Algebraic format – Cauchy Elasticity:

$$\boldsymbol{\sigma} = \mathbf{f}(\boldsymbol{\varepsilon})$$

Cauchy elasticity is limited to rate-independent and history-independent material behaviour. In Cauchy elasticity, the stress is path independent, but the energy is not. Cauchy elasticity has a non-conservative structure, i.e., the stress is not derivable from a scalar potential function (Hackett, 2018).

- Integral – Green elasticity (or hyperelasticity):

$$\boldsymbol{\sigma} = \frac{\partial W}{\partial \boldsymbol{\varepsilon}}$$

129

For hyperelasticity, the response is fully path independent and reversible, and the stress is derived from a strain (or stored) energy potential (Hackett, 2018).

- Differential – Hypoelasticity:

$$\partial \boldsymbol{\sigma} = E_t : \partial \boldsymbol{\varepsilon} \quad \text{or} \quad \dot{\boldsymbol{\sigma}} = g(\boldsymbol{\sigma}, \mathbf{d})$$

where $\mathbf{d}$ = rate-of-deformation tensor.

Hypoelasticity is used to model materials that exhibit nonlinear but reversible stress-strain behaviour even at small strains. Hypoelasticity is defined by equations based upon objective time rate tensors, which, unlike hyperelasticity, require incrementally objective solution formulations (Hackett, 2018).

Therefore, generally speaking, hyperelastic material models are most suitable for the modelling problems within the widest range of finite strain elasticity.

The strain energy function is introduced into the concept of elasticity by George Green, and elastic materials with such a function are said to be Green elastic or hyperelastic. Drozdov gave a formal definition of hyperelasticity in 1996 as the constitutive theory that describes the mechanical behaviour of elastic solids with the use of (only) one material function is called hyperelasticity. The spectrum of materials, the behaviour of which can be classified as being hyperelastic, includes vulcanised rubber, solid propellant, polymeric foams, and soft biological materials (Hackett, 2018).

It is well known that pad materials are anisotropic, inhomogeneous, moderately nonlinear, and thus very complicated. In industries, the pad materials of friction brakes in FE models are treated as elastic materials. Industries recognise that the nonlinearity of these complex composite materials should be explored in the analysis of these materials. One idea is to treat the pad friction material as a hyperelastic material and include that strain energy function into the material analysis.

6.1.1 Strain Energy Functions

Hyperelastic materials can also be classified as isotropic and non-isotropic. The most known isotropic hyperelastic model is probably the Mooney-Rivlin model and its reduced case Neo-Hookean model, which are used to describe the deformation of rubber.

The isotropic hyperelastic model could be described as

$$U = f\,(\bar{I}_1, \bar{I}_2, \bar{I}_3) \tag{6.1}$$

Where U is the strain energy density and $I_1, I_2,$ and I_3 are the three invariants of the Cauchy-Green deformation tensors given as:

$$\bar{I}_1 = \theta_1^2 + \theta_2^2 + \theta_3^2 \tag{6.2}$$

$$\bar{I}_2 = \theta_1^2\theta_2^2 + \theta_2^2\theta_3^2 + \theta_3^2\theta_1^2 \tag{6.3}$$

$$\bar{I}_3 = \theta_1^2\theta_2^2\theta_3^2 \tag{6.4}$$

in which θ_i are the principal extension ratios.

In 1951, Rivlin specified the power series from equation 6.1 which is also considered as the polynomial hyperelastic model.

$$U = \sum_{i+j+k=1}^{\infty} C_{ijk}(I_1 - 3)^i(I_2 - 3)^j(I_3 - 1)^k \tag{6.5}$$

However, if the material is considered to be incompressible, then $\bar{I}_3 = 1$ and equation 6.5 becomes

$$U = \sum_{i+j=1}^{\infty} C_{ij}(I_1 - 3)^i(I_2 - 3)^j \tag{6.6}$$

The Mooney-Rivlin model is a special case of equation 6.6 where only the first two terms of equation 6.6.

$$U = C_{10}(I_1 - 3) + C_{01}(I_2 - 3) \tag{6.7}$$

And Neo-Hookean considers only the first term of equation 6.7

$$U = C_{10}(I_1 - 3) \tag{6.8}$$

If the material is considered to be almost incompressible rather than completely incompressible, a hydrostatic term could be added to equation 6.7:

$$U = C_{10}(I_1 - 3) + C_{01}(I_2 - 3) + U_H(I_3) \qquad (6.9)$$

To uncouple the volumetric response and the deviatoric response in equation 6.9, the reduced invariants are considered:

$$\bar{I}_1 = I_1 I_3^{-1/3} \qquad (6.10)$$

$$\bar{I}_2 = I_2 I_3^{-2/3} \qquad (6.11)$$

$$J_{el} = \sqrt{I_3} \qquad (6.12)$$

And

$$U_H = D_1(J_{el} - 1)^2 \qquad (6.13)$$

Hence, equation 6.9 can be rewritten as:

$$U = C_{10}(\bar{I}_1 - 3) + C_{01}(\bar{I}_2 - 3) + D_1(J_{el} - 1)^2 \qquad (6.14)$$

Apart from the Mooney-Rivlin and Neo-Hookean models, many other hyperelastic models depend on the strain energy functions. Table 6.1 shows the strain energy functions that are popular and being used in ABAQUS.

One model that is also well know but not included in ABAQUS is the Gent model (Gent, 1996) where

$$U = -G \frac{J_m}{2} \ln\left(1 - \frac{I_1 - 3}{J_m}\right) \qquad (6.15)$$

Where G is the shear modulus, and the value of J_m corresponds to the maximum extension ratio θ_m and represents the limit state of the rubber-like material (Gent, 1996).

Table 6.1 Strain energy potential functions (ABAQUS, 2014)

Energy Function	Function Form
Isotropic Hyperelastic Material	
Arruda-Boyce Form	$U = \mu\left(\frac{1}{2}(\bar{I}_1 - 3) + \frac{1}{20\theta_m^2}(\bar{I}_1^2 - 9) + \frac{11}{1050\theta_m^4}(\bar{I}_1^3 - 27)\right.$ $\left. + \frac{19}{7000\theta_m^6}(\bar{I}_1^4 - 81) + \frac{519}{673750\theta_m^8}(\bar{I}_1^5 - 243)\right)$ $+ \frac{1}{D}\left(\frac{J_{el}^2 - 1}{2} - \ln J_{el}\right)$ where U = strain energy per unit of reference volume, μ, θ_m, D = temperature dependent material parameters
Marlow	$U = U_{dev}(\bar{I}_1) + U_{vol}(J_{el})$ where U_{dev} = the deviatoric part of strain energy U_{vol} = the volumetric part of strain energy
Mooney-Rivlin	$U = C_{10}(\bar{I}_1 - 3) + C_{01}(\bar{I}_2 - 3) + D_1(J_{el} - 1)^2$ where C_{10}, C_{01}, D_1 = temperature dependent material parameters
Neo Hookean	$U = C_{10}(\bar{I}_1 - 3) + \frac{1}{D_1}(J_{el} - 1)^2$
Ogden	$U = \sum_{i=1}^{N}\frac{2\mu_i}{\alpha_i^2}(\bar{\theta}_1^{\alpha_i} + \bar{\theta}_2^{\alpha_i} + \bar{\theta}_3^{\alpha_i} - 3) + \sum_{i=1}^{N}\frac{1}{D_i}(J_{el} - 1)^{2i}$

	where N is a material parameter $\mu_i\,,\alpha_i\,,D_i$ = temperature dependent material parameters The particular material models described above—the Mooney-Rivlin and neo-Hookean forms—can also be obtained from the general Ogden strain energy potential for special choices of μ_i and α_i.
Polynomial	$$U = \sum_{i+j+k=1}^{N} C_{ijk}(\bar{I}_1 - 3)^i(\bar{I}_2 - 3)^j(\bar{I}_3 - 1)^k$$ $$+ \sum_{i=1}^{N} \frac{1}{D_i}(J_{el} - 1)^{2i}$$ where C_{ij} = temperature dependent material parameters For cases where the nominal strains are small or only moderately large ($<$ 100%), the first terms in the polynomial series usually provide a sufficiently accurate model. Some particular material models—the Mooney-Rivlin, neo-Hookean, and Yeoh forms—are obtained for special choices of C_{ij}.
Reduced Polynomial	$$U = \sum_{i=1}^{N} C_{i0}(\bar{I}_1 - 3)^i + \sum_{i=1}^{N} \frac{1}{D_i}(J_{el} - 1)^{2i}$$
Van der Waals	$$U = \mu\left(-(\theta_m^2 - 3)(\ln(1 - \eta) + \eta) - \frac{2}{3}a\left(\frac{\tilde{I} - 3}{2}\right)^{\frac{3}{2}}\right)$$ $$+ \frac{1}{D}\left(\frac{J_{el}^2 - 1}{2} - \ln J_{el}\right)$$

	where $\tilde{I} = (1 - \beta)\bar{I}_1 + \beta\bar{I}_2$ $$\eta = \sqrt{\frac{\tilde{I} - 3}{\theta_m^2 - 3}}$$ a is the global interaction parameter β is an invariant mixture parameter D governs the compressibility
Yeoh	$$U = C_{10}(\bar{I}_1 - 3) + C_{20}(\bar{I}_1 - 3)^2 + C_{30}(\bar{I}_1 - 3)^3$$ $$+ \frac{1}{D_1}(J_{el} - 1)^2 + \frac{1}{D_2}(J_{el} - 1)^4$$ $$+ \frac{1}{D_3}(J_{el} - 1)^6$$ where $C_{10}, C_{20}, C_{30}, D_1, D_2, D_3 =$ temperature dependent material parameters

Anisotropic Hyperelastic Material

Generalised Fung (Fung-Anisotropic/ Fung-Orthotropic)	$$U = \frac{c}{2}(\exp(Q) - 1) + \frac{1}{D}\left(\frac{J_{el}^2 - 1}{2} - \ln J_{el}\right)$$ where $c, D =$ temperature dependent material parameters $$Q = \bar{\boldsymbol{\varepsilon}}^G : \mathbf{b} : \bar{\boldsymbol{\varepsilon}}^G = \bar{\varepsilon}_{ij}^G \, b_{ijkl} \bar{\varepsilon}_{kl}^G$$ b_{ijkl} $=$ dimensionless symmetric fourth $-$ order tensor of anisotropic material constants $\bar{\varepsilon}_{ij}^G =$ the components of the modified Green strain tensor

Holzapfel- Gasser-Ogden	$U = C_{10}(\bar{I}_1 - 3) + \dfrac{1}{D}\left(\dfrac{J_{el}^2 - 1}{2} - \ln J_{el}\right)$ $\qquad + \dfrac{k_1}{2k_2}\displaystyle\sum_{\alpha=1}^{N}(\exp(k_2\langle \bar{E}_\alpha\rangle^2) - 1)$ where $\bar{E}_\alpha \overset{\text{def}}{=} \kappa(\bar{I}_1 - 3) + (1 - 3\kappa)(\bar{I}_{4(\alpha\alpha)} - 1)$ $\quad C_{10}, D, k_1, k_2, \kappa$ $\quad = $ temperature dependent material parameters $N = $ the number of families of fibers $(N \leq 3)$ $\bar{I}_{4(\alpha\alpha)} = $ pseudo invariants of $\bar{\mathbf{C}}$ and $\mathbf{A}_\alpha$ The strain-like quantity $\bar{E}_\alpha$ characterizes the deformation of the family of fibres with mean direction $\mathbf{A}_\alpha$.

6.2 FE Model of Compression Test Sample in ABAQUS

The compression tests of the brake pad friction material are done in chapter 4 using both the strain gauges and the DIC to measure the lateral change in strain. The measured compression test data using the DIC is used in this chapter to analyse the pad friction material as isotropic Hyperelastic material.

ABAQUS is a well-known FE analysing software that could simulate the compression test results of the pad specimens. The compression rate test results were used as the material properties of the sample block of the pad friction material in ABAQUS at the beginning. The FE model of the sample block is shown in Figures 6.1 and 6.2, where the size of the block is 50mm×40mm in cross-section area and 11.45mm thick for the friction material. The element type of the block sample was C3D20H, which are 20-node hybrid quadratic bricks.

The collected compression test data from the DIC test can analyse the isotropic hyperelastic material in ABAQUS. The analysed compression test data shown in

Figure 4.21, section 4.3.2 provided the nonlinear relationship between the stress in the x-direction and the strain in the x-direction, measured using the Instron machine. The equation of the best fit line (in blue) estimates the stress changes with the strain variation.

$$y = (-1.01 * 10^{10}) * x^3 + (1.27 * 10^7) * x^2 + (4.66 * 10^3) * x \qquad (6.16)$$

where y = stress applied in the x-direction, x = change in strain in the x-direction. The range of x is set to be 0>x>6E-04, the number of x values is set to be 100, so the incresing increment of x at each step is 6E-06.
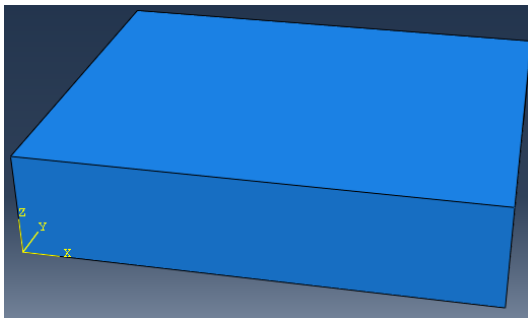
Figure 6.1 Brake Pad Sample Block for Compression Rate Test
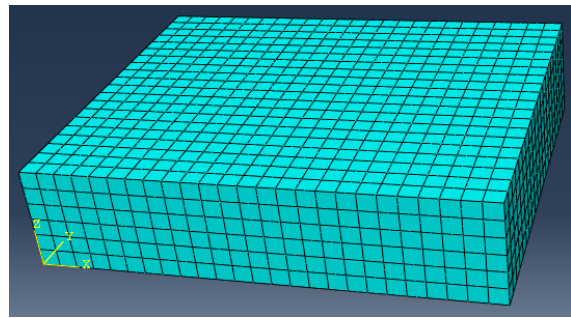
Figure 6.2 Meshed Brake Pad Sample Block for Compression Rate Test

6.3 Evaluate Compression Test Data in ABAQUS

As mentioned previously, the compression rate test data of the pad sample block was used in the isotropic hyperelastic material card. The evaluation of all types of strain energy potential is shown in Figure 6.3 below.

Figure 6.3 shows the trend of analytical stress-strain relationships calculated from all strain energy potential types against the compression test data. The bottom right corner in Figure 6.3 shows the label of each line. Note that the red cross-line in Figure 6.3 represents the test data.

6.3.1 Evaluation of Isotropic Hyperelastic Models by Observation

There are two methods to evaluate the most suitable isotropic hyperelastic model from ABAQUS with the given compression test data. One method is to observe from Figure 6.3 and find the line that best matches the test data. The advantage of this method is that it is easier to operate, and the evaluation time would be small. The disadvantages are: firstly, the method is not very accurate because the conclusion is made by observation, and there could be a considerable human error in the conclusion; secondly, some of the lines could be very close to each other, and it would be very difficult to tell which is the best fitting line.

Figures 6.4 and 6.5 show the evaluation of the suitable isotropic hyperelastic model from the observation method. In Figure 6.4, the number of suitable isotropic hyperelastic models is reduced to three, and the three selected curves overlay each other. Since the three selected isotropic hyperelastic models in Figure 6.4 are Ogden models with different strain energy potential orders, the Ogden model with strain energy potential order N = 3 is selected as the most suitable isotropic hyperelastic model (Figure 6.5).

Figure 6.6 shows the coefficients of the Ogden N3 model calculated from ABAQUS. The isotropic hyperelastic models in ABAQUS can be defined from both the static test data and the defined strain energy potential coefficients.

6.3.2 Evaluation of Isotropic Hyperelastic Models by Calculation

Another method to evaluate the most suitable isotropic hyperelastic model would be comparing the relative error between the test and analytical data for all strain energy potential types and finding the method that gives minimum average or least-squares error between the test and analytical data.

However, some evaluation can be done using observation to reduce the isotropic hyperelastic models, which are unsuitable, for example, the model Ogden N1 in Figure 6.3.
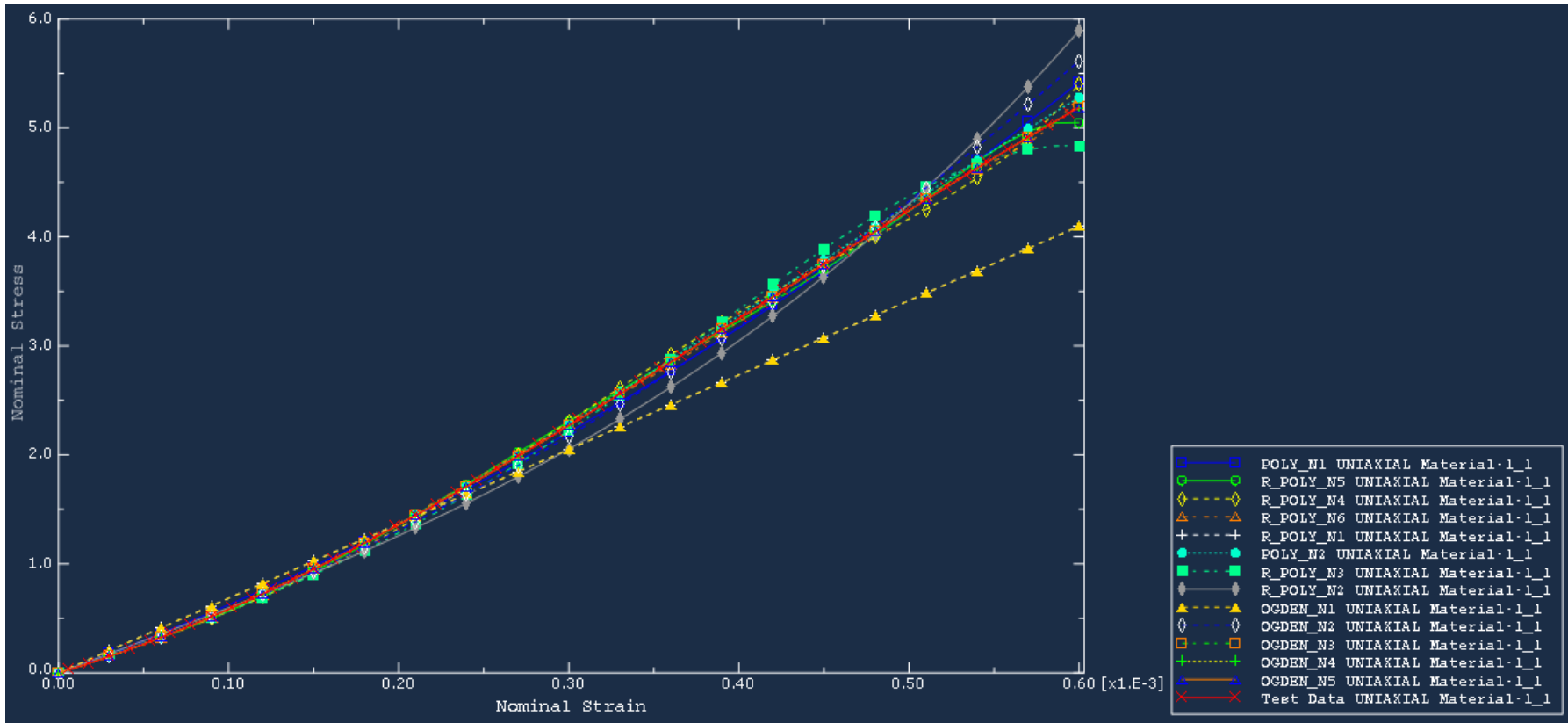
Figure 6.3 Evaluate Compression Test Sample With All Isotropic Hyperelastic Material Models in ABAQUS
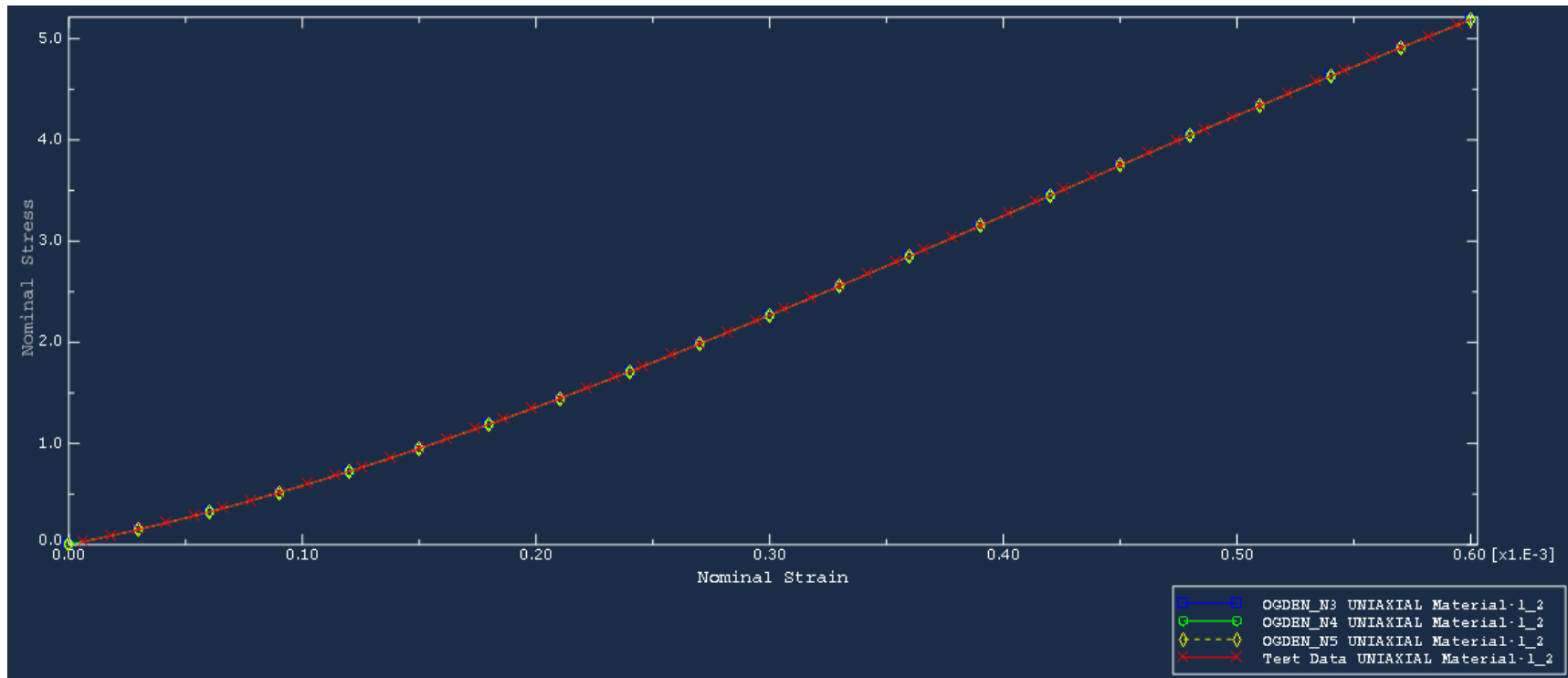
Figure 6.4 Evaluate Compression Test Sample With Selected Isotropic Hyperelastic Material Models in ABAQUS
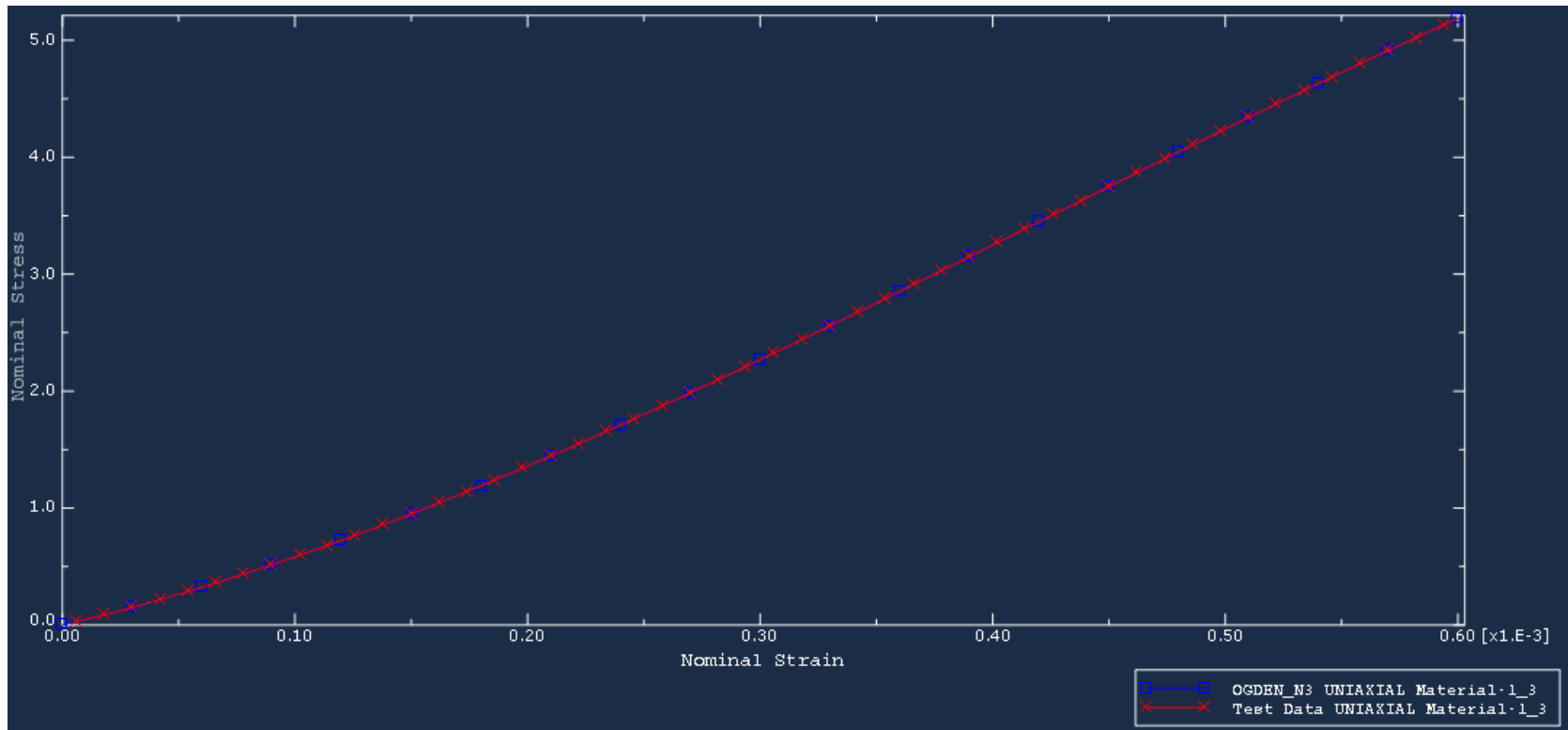
Figure 6.5 Suitable Isotropic Hyperelastic Material Model Against Compression Test Data in ABAQUS, Ogden_N3

141

```
Material Parameters and Stability Limit Information                    —    □    ✕

Material:    Material-1
Job Name:  Material-1_3

┌ Ogden, N = 3 ┐
│              │   HYPERELASTICITY - OGDEN STRAIN ENERGY FUNCTION WITH N =   3
│              │
│              │              I          MU_I          ALPHA_I           D_I
│              │
│              │              1      3.380179682E+09    1.89160869      0.00000000
│              │              2     -2.250623276E+09    3.88752572      0.00000000
│              │              3     -1.129554853E+09   -2.10022974      0.00000000
│              │
│              │
│              │                       STABILITY LIMIT INFORMATION
│              │
│              │
│              │   WARNING: UNSTABLE HYPERELASTIC MATERIAL
│              │
│              │
│              │      UNIAXIAL TENSION:        UNSTABLE AT A NOMINAL STRAIN LARGER THAN      0.0100
│              │      UNIAXIAL COMPRESSION:    UNSTABLE AT A NOMINAL STRAIN LESS THAN       -0.0197
│              │      BIAXIAL TENSION:         UNSTABLE AT A NOMINAL STRAIN LARGER THAN      0.0100
│              │      BIAXIAL COMPRESSION:     UNSTABLE AT A NOMINAL STRAIN LESS THAN       -0.0050
│              │      PLANAR TENSION:          UNSTABLE AT A NOMINAL STRAIN LARGER THAN      0.0100
│              │      PLANAR COMPRESSION:      UNSTABLE AT A NOMINAL STRAIN LESS THAN       -0.0099
│              │      VOLUMETRIC TENSION:      STABLE FOR ALL VOLUME RATIOS
│              │      VOLUMETRIC COMPRESSION:  STABLE FOR ALL VOLUME RATIOS

                              [ Dismiss ]
```

Figure 6.6 Coefficients of Ogden_N3 Determined In ABAQUS

142

Table 6.2 shows the evaluation of the isotropic hyperelastic models using the observation method first and the calculation method afterwards (Figure 6.4).

Table 6.2 Compare the Average and Least-Squares Error Using Different Strain Energy Potential Method

	Average Relative error	Least Squares Error
Ogden_N3	0.086%	0.671%
Ogden_N4	0.087%	0.678%
Ogden_N5	0.087%	0.674%

6.4 Applying Suitable Isotropic Hyperelastic Material Properties to the Full Pad

The Ogden N3 model is selected as the suitable isotropic hyperelastic model for the pad friction material (section 6.3). The FE model of the full pad is shown in Figure 5.9. The Ogden N3 isotropic hyperelastic model can be defined from either the static test data, the stress and strain input values or the calculated strain energy potential coefficients.

The element type for the pad FE model is C3D10H, where H stand for Hybrid formulation. Note that the simulation of the pad frequencies using the isotropic hyperelastic material card is only successful if the meshing of the FE model is set to be hybrid.

Table 6.3 shows the comparison between the test frequencies and the analytical frequencies with the elastic FE model and the hyperelastic FE model of the pad friction material. Note that the analytical frequencies using the elastic material card is determined in section 5.3.2 and shown in table B.3 in Appendix B.

From table 6.3, it can be observed that the error between the dynamic test data and the analytical frequencies calculated using the Ogden N3 material card are a lot larger than using the conventional transversely isotropic material card. Hence, using the transversely isotropic material card in the pad FE model is more suitable. Further investigation is needed to find more suitable isotropic hyperelastic material properties for the FE model of the pad friction material.

Table 6.3 Comparison of Dynamic Test Frequencies with Analytical Frequencies Using Transversely Isotropic Elastic Material and Using Isotropic Hyperelastic Material

Mode Number	Test Frequencies (Hz)	Mode Number	Elastic Simulation (Hz)	Relative Difference	Mode Number	Hyperelastic Simulation (Hz)	Relative Difference
1	1507	1	1551	2.91%	4	1421	5.71%
2	2020	2	2015	0.24%	5	1759	12.90%
3	4556	3	4552	0.09%	6	3948	13.34%
4	4803	4	4831	0.58%	7	4093	14.77%
5	6970	5	6900	1.00%	8	5963	14.44%
6	7113	6	7172	0.82%	9	6299	11.45%
8	8429	8	8387	0.51%	10	7329	13.06%
9	8775	9	8778	0.03%	12	7985	9.01%
19	10788	19	10739	0.45%	13	9458	12.33%
11	11332	11	11426	0.83%	14	10006	11.70%
12	12140	12	12152	0.10%	15	10974	9.60%
Average relative error				0.69%			11.66%

6.5 Summary

The fundamental theories of different types of Hyperelastic materials, including the isotropic and anisotropic Hyperelastic materials, were reviewed in section 6.1. The concept of hyperelastic material was presented, and the formulas of different strain energy potential functions were used in ABAQUS.

The evaluation analysis was done by applying the compression test data with different types of isotropic hyperelastic materials cards to the FE model of the pad specimen in ABAQUS.

The selected suitable isotropic hyperelastic materials were applied to the full brake pad FE model, and the analytical frequencies were simulated and compared with the results from the material identification method previously shown in table B.3.

Chapter 7 Damping Identification of Pad Material

This chapter covers the formulations and fundamental theories of the damped vibration theory and the Rayleigh damping model. Rayleigh damping coefficients are used in the pad FE model and the sensitivity of the constants α and β are presented in table 7.2.

The identification method such as the Sensitivity method is used to determine the Rayleigh damping coefficients. Data of the damping factors of the friction material collected from the dynamic experiments are used in this chapter.

The analytical complex eigenvalues and damping factors from the pad FE model is compared against the test complex eigenvalues and damping coefficient. The trend of the updated analytical damping coefficients using Rayleigh damping coefficients are plot against the trend of the test damping coefficients in Figure 7.1 and table 7.3.

7.1 Introduction

This Chapter reviews some damping models which can be used to determine the damping factor of the pad friction material theoretically.

Chapter 5 reviewed the equation of motion of an undamped vibration system. Often in vibration analysis, it is useful to model energy dissipation, or damping, by including the term $\mathbf{C}$, where $\mathbf{C}$ is an n x n matrix of damping coefficients and $\dot{\mathbf{x}}$ is an n x 1 vector of velocities.

The general equation of motion of a Multi-Degree-of-Freedom (MDoF) system is defined as

$$\mathbf{M}\ddot{x}(t) + \mathbf{C}\dot{x}(t) + \mathbf{K}x(t) = \mathbf{f}(t) \tag{7.1}$$

where $\mathbf{f}(t)$ is the force vector in function of time.

Assuming the solution of the system is in the form of $\mathbf{x}(t) = \boldsymbol{\varphi}e^{\lambda t}$, equation 7.1 can be rewritten into equation 7.2 below.

$$(\lambda^2\mathbf{M} + \lambda\mathbf{C} + \mathbf{K})\boldsymbol{\varphi} = 0 \tag{7.2}$$

where λ is the eigenvalue of the system, which can be calculated from $\det(\lambda^2\mathbf{M} + \lambda\mathbf{C} + \mathbf{K}) = 0$. The mode shape vector corresponding to each eigenvalue of the system would be $\boldsymbol{\phi}$ and $\boldsymbol{\Phi}$ is the modal matrix with each column being a mode vector of the system.

From the general EoM of the system, an EoM with modal vector coordinates, q rather that physical vector coordinates, x was derived as shown in equatiob 7.3.

$$\boldsymbol{\phi}^{\mathrm{T}}\mathbf{M}\boldsymbol{\phi}\ddot{q} + \boldsymbol{\phi}^{\mathrm{T}}\mathbf{C}\boldsymbol{\phi}\dot{q} + \boldsymbol{\phi}^{\mathrm{T}}\mathbf{K}\boldsymbol{\phi}q = \boldsymbol{\phi}^{\mathrm{T}}\mathbf{f} \tag{7.3}$$

Where $\mathbf{x} = \sum_{j=1}^{n} \boldsymbol{\varphi}_j q_j = \boldsymbol{\phi}\mathbf{q}.$

This chapter studies two methods which determine and implement the damping coefficient of the pad, the Lancaster method and the Rayleigh damping coefficient.

7.2 Rayleigh Damping Coefficients

7.2.1 Introduction

The orthogonality of normal modes is not applicable for damped system with EOM shown in equation 7.3. However, if the damping is assumed to be proportional damping, then the orthogonality of the normal modes can be applied to the damping matrix, $\mathbf{C}$. For an MDoF system with proportional damping, the complicated EoM can be simplified and converted into a set of SDoF systems in modal coordinates.

The proportional damping is also know as Rayleigh damping, which was introduced by Lord Rayleigh in 1878. Proportional damping means that $\mathbf{C}$ is simultaneously diagonalisable with $\mathbf{M}$ and $\mathbf{K}$. In terms of Rayleigh damping model, $\mathbf{C}$ is a function of $\mathbf{M}$ and $\mathbf{K}$.

$$\mathbf{C} = \alpha\mathbf{M} + \beta\mathbf{K} \tag{7.4}$$

where α and β are mass and stiffness proportional Rayleigh damping coefficients. Equations 7.3 and 7.4 gives:

$$\boldsymbol{\phi}^{\mathrm{T}}\mathbf{M}\boldsymbol{\phi}\ddot{\mathbf{q}} + \boldsymbol{\phi}^{\mathrm{T}}(\alpha\mathbf{M} + \beta\mathbf{K})\boldsymbol{\phi}\dot{\mathbf{q}} + \boldsymbol{\phi}^{\mathrm{T}}\mathbf{K}\boldsymbol{\phi}\mathbf{q} = \mathbf{0} \tag{7.5}$$

Applying orthogonality of normal modes and mass-normalisation to equation gives:

$$\ddot{\mathbf{q}} + \begin{bmatrix} \ddots & 0 & 0 \\ 0 & \alpha\omega_j^2 + \beta & 0 \\ 0 & 0 & \ddots \end{bmatrix}\dot{\mathbf{q}} + \begin{bmatrix} \ddots & 0 & 0 \\ 0 & \omega_j^2 & 0 \\ 0 & 0 & \ddots \end{bmatrix}\mathbf{q} = \mathbf{0} \tag{7.6}$$

which leads to n uncoupled SDOF mass-normalised equations:

$$\ddot{q}_j(t) + (\alpha\omega_j^2 + \beta)\dot{q}_j(t) + \omega_j^2 q_j(t) = 0 \tag{7.7}$$

$$\ddot{q}_j(t) + 2\zeta_j\omega_{n_j}\dot{q}_j(t) + \omega_{n_j}^2 q_j(t) = 0 \tag{7.8}$$

Hence, the damping matrix can be reduced to

$$2\zeta_j\omega_{n_j} = \alpha + \beta\omega_{n_j}^2 \tag{7.9}$$

$$\zeta_j = \frac{\alpha}{2\omega_{n_j}} + \frac{\beta\omega_{n_j}}{2} \tag{7.10}$$

where ω_j is the j-th eigenvalue of the system and ζ_j is the damping ratio of the j-th eigenvalue. Equation 7.9 is rearranged from equation 7.10.

Assume two test natural frequencies ω_a, ω_b and their corresponding damping factors ζ_a, ζ_b are determined. Then equation 7.10 can be rearranged to the following equations:

$$\alpha = \frac{2 * \omega_a * \omega_b * (\omega_a\zeta_b - \omega_b\zeta_a)}{\omega_a^2 - \omega_b^2} \tag{7.11}$$

$$\beta = \frac{2 * \omega_a * \zeta_a - 2 * \omega_b * \zeta_b}{\omega_a^2 - \omega_b^2} \tag{7.12}$$

From equation 7.10, it can be seen that when the undamped natural frequency of the system is relatively small, the damping ratio is dominated by α. However, as the undamped natural frequency increases, the damping ratio of the system is dominated by the constant β.

Using the natural frequencies and damping factors from mode 1 and 2 from the dynamic test data in table 3.2, the initial guess of Rayleigh damping constants α and β are shown in table 7.1.

Table 7.1 Initial Estimation of α and β Using Mode 1 and 2 From Dynamic Test Data

Dynamic Test Data		
Mode Number	**Undamped Frequencies (Hz)**	**Damping Coefficient (%)**
1	1506.59	0.66
2	2019.57	0.71
Rayleigh Damping Coefficient		
α	8.8558	
β	4.86e-6	

Table 7.2 shows the sensitivity analysis of the Rayleigh damping constants α and β. It is clear that β is much more sensitive to the natural frequency of the system comparing with α.

Rayleigh damping model is selected because it can be easily implemented into the FE modelling softwares such as ABAQUS whereas other damping models may not be applicable to some Finite Element Softwares.

Table 7.2 Sensitivity of α and β values

		Changes in Rayleigh Damping Ratio:								
Changes in Resultant Eigenvalues:	Mode Number	Original (α=8.8558, β=4.86e-6)	α*10	Relative Difference	α/10	Relative Error	β*10	Relative Difference	β/10	Relative Difference
			88.558		0.88558		4.86e-5		4.86e-7	
	1	0.0406	0.0406	0.00%	0.0405	0.21%	0	100.00%	0.00415	89.79%
	2	0.0448	0.0448	0.00%	0.0447	0.19%	0	100.00%	0.00456	89.82%
	3	0.0918	0.0918	0.00%	0.0918	0.04%	0	100.00%	0.00921	89.97%
	4	0.10025	0.10025	0.00%	0.10021	0.04%	0	100.00%	0.01005	89.98%
	5	0.11589	0.11589	0.00%	0.11586	0.03%	0.4137	257.00%	0.01160	89.99%
	6	0.13215	0.13215	0.00%	0.13212	0.02%	0.4582	246.74%	0.01321	90.00%
	7	0.16594	0.16594	0.00%	0.16592	0.01%	4.9167	2862.94%	0.01656	90.02%
	8	0.1861	0.1861	0.00%	0.18608	0.01%	1.0313	454.16%	0.01855	90.03%
	9	0.23713	0.23713	0.00%	0.23712	0.00%	1.156	387.50%	0.02357	90.06%
	10	0.25798	0.25798	0.00%	0.25797	0.00%	1.4168	449.19%	0.02560	90.08%

7.2.2 Applying Rayleigh Damping Formula

The theoretical implementation and validation of the Rayleigh damping model in ABAQUS is presented in section 7.2.2. The Rayleigh damping constants α and β are determined using the Sensitivity method as shown in chapter 5. The procedures to validate the Sensitivity method against the determination of the Rayleigh damping constants are:

- Setup pad FE model with the initial guess $\alpha_1 = 10$ and $\beta_1 = 5 * 10^{-6}$ based from the test data. The complex eigenvalues, complex eigenvectors and damping coeffieicnts of each mode are analysed from ABAQUS and used as the 'theoretical test data' collected.

- The material properties of the pad FE model will not be updated and the determined material properties in table C.4 is used in this section.

- Note that since the complex eigenvalues are very sensitive to β, the range of β is set as $\pm 30\%$.

- Further details of the updating process is explained in section 5.2.1.

Figure 7.1 and table 7.3 shows the comparison between the test and updated damping coefficients between each mode using the α and β values updated from the Sensitivity method from different iteration steps. It is clear that the trend of the updated damping ratios are dominated by the updated β value and the trend of the pad test damping ratio is different from the trent of the analytical damping ratio from ABAQUS. Further investigation is needed on more reliable damping testing method as well as analytical method.

151
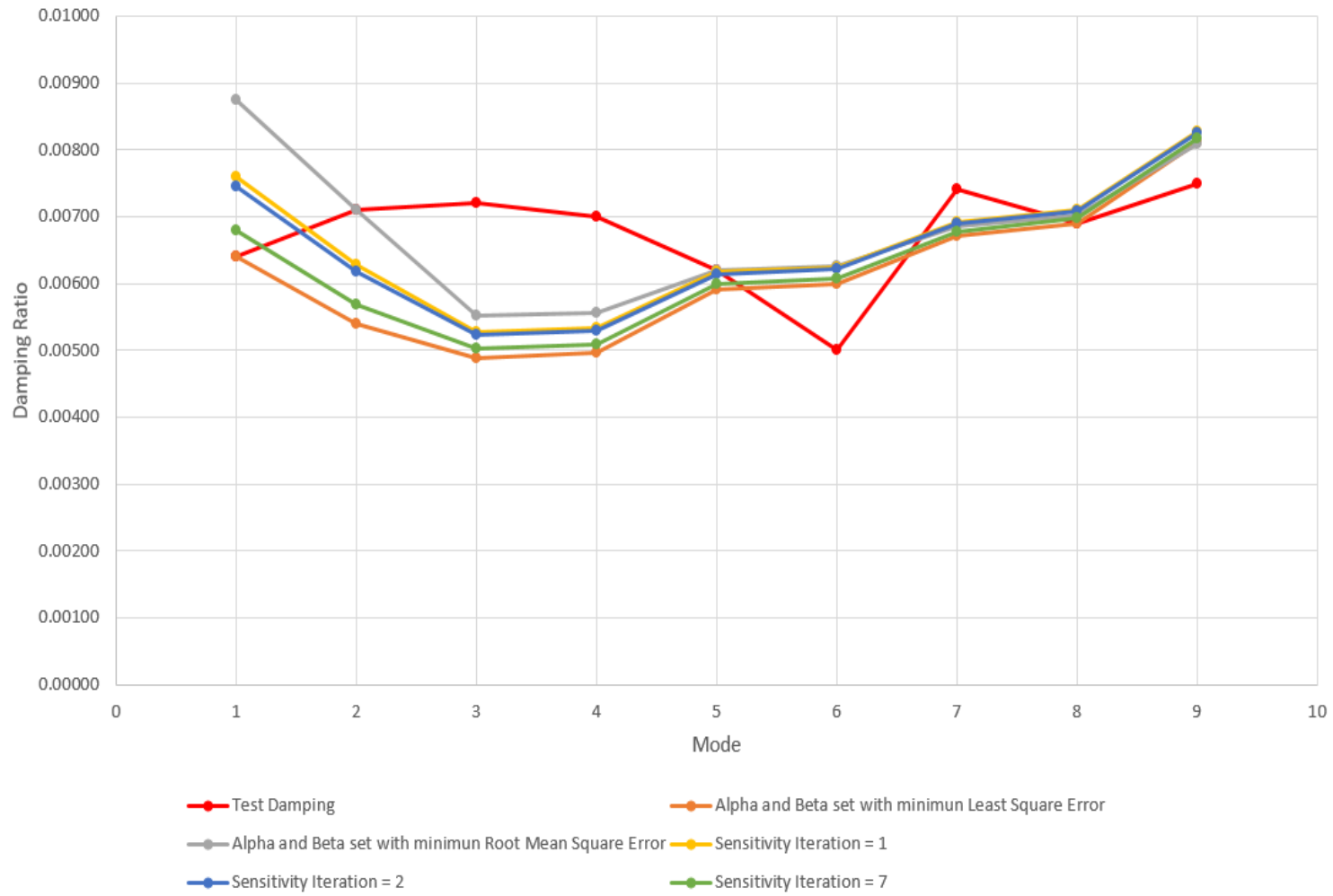
Figure 7.1 Calculated damping factors for each mode using conventional Rayleigh Damping formula

Table 7.3 Damping Factors Simulation using conventional Rayleigh Damping formula

Mode Number	Methods:	Damping from Test data	Alpha and Beta set with minimun Least Squares Difference	Alpha and Beta set with minimun Root Mean Square Difference	Sensitivity Iteration = 1	Sensitivity Iteration = 2	Sensitivity Iteration = 7
	alpha		1.02E+02	1.47E+02	1.24E+02	1.22E+02	1.09E+02
	beta		2.17E-06	2.07E-06	2.17E-06	2.17E-06	2.17E-06
1	Damping, zeta 1	6.4E-03	6.4E-03	8.74E-03	7.59E-03	7.45E-03	6.80E-03
2	Damping, zeta 2	7.1E-03	5.39E-03	7.10E-03	6.27E-03	6.17E-03	5.68E-03
3	Damping, zeta 3	7.2E-03	4.88E-03	5.52E-03	5.28E-03	5.23E-03	5.01E-03
4	Damping, zeta 4	7.0E-03	4.96E-03	5.55E-03	5.33E-03	5.29E-03	5.09E-03

5	Damping, zeta 5	6.2E-03	5.91E-03	6.20E-03	6.17E-03	6.14E-03	6.00E-03
6	Damping, zeta 6	5.0E-03	5.99E-03	6.26E-03	6.24E-03	6.21E-03	6.07E-03
7	Damping, zeta 7	7.4E-03	6.70E-03	6.86E-03	6.92E-03	6.89E-03	6.78E-03
8	Damping, zeta 8	6.9E-03	6.90E-03	7.02E-03	7.11E-03	7.08E-03	6.97E-03
9	Damping, zeta 9	7.5E-03	8.10E-03	8.08E-03	8.27E-03	8.25E-03	8.16E-03
	Least Squares Error		3.03E-01	3.06E-01	2.54E-01	2.53E-01	2.73E-01
	Root Mean Square Error		1.26E-03	1.18E-03	1.10E-03	1.11E-03	1.18E-03

7.3 Summary

This chapter covers the formulations and fundamental theories of the damping identification methods. The pad material is considered as viscoselastic material and the Rayleigh damping formula is reviewed and applied to the brake pad FE model. The sensitivity of the constants α and β are presented in table 7.2.

The identification method such as the Sensitivity method is used to determine the Rayleigh damping coefficients. Data of the damping factors of the friction material collected from the dynamic experiments are used in this chapter.

The analytical complex eigenvalues and damping factors from the pad FE model is compared against the test complex eigenvalues and damping coefficient. The trend of the updated analytical damping coefficients using Rayleigh damping coefficients are plot against the trend of the test damping coefficients in Figure 7.1 and table 7.3.

It is found that the trend of the analytical damping factors from the updated Rayleigh damping coefficients does not match with the experimental damping factors measured from the dynamic test. Further investigation is needed on 1) the testing method to collect reliable experimental damping factors; 2) different damping models which is most suitable to the trend of the experiment damping factors of the pad.

Chapter 8 Conclusion and Further Work

8.1 Conclusions

In this research, the main conclusions can be summarised as in the following aspects:

- The comparison of the results from two dynamic test methods shown that when testing the pad in free-free condition using impact hammer, the measured data from the Acceleration/Force dynamic test gives less noise comparing with using the Velocity/Force dynamic testing method.
- A MATLAB proram was developed to automatically calculate the analytical mode shape of the pad in the FE model if the measured mode shape is given in the extracted universal file.
- The results from the compression test measuring the change in strain of the pad in all direction using DIC are more accurate and reliable than using the strain gauges. The DIC measurements give a better observation of the behaviour of the whole pad surface whereas the strain gauges only measures the local change in strain. Furthermore, the DIC method is easier to apply and more cost effective than using the strain gauges.
- The static test results shown that the pad is behaving similar as a viscoelastic material. Results in Figure 4.8 demonstrated that when repeating the compression test on a sample that is viscoelastic material, sufficient time must be give to allow the sample to restore to its original shape.
- The comparison between the Sensitivity identification method and the Nastran Optimisation method shown that the Sensitivity method gives more accurate identification results but the computation cost is larger. The Nastran Optimisiation method is more cost effective but the identified parameters are give less accurate prediction of the pad natural frequencies.
- It can be observe from identification results using different updating conditions (Appendix C) that the dynamic behaviour of the pad is most accurate if the pad is considered as orthotropic material, the test and analytical mode shapes are matched during the updating method, and the updating method is the Sensitivity method. The conditions such as

156

considering the pad as transversely isotropic material, not matching mode shapes, ot using Nastran optimization method, would give less accurate results.

- The pad friction material is considered as both elastic and hyperelastic in the thesis. The determined results shown that when the pad is under free-free condition, considering the pad as elastic material gives a must better prediction than considering the pad as hyperelastic material. Hence, the conclusion can be drawn that when the pad is under free-free condition, it is better to assume the pad is elastic material rather than hyperelastic material.

The conclusions of the thesis are shown above. Further research could be carried out about the brake pad and details of further work is shown below.

8.2 Further Work

Regarding the brake pad mechanical properties, the following work could be carried out in the future.

- The research of the experimental studies of brake systems showed during a brake application, plenty of heat can be generated. Therefore, thermal effects play a significant role in triggering brake squeal noise in these situations. Thermal effects of the material properties of the pad friction material and thermal deformation should be considered in future researches. Similarly, humidity can also be influential in certain situations and thus can also be considered.

- The pad condition in this paper were assumed to be new. However, in real life, the pad surface would wear out over time. The effect of surface wear on the tribological properties of the friction material and contact status was not considered and should be further investigated.

- Damping has attracted a large number of investigations and influences greatly the predictability of theoretical models. However, a reliable technique for measuring and modelling of damping of the friction

material is still lacking. An extensive study is needed to characterise damping of the friction material in FE models of brake systems.

Appendix A: Sensitivity Analysis for the Elastic Properties of the Pad with respect to Out-of-plane Frequencies
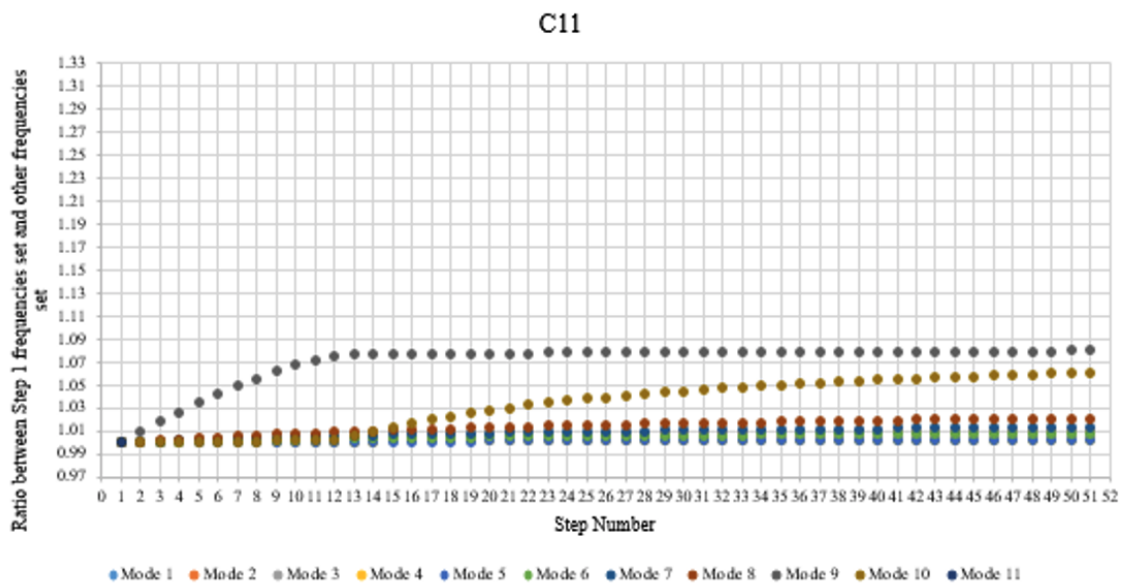
Figure A.1 Sensitivity analysis for elastic property C11 with respect to out-of-plane frequencies
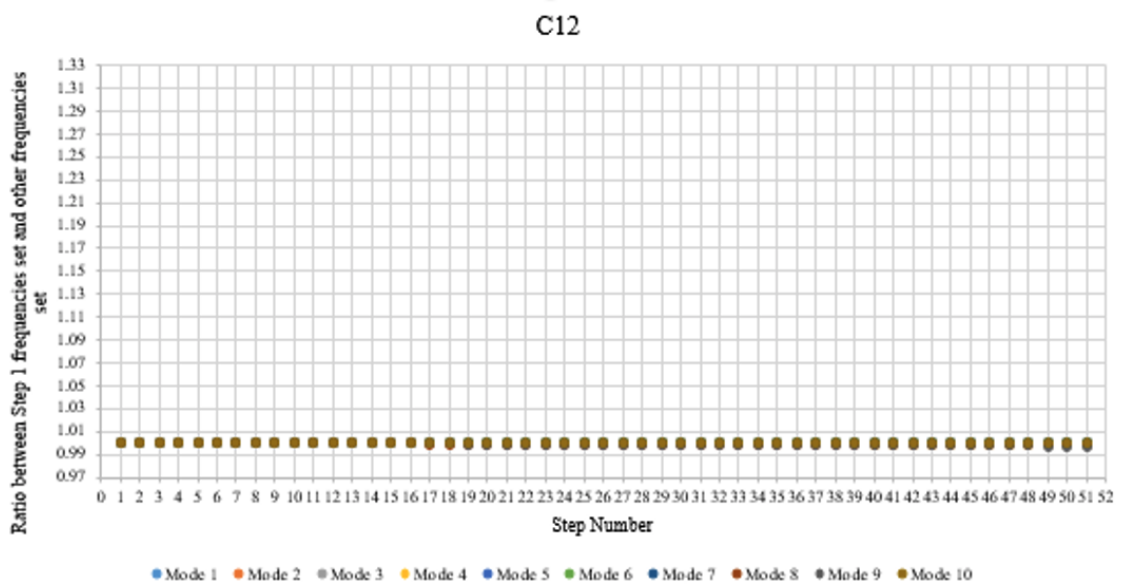
Figure A.2 Sensitivity analysis for elastic property C12 with respect to out-of-plane frequencies

159

C13
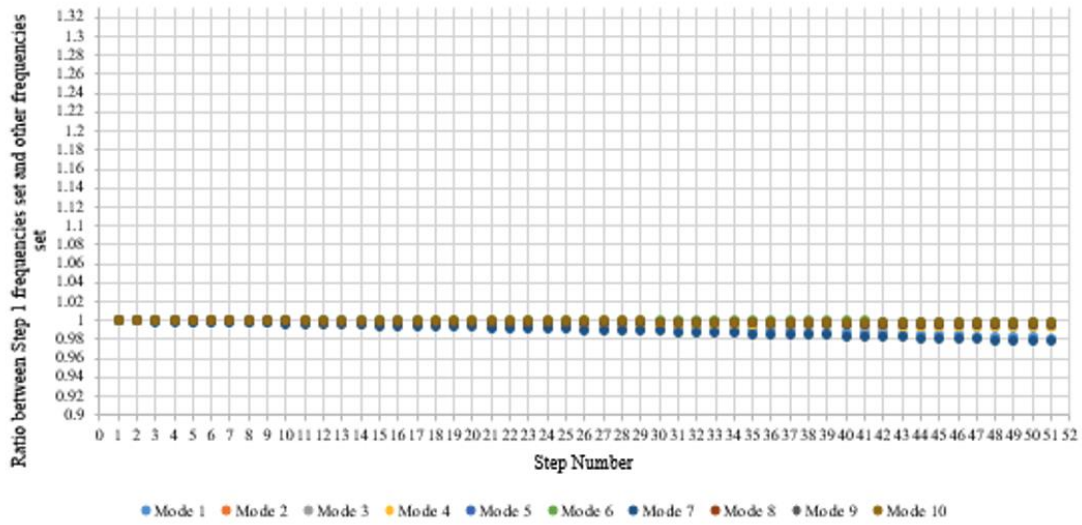
Figure A.3 Sensitivity analysis for elastic property C13 with respect to out-of-plane frequencies

C22
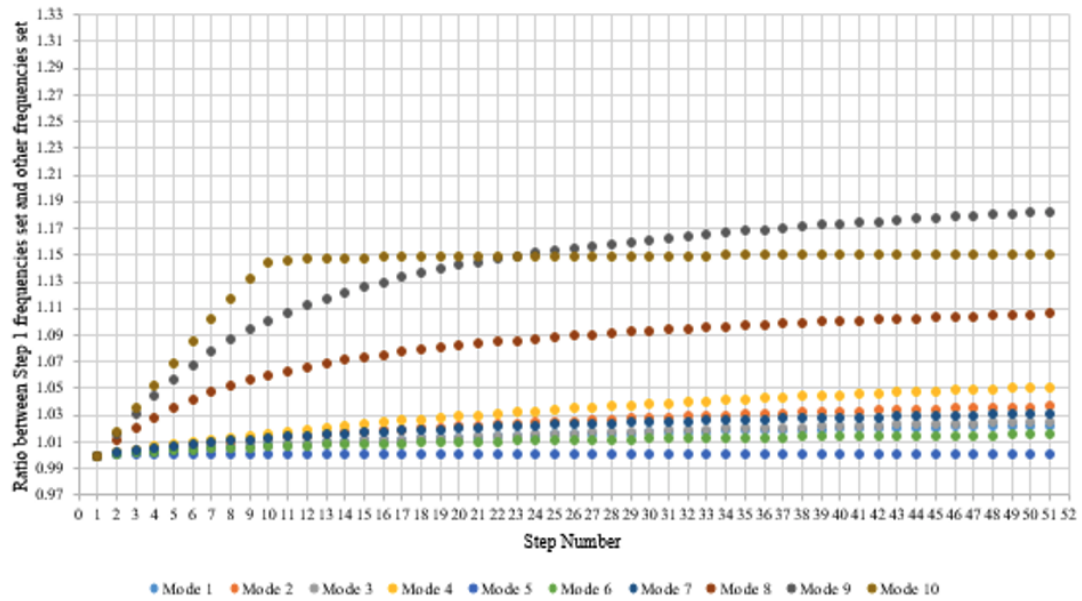
Figure A.4 Sensitivity analysis for elastic property C22 with respect to out-of-plane frequencies

160
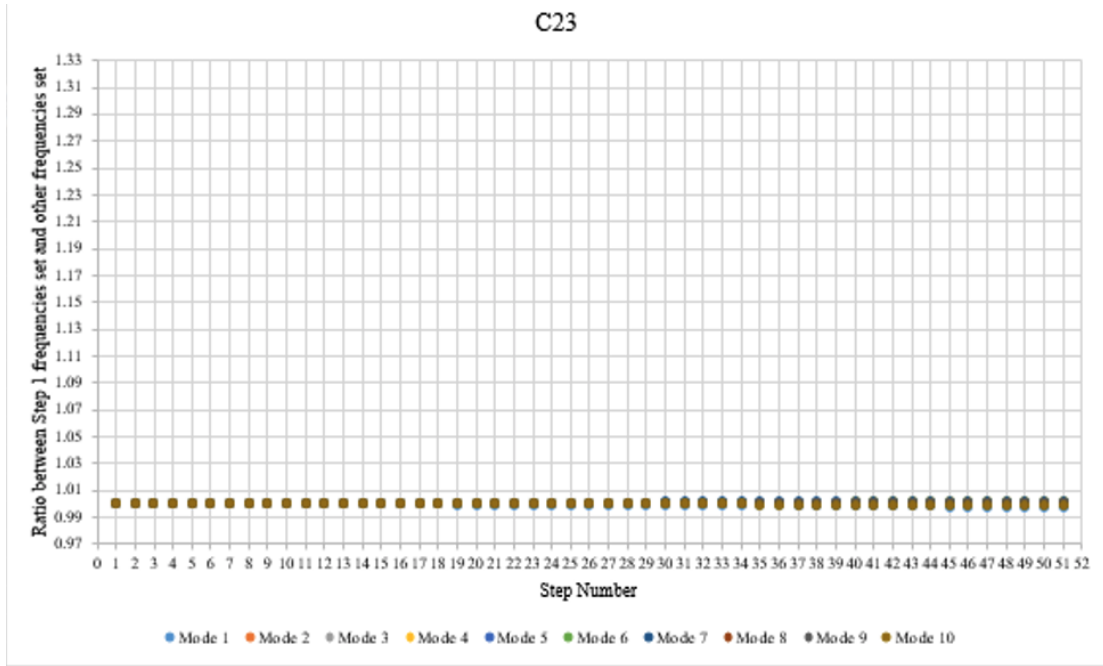
Figure A.5 Sensitivity analysis for elastic property C23 with respect to out-of-plane frequencies
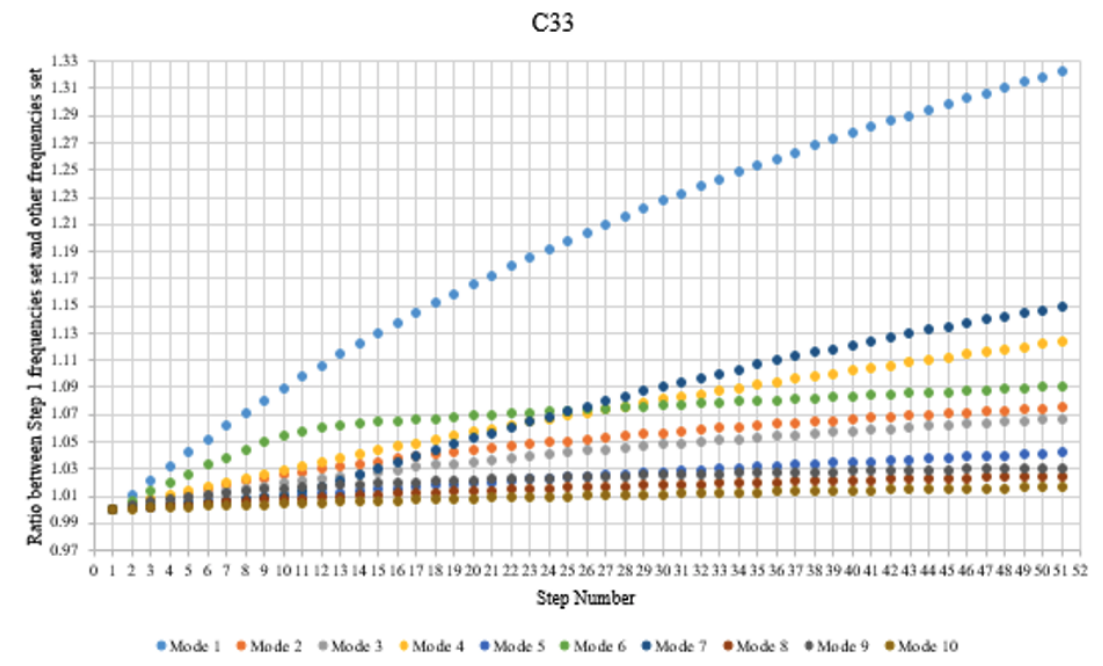
Figure A.6 Sensitivity analysis for elastic property C33 with respect to out-of-plane frequencies

161
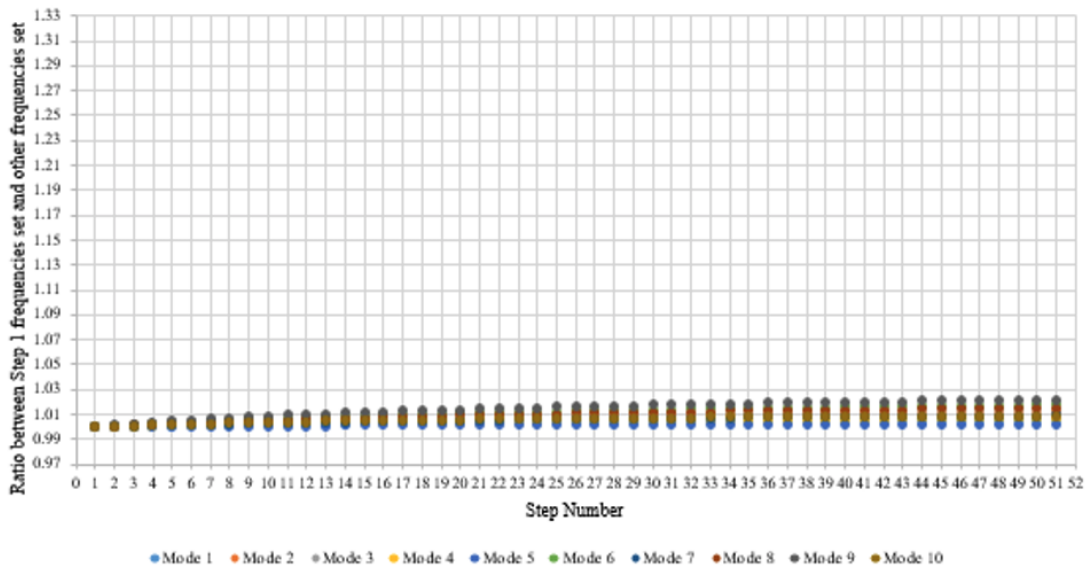
Figure A.7 Sensitivity analysis for elastic property C44 with respect to out-of-plane frequencies
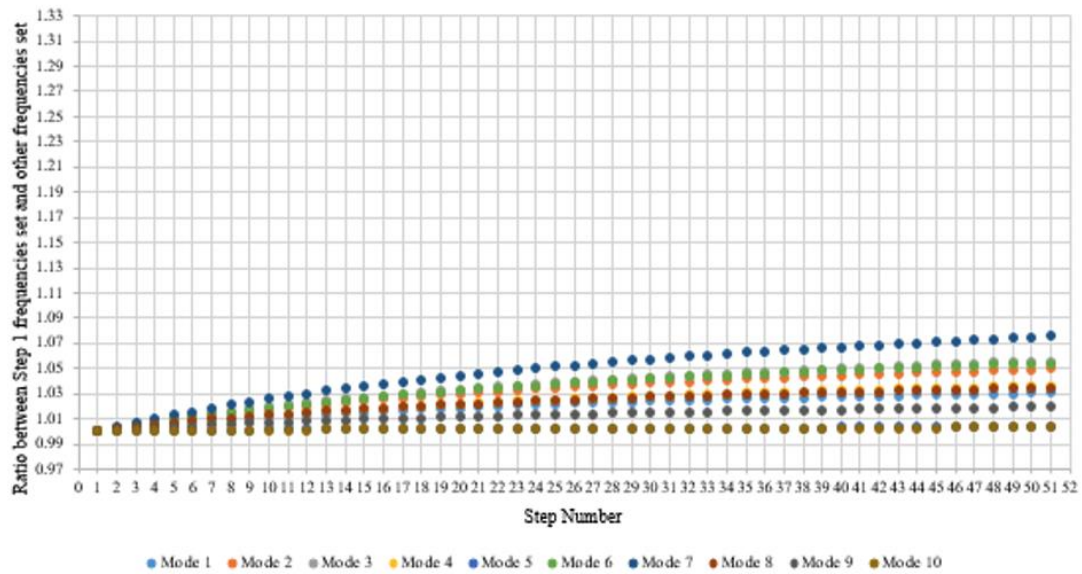
Figure A.8 Sensitivity analysis for elastic property C55 with respect to out-of-plane frequencies

162
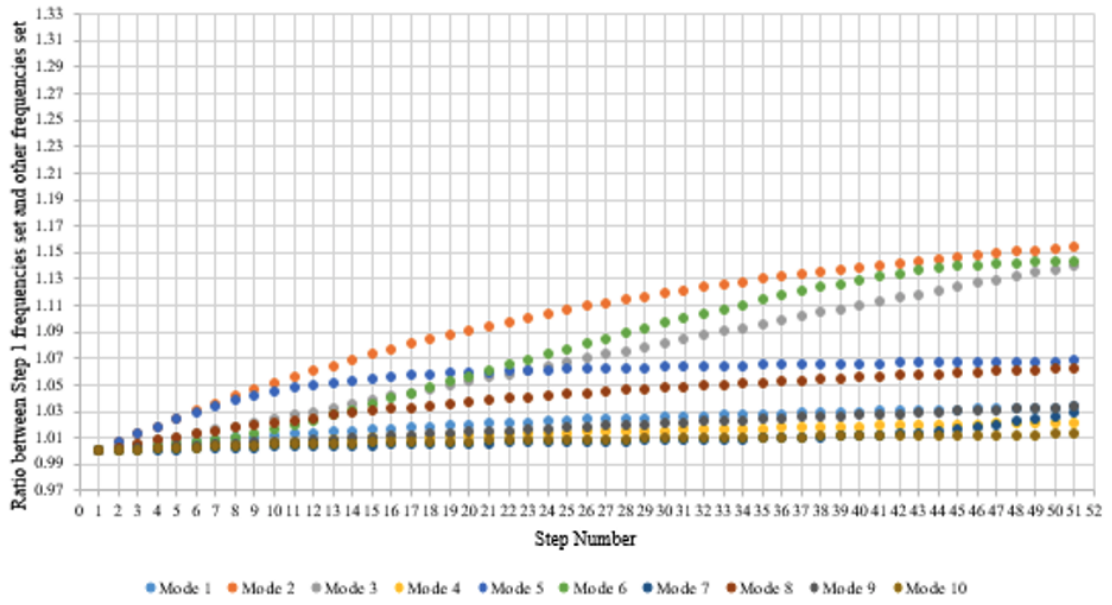
Figure A.9 Sensitivity analysis for elastic property C66 with respect to out-of-plane frequencies

Appendix B: Updated Pad Material Properties Using Sensitivity Method

Table B.1 Sensitivity Method, Transversely Isotropic Material, No Matching Mode Shape, Dynamic test data only

Material Properties Results Comparison					
	Original	Updated			
E(x)	8707	8165			
E(y)	8707	8165			
E(z)	533	597			
v(xy)	0.26	0.2			
v(xz)	0.46	0.47			
v(yz)	0.46	0.47			
G(xy)	3418	3784			
G(xz)	6613.9	9581.1			
G(yz)	6613.9	9581.1			

Frequency Results Comparison					
		Original Data		Updated Data	
Mode Number	Test Frequencies	Analytical Frequencies	Relative Error	Analytical Frequencies	Relative Error
1	1506.593398	1557.867	3.40%	1551.9	3.01%
2	2019.574692	2043.489	1.18%	2099	3.93%
3	4555.959192	4577.402	0.47%	4566.4	0.23%
4	4802.947124	4801.391	0.03%	4917	2.37%
5	6969.508014	6867.656	1.46%	6817	2.19%
6	7113.160435	7210.523	1.37%	7285.8	2.43%
7	7972.601296	7934.879	0.47%	7944.3	0.35%
8	8429.429841	8386.267	0.51%	8448.8	0.23%
9	8775.171121	8937.612	1.85%	8839.4	0.73%
10	10787.53407	10804.15	0.15%	10983	1.81%
11	11331.86158	11400.66	0.61%	11600	2.37%
12	12139.64464	12030.17	0.90%	12227	0.72%
13	16373.34637	13013.23	20.52%	13378	18.29%
Average Relative Error			2.53%		2.44%

Table B.2 Sensitivity Method, Transversely Isotropic Material, Mode Shape Matched, Dynamic test data only

Material Properties Results Comparison		
	Original	Updated
E(x)	8707	8063
E(y)	8707	8063
E(z)	533	601
v(xy)	0.26	0.18
v(xz)	0.46	0.47
v(yz)	0.46	0.47
G(xy)	3418	3350
G(xz)	6613.9	8237.2
G(yz)	6613.9	8237.2

Frequency Results Comparison

Original Data						Updated Data					
Test Matched Mode Number	Test Frequencies	Analytical Matched Mode Number	Analytical Frequencies	Relative Error	MAC Number	Test Matched Mode Number	Test Frequencies	Analytical Matched Mode Number	Analytical Frequencies	Relative Error	MAC Number
1	1506.5934	1	1557.866	3.40%	0.99349782	1	1506.5934	1	1546.8	2.67%	0.998387
2	2019.57469	2	2043.488	1.18%	0.99628036	2	2019.57469	2	2046.5	1.33%	0.983509
3	4555.95919	3	4577.399	0.47%	0.98246686	3	4555.95919	3	4545.2	0.24%	0.989332
4	4802.94712	4	4801.387	0.03%	0.99202228	4	4802.94712	4	4794.8	0.17%	0.987521
5	6969.50801	5	6867.655	1.46%	0.97467552	5	6969.50801	5	6847.4	1.75%	0.967698
6	7113.16044	6	7210.513	1.37%	0.89273297	6	7113.16044	6	7176.4	0.89%	0.971855
8	8429.42984	8	8386.269	0.51%	0.92517879	8	8429.42984	8	8344.5	1.01%	0.973705
9	8775.17112	9	8937.608	1.85%	0.96887887	9	8775.17112	9	8763	0.14%	0.984982
10	10787.5341	10	10804.14	0.15%	0.96561446	10	10787.5341	10	10795	0.07%	0.995169
11	11331.8616	11	11400.66	0.61%	0.97869227	11	11331.8616	11	11440	0.95%	0.980509
12	12139.6446	12	12030.15	0.90%	0.94825561	12	12139.6446	12	12095	0.37%	0.955644
Average Relative Error				1.09%						0.87%	

Table B.3 Sensitivity Method, Orthotropic Material, Mode Shape Matched, Dynamic test data only

Material Properties Results Comparison

	Original	Updated
E(x)	8707	8120
E(y)	8707	9012
E(z)	533	632
v(xy)	0.26	0.21
v(xz)	0.46	0.48
v(yz)	0.46	0.47
G(xy)	3418	3091
G(xz)	6613.9	8935.4
G(yz)	6613.9	5645.7

Frequency Results Comparison

Original Data						Updated Data					
Test Matched Mode Number	Test Frequencies	Analytical Matched Mode Number	Analytical Frequencies	Relative Error	MAC Number	Test Matched Mode Number	Test Frequencies	Analytical Matched Mode Number	Analytical Frequencies	Relative Error	MAC Number
1	1506.5934	1	1557.866	3.40%	0.99349782	1	1506.5934	1	1550.5	2.91%	0.982578
2	2019.57469	2	2043.488	1.18%	0.99628036	2	2019.57469	2	2014.8	0.24%	0.988960
3	4555.95919	3	4577.399	0.47%	0.98246686	3	4555.95919	3	4551.9	0.09%	0.984815
4	4802.94712	4	4801.387	0.03%	0.99202228	4	4802.94712	4	4830.8	0.58%	0.987077
5	6969.50801	5	6867.655	1.46%	0.97467552	5	6969.50801	5	6900	1.00%	0.999058
6	7113.16044	6	7210.513	1.37%	0.89273297	6	7113.16044	6	7171.7	0.82%	0.991621
8	8429.42984	8	8386.269	0.51%	0.92517879	8	8429.42984	8	8386.5	0.51%	0.998877
9	8775.17112	9	8937.608	1.85%	0.96887887	9	8775.17112	9	8777.6	0.03%	0.991568
10	10787.5341	10	10804.14	0.15%	0.96561446	10	10787.5341	10	10739	0.45%	0.992579
11	11331.8616	11	11400.66	0.61%	0.97869227	11	11331.8616	11	11426	0.83%	0.987953
12	12139.6446	12	12030.15	0.90%	0.94825561	12	12139.6446	12	12152	0.10%	0.989394
Average Relative Error				1.09%						0.69%	

Table B.4 Sensitivity Method, Transversely Isotropic Material, Mode Shape Matched, Dynamic and Static test data

Material Properties Results Comparison		
	Original	Updated
E(x)	8707	8179
E(y)	8707	8179
E(z)	533	614
v(xy)	0.26	0.19
v(xz)	0.46	0.45
v(yz)	0.46	0.45
G(xy)	3418	3182
G(xz)	6613.9	8317.1
G(yz)	6613.9	8317.1

Frequency Results Comparison

Original Data						Updated Data					
Test Matched Mode Number	Test Frequencies	Analytical Matched Mode Number	Analytical Frequencies	Relative Error	MAC Number	Test Matched Mode Number	Test Frequencies	Analytical Matched Mode Number	Analytical Frequencies	Relative Error	MAC Number
1	1506.5934	1	1557.866	3.40%	0.99349782	1	1506.5934	1	1550.7	2.93%	0.994617
2	2019.57469	2	2043.488	1.18%	0.99628036	2	2019.57469	2	2029.4	0.49%	0.987007
3	4555.95919	3	4577.399	0.47%	0.98246686	3	4555.95919	3	4557.9	0.04%	0.994390
4	4802.94712	4	4801.387	0.03%	0.99202228	4	4802.94712	4	4756.3	0.97%	0.999541
5	6969.50801	5	6867.655	1.46%	0.97467552	5	6969.50801	5	6860.3	1.57%	0.996388
6	7113.16044	6	7210.513	1.37%	0.89273297	6	7113.16044	6	7164.3	0.72%	0.995021
8	8429.42984	8	8386.269	0.51%	0.92517879	8	8429.42984	8	8342.6	1.03%	0.999123
9	8775.17112	9	8937.608	1.85%	0.96887887	9	8775.17112	9	8799.4	0.28%	0.988587
10	10787.5341	10	10804.14	0.15%	0.96561446	10	10787.5341	10	10763	0.23%	0.996163
11	11331.8616	11	11400.66	0.61%	0.97869227	11	11331.8616	11	11420	0.78%	0.993891
12	12139.6446	12	12030.15	0.90%	0.94825561	12	12139.6446	12	12112	0.23%	0.992539
Average Relative Error				1.09%						0.84%	

Appendix C: Updated Pad Material Properties Using Nastran Optimisation Method

Table C.1 Nastran Optimisation Method, Transversely Isotropic Material, No Matching Mode Shape, Dynamic test data only

Material Properties Results Comparison						
	Original	Updated				
C11	9551.697058	8468.82				
C12	2641.379598	1654.36				
C13	343.3442672	333.843				
C22	9551.697058	8468.82				
C23	343.3442672	333.843				
C33	552.3364299	843.888				
C44	3418	3111.98				
C55	6613.9	10385.8				
C66	6613.9	10385.8				

Frequency Results Comparison						
		Original Data			Updated Data	
Mode Number	Test Frequencies	Analytical Frequencies	Relative Error		Analytical Frequencies	Relative Error
1	1506.593398	1557.867	3.40%		1554.893	3.21%
2	2019.574692	2043.489	1.18%		2031.605	0.60%
3	4555.959192	4577.402	0.47%		4558.334	0.05%
4	4802.947124	4801.391	0.03%		4749.08	1.12%
5	6969.508014	6867.656	1.46%		6858.158	1.60%
6	7113.160435	7210.523	1.37%		7174.731	0.87%
7	7972.601296	7934.879	0.47%		7934.327	0.48%
8	8429.429841	8386.267	0.51%		8348.649	0.96%
9	8775.171121	8937.612	1.85%		8787.623	0.14%
10	10787.53407	10804.15	0.15%		10774.83	0.12%
11	11331.86158	11400.66	0.61%		11451.04	1.05%
12	12139.64464	12030.17	0.90%		12260.34	0.99%
13	16373.34637	13013.23	20.52%		13439.38	17.92%
Average Relative Error			2.53%			2.24%

Table C.2 Nastran Optimisation Method, Transversely Isotropic Material, Mode Shape Matched, Dynamic test data only

Material Properties Results Comparison		
	Original	Updated
C11	9551.69706	8597.64
C12	2641.3796	1649.14
C13	343.344267	338.92
C22	9551.69706	8597.64
C23	343.344267	338.92
C33	552.33643	609.814
C44	3418	3270.98
C55	6613.9	7249.84
C66	6613.9	7249.84

Frequency Results Comparison

Original Data						Updated Data					
Test Matched Mode Number	Test Frequencies	Analytical Matched Mode Number	Analytical Frequencies	Relative Error	MAC Number	Test Matched Mode Number	Test Frequencies	Analytical Matched Mode Number	Analytical Frequencies	Relative Error	MAC Number
1	1506.5934	1	1557.866	3.40%	0.99349782	1	1506.5934	1	1.55E+03	2.61%	0.99346549
2	2019.57469	2	2043.488	1.18%	0.99628036	2	2019.57469	2	2.03E+03	0.58%	0.99619942
3	4555.95919	3	4577.399	0.47%	0.98246686	3	4555.95919	3	4.54E+03	0.31%	0.98286162
4	4802.94712	4	4801.387	0.03%	0.99202228	4	4802.94712	4	4.76E+03	0.89%	0.99156817
5	6969.50801	5	6867.655	1.46%	0.97467552	5	6969.50801	5	6.84E+03	1.88%	0.97404946
6	7113.16044	6	7210.513	1.37%	0.89273297	6	7113.16044	6	7.14E+03	0.34%	0.89048942
8	8429.42984	8	8386.269	0.51%	0.92517879	8	8429.42984	8	8.30E+03	1.49%	0.92616832
9	8775.17112	9	8937.608	1.85%	0.96887887	9	8775.17112	9	8.74E+03	0.45%	0.96890489
10	10787.5341	10	10804.14	0.15%	0.96561446	10	10787.5341	10	1.07E+04	0.62%	0.96049482
11	11331.8616	11	11400.66	0.61%	0.97869227	11	11331.8616	11	1.14E+04	0.30%	0.97594987
12	12139.6446	12	12030.15	0.90%	0.94825561	12	12139.6446	12	1.20E+04	1.05%	0.96064948
Average Relative Error				1.09%						0.96%	

Table C.3 Nastran Optimisation Method, Orthotropic Material, Mode Shape Matched, Dynamic test data only

Material Properties Results Comparison

	Original	Updated
C11	9551.697058	8122.04
C12	2641.379598	1617.71
C13	343.3442672	342.566
C22	9551.697058	10042.2
C23	343.3442672	334.435
C33	552.3364299	618.958
C44	3418	3276.59
C55	6613.9	5964.39
C66	6613.9	7162.34

Frequency Results Comparison

Original Data						Updated Data					
Test Matched Mode Number	Test Frequencies	Analytical Matched Mode Number	Analytical Frequencies	Relative Error	MAC Number	Test Matched Mode Number	Test Frequencies	Analytical Matched Mode Number	Analytical Frequencies	Relative Error	MAC Number
1	1506.593398	1	1557.866	3.40%	0.993497822	1	1506.593398	1	1534.929	1.88%	0.993454428
2	2019.574692	2	2043.488	1.18%	0.996280358	2	2019.574692	2	2028.203	0.43%	0.996171067
3	4555.959192	3	4577.399	0.47%	0.982466864	3	4555.959192	3	4504.547	1.13%	0.983152017
4	4802.947124	4	4801.387	0.03%	0.99202228	4	4802.947124	4	4764.274	0.81%	0.990978471
5	6969.508014	5	6867.655	1.46%	0.974675523	5	6969.508014	5	6945.937	0.34%	0.973153007
6	7113.160435	6	7210.513	1.37%	0.892732965	6	7113.160435	6	7175.788	0.88%	0.889386356
8	8429.429841	8	8386.269	0.51%	0.925178793	8	8429.429841	8	8408.986	0.24%	0.926717169
9	8775.171121	9	8937.608	1.85%	0.96887887	9	8775.171121	9	8760.162	0.17%	0.96891694
10	10787.53407	10	10804.14	0.15%	0.965614456	10	10787.53407	10	10736.58	0.47%	0.94670371
11	11331.86158	11	11400.66	0.61%	0.978692274	11	11331.86158	11	11459.46	1.13%	0.975306049
12	12139.64464	12	12030.15	0.90%	0.94825561	12	12139.64464	12	12030.14	0.90%	0.963757168
Average Relative Error				1.09%						0.76%	

Table C.4 Nastran Optimisation Method, Transversely Isotropic Material, Mode Shape Matched, Dynamic and Static test data

Material Properties Results Comparison

	Original	Updated
C11	9551.69706	8687.38
C12	2641.3796	1684.62
C13	343.344267	341.77
C22	9551.69706	8687.38
C23	343.344267	341.77
C33	552.33643	600.172
C44	3418	3263.73
C55	6613.9	8179.13
C66	6613.9	8179.13

Frequency Results Comparison

Original Data						Updated Data					
Test Matched Mode Number	Test Frequencies	Analytical Matched Mode Number	Analytical Frequencies	Relative Error	MAC Number	Test Matched Mode Number	Test Frequencies	Analytical Matched Mode Number	Analytical Frequencies	Relative Error	MAC Number
1	1506.5934	1	1557.866	3.40%	0.99312595	1	1506.5934	1	1549.117	2.82%	0.99319878
2	2019.57469	2	2043.488	1.18%	0.98903894	2	2019.57469	2	2035.715	0.80%	0.98900662
3	4555.95919	3	4577.399	0.47%	0.98149629	3	4555.95919	3	4558.447	0.05%	0.98271569
4	4802.94712	4	4801.387	0.03%	0.98044902	4	4802.94712	4	4770.735	0.67%	0.98013646
5	6969.50801	5	6867.655	1.46%	0.95205574	5	6969.50801	5	6860.528	1.56%	0.95004059
6	7113.16044	6	7210.513	1.37%	0.87311461	6	7113.16044	6	7162	0.69%	0.86744157
8	8429.42984	8	8386.269	0.51%	0.90372959	8	8429.42984	8	8333.782	1.13%	0.90223741
9	8775.17112	9	8937.608	1.85%	0.95390627	9	8775.17112	9	8767.988	0.08%	0.95474763
10	10787.5341	10	10804.14	0.15%	0.94525676	10	10787.5341	10	10757.39	0.28%	0.94811914
11	11331.8616	11	11400.66	0.61%	0.94035256	11	11331.8616	11	11411.25	0.70%	0.94047686
12	12139.6446	12	12030.15	0.90%	0.9489008	12	12139.6446	12	12054.38	0.70%	0.95345196
Average Relative Error				1.09%						0.86%	

References

Chapter 10 Arnoldi and Lanczos algorithms [Online]. Available: http://people.inf.ethz.ch/arbenz/ewp/Lnotes/chapter10.pdf [Accessed].

ABAQUS 2014. Abaqus 6.14 Online Documentation.

AHMAD, M. A., SUBRAMANIAM, K. & GHOSN, M. 2006. Experimental Investigation and Fracture Analysis of Debonding between Concrete and FRP Sheets. *Journal of Engineering Mechanics-asce - J ENG MECH-ASCE,* 132.

AHN, S., NAM, C., CHOI, S., AN, D., KIM, I., SEO, K. & SOHN, C. 2021. A study on squeal noise reduction considering the pad shape of the disc brake system for urban railway vehicles. *Journal of Mechanical Science and Technology,* 35**,** 1923.

AKAY, A. 2002. Acoustics of friction. *Journal of the Acoustical Society of America,* vol. 111, no. 4, pp. 1525-1548.

ARRUDA, E. M. & BOYCE, M. C. 1993. A three-dimensional constitutive model for the large stretch behavior of rubber elastic materials. *Journal of the Mechanics and Physics of Solids,* 41**,** 389-412.

AUZINS, J., CHATE, A., RIKARDS, R. & SKUKIS, E. 2015. Metamodeling and robust minimization approach for the identification of elastic properties of composites by vibration method. *ZAMM - Journal of Applied Mathematics and Mechanics / Zeitschrift für Angewandte Mathematik und Mechanik,* 95**,** n/a-n/a.

BAJER, A., BELSKY, V. & KUNG, S.-W. 2004. *The Influence of Friction-Induced Damping and Nonlinear Effects on Brake Squeal Analysis*.

BARUCH, M. 1978. Optimization Procedure to Correct Stiffness and Flexibility Matrices Using Vibration Tests. *AIAA Journal,* 16**,** 1208-1210.

BEHRENDT, J., WEISS, C. & HOFFMANN, N. P. 2011. A numerical study on stick–slip motion of a brake pad in steady sliding. *Journal of Sound and Vibration,* 330**,** 636-651.

BERMAN, A. & NAGY, E. J. 1983. Improvement of a Large Analytical Model Using Test Data. *AIAA Journal,* 21**,** 1168-1173.

BRACE, W. F. 1972. Laboratory studies of stick-slip and their application to earthquakes. *Tectonophysics,* 14**,** 189-200.

BRUNETTI, J., MASSI, F., D'AMBROGIO, W. & BERTHIER, Y. 2016. A new instability index for unstable mode selection in squeal prediction by complex eigenvalue analysis. *Journal of Sound and Vibration,* 377**,** 106-122.

BRYANT, D., SOLMS, F., FIELDHOUSE, J. & ASHRAF, N. Investigation of brake pad vibration under dynamic squeal conditions. 2012.

CAI, R., HOLWECK, F., FENG, Z.-Q. & PEYRAUT, F. 2016. A new hyperelastic model for anisotropic hyperelastic materials with one fiber family. *International Journal of Solids and Structures,* 84**,** 1-16.

CARVALHO, J., DATTA, B. N., GUPTA, A. & LAGADAPATI, M. 2007. A direct method for model updating with incomplete measured data and without spurious modes. *Mechanical Systems and Signal Processing,* 21**,** 2715-2731.

CHEN, F., ABDELHAMID, M. K., BLASCHKE, P. & J., S. 2003. On automotive disc brake squeal, part III: Test and evaluation. *SAE Technical Papers*.

CHEN, G. X., LIU, Q. Y., JIN, X. S. & ZHOU, Z. R. 2008. Stability analysis of a squealing vibration model with time delay. *Journal of Sound and Vibration,* 311**,** 516-536.

CHEN, G. X. & ZHOU, Z. R. 2003. Correlation of a negative friction−velocity slope with squeal generation under reciprocating sliding conditions. *Wear,* 255**,** 376-384.

CHOI, K. K. & KIM, N. H. 2005. *Structural sensitivity analysis and optimization*, Springer Science+Business Media, Inc.

CROWTHER, A., ZHANG, N., LIU, D. K. & JEYAKUMARAN, J. K. 2004. Analysis and simulation of clutch engagement judder and stick-slip in automotive powertrain systems. *Proceedings of the Institution of Mechanical Engineers. Part D, Journal of automobile engineering,* 218**,** 1427-1446.

D. SINCLAIR, N. M. 1955. Frictional vibrations. *Journal of Applied Mechanics, Transactions of the ASME* 22**,** 13-207.

D'AMBROGIO, W. & FREGOLENT, A. 2003. Results Obtained by Minimising Natural Frequency and Antiresonance Errors of a Beam Model. *Mechanical Systems and Signal Processing,* 17**,** 29.

DANTE, R. C. 2015. *Handbook of Friction Materials and Their Applications,* Cambridge, UNITED KINGDOM, Elsevier Science & Technology.

DAY, A. 2014. Braking of Road Vehicles. Elsevier.

DOROSTI, M. Reduced-order model updating for prediction of performance variables in mechanical structures. 2017.

DOROSTI, M., FEY, R., HEERTJES, M., WAL, M. & NIJMEIJER, H. 2017. Iterative Pole-Zero Model Updating Using Multiple Frequency Response Functions.

DOROSTI, M., FEY, R. H. B., HEERTJES, M. F., VAN DE WAL, M. M. J. & NIJMEIJER, H. 2018. Iterative pole-zero finite element model updating using generic parameters. *Mechatronics,* 55**,** 180-193.

ELHILALI, F., FIHRI-FASSI, H. & OURIHI, R. 2021. Towards the development of an optimized numerical model of the brake system pad with natural material. *Materials Today: Proceedings,* 45**,** 5419-5425.

ESFANDIARI, A., BAKHTIARI-NEJAD, F., SANAYEI, M. & RAHAI, A. 2010a. Structural finite element model updating using transfer function data. *Computers & Structures,* 88**,** 54-64.

ESFANDIARI, A., SANAYEI, M., BAKHTIARI-NEJAD, F. & RAHAI, A. 2010b. Finite Element Model Updating Using Frequency Response Function of Incomplete Strain Data. *AIAA Journal,* 48**,** 1420-1433.

FIELDHOUSE, J., ASHRAF, N. & TALBOT, C. 2009. The Measurement and Analysis of the Disc/Pad Interface Dynamic Centre of Pressure and Its Influence on Brake Noise. *SAE International Journal of Passenger Cars - Mechanical Systems,* 1.

FIELDHOUSE, J. D. & NEWCOMB, T. P. 1996. Double pulsed holography used to investigate noisy brakes. *Optical diagnostics in the automotive industry,* 25**,** 455-494.

FOSBERRY, R. A. C. H. Z. 1961. *Disc brake squeal : its mechanism and suppression,* Lindley, Motor Industry Research Association.

FRISWELL, M., INMAN, D. & PILKEY, D. 1998. Direct Updating of Damping and Stiffness Matrices. *Aiaa Journal - AIAA J,* 36**,** 491-493.

FUH, J. S., CHEN, S. Y. & BERMAN, A. 1984. System identification of analytical models of damped structures. *25th Structures, Structural Dynamics and Materials Conference.* American Institute of Aeronautics and Astronautics.

FUNG, Y. C. 1993. *Biomechanics : mechanical properties of living tissues*, Springer.

GASSER, T. C. & HOLZAPFEL, G. A. 2002. A rate-independent elastoplastic constitutive model for biological fiber-reinforced composites at finite

strains: continuum basis, algorithmic formulation and finite element implementation. *Computational Mechanics,* 29**,** 340-360.

GASSER, T. C., OGDEN, R. W. & HOLZAPFEL, G. A. 2006. Hyperelastic modelling of arterial layers with distributed collagen fibre orientations. *Journal of The Royal Society Interface,* 3**,** 15-35.

GENT, A. N. 1996. A New Constitutive Relation for Rubber. *Rubber Chemistry and Technology,* 69**,** 59-61.

GIANNINI, O., AKAY, A. & MASSI, F. 2006. Experimental analysis of brake squeal noise on a laboratory brake setup. *Journal of Sound and Vibration,* 292**,** 1-20.

GIANNINI, O. & SESTIERI, A. 2006. Predictive model of squeal noise occurring on a laboratory brake. *Journal of sound and vibration,* 296**,** 583-601.

HACKETT, R. M. 2018. *Hyperelasticity Primer*, Springer International Publishing.

HAJHASHEMKHANI, M. & HEMATIYAN, M. 2015. Determination of material parameters of isotropic and anisotropic hyper-elastic materials using boundary measured data. *Journal of Theoretical and Applied Mechanics,* 53**,** 895-910.

HERVÉ, B., SINOU, J.-J., MAHÉ, H. & JEZEQUEL, L. 2009. Extension of the destabilization paradox to limit cycle amplitudes for a nonlinear self-excited system subject to gyroscopic and circulatory actions. Elsevier.

HERVÉ, B., SINOU, J. J., MAHÉ, H. & JEZEQUEL, L. 2008. Analysis of squeal noise and mode coupling instabilities including damping and gyroscopic effects. *European Journal of Mechanics - A/Solids,* 27**,** 141-160.

HOFFMANN, N., FISCHER, M., ALLGAIER, R. & GAUL, L. 2002. A minimal model for studying properties of the mode-coupling type instability in friction induced oscillations. *Mechanics Research Communications,* 29**,** 197-205.

HOLZAPFEL, G. & OGDEN, R. 2003. *Biomechanics of Soft Tissue in Cardiovascular Systems*.

HOLZAPFEL, G. A. 2000. *Nonlinear Solid Mechanics: A Continuum Approach for Engineering*, Wiley.

HOOKE, R. 1678. *Lectures de Potentia Restitutiva, Or of Spring Explaining the Power of Springing Bodies*, John Martyn.

HUH, U., LEE, C.-W., YOU, J.-H., SONG, C.-H., LEE, C.-S. & RYU, D.-M. 2019. Determination of the Material Parameters in the Holzapfel-Gasser-Ogden Constitutive Model for Simulation of Age-Dependent Material Nonlinear Behavior for Aortic Wall Tissue under Uniaxial Tension. *Applied Sciences,* 9**,** 2851.

IBRAHIM, R. A. 1994. Friction-Induced Vibration, Chatter, Squeal, and Chaos—Part II: Dynamics and Modeling. *Applied Mechanics Reviews,* 47**,** 227-253.

INSTRON. *What is Compression Testing?* [Online]. Available: https://www.instron.com/en/our-company/library/test-types/compression-test?region=Global%20Site&lang=en [Accessed 2021].

JARVIS, R. P. & MILLS, B. 1963. Vibrations Induced by Dry Friction. *Proceedings of the Institution of Mechanical Engineers,* 178**,** 847-857.

JONES, K. W. & TURCOTTE, J. S. 2002. Finite element model updating using antiresonant frequencies. *Journal of Sound and Vibration,* 252**,** 717-727.

JUNGWIRTH, M., HOFINGER, D. & WEINZIERL, H. A comparison of model order reduction methods used in different FE software tools. 2010 11th International Thermal, Mechanical & Multi-Physics Simulation, and Experiments in Microelectronics and Microsystems (EuroSimE), 26-28 April 2010 2010. 1-5.

KANG, J., KROUSGRILL, C. M. & SADEGHI, F. 2009. Comprehensive stability analysis of disc brake vibrations including gyroscopic, negative friction slope and mode-coupling mechanisms. *Journal of Sound and Vibration,* 324**,** 387-407.

KEIL, S. 2017. Technology and Practical Use of Strain Gages - With Particular Consideration of Stress Analysis Using Strain Gages. John Wiley & Sons.

KINKAID, N. M., O'REILLY, O. M. & PAPADOPOULOS, P. 2003. Automotive disc brake squeal. *Journal of Sound and Vibration,* 267**,** 105-166.

KINKAID, N. M., O'REILLY, O. M. & PAPADOPOULOS, P. 2005. On the transient dynamics of a multi-degree-of-freedom friction oscillator : a new mechanism for disc brake noise. *Journal of sound and vibration,* 287**,** 901-917.

KIRILLOV, O. 2004. Destabilization paradox. *Physics - Doklady,* 49**,** 239-245.

KOENEN, A. & SANON, A. 2007. Tribological and vibroacoustic behavior of a contact between rubber and glass (application to wiper blade). *Tribology International - TRIBOL INT,* 40**,** 1484-1491.

KRUSE, S., TIEDEMANN, M., ZEUMER, B., REUSS, P., HETZLER, H. & HOFFMANN, N. 2015. The influence of joints on friction induced vibration in brake squeal. *Journal of Sound and Vibration,* 340**,** 239-252.

KUMAR, S., PRIYADARSHAN & GHOSH, S. K. 2021. Statistical and artificial neural network technique for prediction of performance in AlSi10Mg-MWCNT based composite materials. *Materials Chemistry and Physics,* 273**,** 125136.

KUMAR, V. V. & KUMARAN, S. S. 2019. Friction material composite: types of brake friction material formulations and effects of various ingredients on brake performance–a review. *Materials Research Express,* 6.

KUO, Y.-C., LIN, W.-W. & XU, S. 2006. New Methods for Finite Element Model Updating Problems. *AIAA Journal,* 44**,** 1310-1316.

LALLEMENT, G. & INMAN, D. 1995. A Tutorial on Complex Eigenvalues.

LAMARQUE, P. V. & WILLIAMS, C. G. 1938. Brake squeak: the experiences of manufacturers and operators and some preliminary experiments. *The Institution of Automobile Engineers.,* Research report no. 8500 B.

LANCZOS, C. 1950. An iteration method for the solution of the eigenvalue problem of linear differential and integral operators. *Journal of research of the National Bureau of Standards,* 45**,** 255-282.

LEE, Y. 2006. Finite element model updating of loaded and geometrically modified structures. *Student thesis: Doctoral Thesis › Doctor of Philosophy (PhD).*

MAIA, N. M. M. & MONTALVÃO E SILVA, J. M. 1997. *Theoretical and experimental modal analysis*, Research Studies Press.

MANN, R., MAGNIER, V., SERRANO-MUNOZ, I., BRUNEL, J.-F., BRUNEL, F., DUFRENOY, P. & HENRION, M. 2017. Non-linear mechanical behavior of a sintered material for braking application using digital image correlation. *Mechanics & Industry,* 18**,** 601.

MARWALA, T. 2010. *Finite Element Model Updating Using Computational Intelligence Techniques: Applications to Structural Dynamics.*

MAXWELL, J. C. 1866. The Bakerian Lecture.--On the Viscosity or Internal Friction of Air and Other Gases. *Philosophical Transactions of the Royal Society of London,* 156**,** 249-268.

MCCONNELL, K. G. & VAROTO, P. S. 1995. *Vibration Testing: Theory and Practice*, Wiley.

MCCORMICK, N. & LORD, J. 2010. Digital Image Correlation. *Materials Today,* 13**,** 52-54.

MILLS, H. R. 1939. Brake squeak. *The Institution of Automobile Engineers.,* Research report nos.9000B (1938) and 9162 B.

MOONEY, M. 1940. A Theory of Large Elastic Deformation. *Journal of Applied Physics,* 11**,** 582-592.

MORTELETTE, L., BRUNEL, J. F., BOIDIN, X., DESPLANQUES, Y., DUFRÉNOY, P. & SMEETS, L. 2009. Impact of Mineral Fibres on Brake Squeal Occurrences. 400 Commonwealth Drive, Warrendale, PA, United States: SAE International.

MOTTERSHEAD, J. E., LINK, M. & FRISWELL, M. I. 2011. The sensitivity method in finite element model updating: A tutorial. *Mechanical Systems and Signal Processing,* 25**,** 2275-2296.

MOTTERSHEAD, J. E., OUYANG, H., CARTMELL, M. P. & FRISWELL, M. I. 1997. Parametric Resonances in an Annular Disc, with a Rotating System of Distributed Mass and Elasticity; And the Effects of Friction and Damping. *Proceedings: Mathematical, Physical and Engineering Sciences,* 453**,** 1-19.

MRÓZ, Z. & STAVROULAKIS, G. 2005. *Parameter Identification of Materials and Structures*.

MSCSOFTWARE 2012. MSC Nastran 2012 Design Sensitivity and Optimization User's Guide. USA: MSC.Software Corporation.

MUSCOPLAT, R. 2019. *Brake Pad Anatomy - Brake Pad Components* [Online]. Available: https://ricksfreeautorepairadvice.com/brake-pad-anatomy/ [Accessed Jan 2021].

NAGENDRA, G. K. & FLEURY, C. 1989. Sensitivity and optimization of composite structures in MSC/NASTRAN. *Finite Elements in Analysis and Design,* 5**,** 223-235.

NEWBY, W. R. 2014. Environmentally acceptable friction composites. University of Exeter.

NORTH, M. R. 1972. Frictionally induced, self excited vibrations in a disc brake system. Loughborough University.

OGDEN, R. W. & HILL, R. 1972. Large deformation isotropic elasticity: on the correlation of theory and experiment for incompressible rubberlike solids. *Proceedings of the Royal Society of London. A. Mathematical and Physical Sciences,* 326**,** 565-584.

ORTHWEIN, W. C. 2004. *Clutches and brakes. design and selection*, M. Dekker.

OUYANG, H., MOTTERSHEAD, J., BROOKFIELD, D., JAMES, S. & CARTMELL, M. 2000. Methodology for the determination of dynamic instabilities in a car disc brake. *International Journal of Vehicle Design,* 23**,** 241-262.

OUYANG, H., MOTTERSHEAD, J. E., CARTMELL, M. P. & FRISWELL, M. I. 1998. Friction-induced parametric resonances in discs : Effect of a negative friction-velocity relationship. *Journal of sound and vibration,* 209**,** 251-264.

OUYANG, H., NACK, W., YUAN, Y. & CHEN, F. 2005. Numerical analysis of automotive disc brake squeal: A review. *International Journal of Vehicle Noise and Vibration,* 1**,** 207-230.

OZEL, T., LLANOS, I., SORIANO, J. & ARRAZOLA, P. J. 2011. 3D FINITE ELEMENT MODELLING OF CHIP FORMATION PROCESS FOR MACHINING INCONEL 718: COMPARISON OF FE SOFTWARE PREDICTIONS. *Machining science and technology,* 15**,** 21-46.

PFEIFFER, F. & HAJEK, M. 1992. Stick-slip motion of turbine blade dampers. *Philosophical Transactions of the Royal Society of London. Series A: Physical and Engineering Sciences,* 338**,** 503 - 517.

POISSON, S. D. 1831. *Mémoire sur les équations générales de l'équilibre et du mouvement des corps solides élastiques et des fluides*, De l'Imprimerie royale.

POPP, K. & STELTER, P. 1990. Stick-Slip Vibrations and Chaos. *Philosophical Transactions: Physical Sciences and Engineering,* 332**,** 89-105.

PRANDINA, M. 2010. *Spatial Damping Identification.* Doctor in Philosophy, University of Liverpool.

QUAN, X., MO, J., HUANG, B., TANG, B., OUYANG, H. & ZHOU, Z. 2019. Influence of the Friction Block Shape and Installation Angle of High-Speed Train Brakes on Brake Noise. *Journal of Tribology,* 142.

RAO, S. S. 2017. *Mechanical Vibrations*, Pearson Education, Incorporated.

RAO, S. S. & YAP, F. F. 2011. *Mechanical vibrations*, Prentice Hall.

RAYLEIGH, J. W. S. B. & LINDSAY, R. B. 1898. The theory of sound - Second edition revised and enlarged. *Nature,* 58.

RIVLIN, R. S. & RIDEAL, E. K. 1948. Large elastic deformations of isotropic materials IV. further developments of the general theory. *Philosophical*

Transactions of the Royal Society of London. Series A, Mathematical and Physical Sciences, 241**,** 379-397.

RIVLIN, R. S., SAUNDERS, D. W. & ANDRADE, E. N. D. C. 1951. Large elastic deformations of isotropic materials VII. Experiments on the deformation of rubber. *Philosophical Transactions of the Royal Society of London. Series A, Mathematical and Physical Sciences,* 243**,** 251-288.

RUGSAJ, R. & SUVANJUMRAT, C. 2018. Finite Element Analysis of Hyperelastic Material Model for Non-Pneumatic Tire. *Key Engineering Materials,* 775**,** 554-559.

SAINDANE, U. V., SONI, S. & MENGHANI, J. V. 2021. Studies on mechanical properties of brake friction materials derived from carbon fibres reinforced polymer composite. *Materials Today: Proceedings,* 47**,** 5760-5765.

SEO, Y., KIM, Y., WITCZAK, M. W. & BONAQUIST, R. 2002. Application of Digital Image Correlation Method to Mechanical Testing of Asphalt-Aggregate Mixtures. *Transportation Research Record,* 1789**,** 162-172.

SIPPLE, J. D. & SANAYEI, M. 2014. Finite element model updating using frequency response functions and numerical sensitivities. *Structural Control and Health Monitoring,* 21**,** 784-802.

SOTO, A. & SALAZAR, G. 2009. *Asbestos : Risks, Environment and Impact,* New York, UNITED STATES, Nova Science Publishers, Incorporated.

SPURR, R. T. 1961. A theory of brake squeal. *Proceedings of the Institution of Mechanical Engineers; Automobile Division,* 15**,** 33-52.

STANBRIDGE, A. B. & EWINS, D. J. 1999. MODAL TESTING USING A SCANNING LASER DOPPLER VIBROMETER. *Mechanical Systems and Signal Processing,* 13**,** 255-270.

STENDER, M., PAPANGELO, A., ALLEN, M., BRAKE, M., SCHWINGSHACKL, C. & TIEDEMANN, M. 2016. Structural Design with Joints for Maximum Dissipation. Cham: Springer International Publishing.

STOKES, S. G. G. 1850. ON THE EFFECT OF THE INTERNAL FRICTION OF FLUIDS ON THE MOTION OF PENDULUMS. *In:* STOKES, G. G. (ed.) *Mathematical and Physical Papers.* Cambridge: Cambridge University Press.

SUNDARKRISHNAA, K. L. 2015. *Friction Material Composites. Copper-/Metal-Free Material Design Perspective*, Springer International Publishing.

TRICHÊS JÚNIOR, M., GERGES, S. N. Y. & JORDAN, R. 2008. Analysis of brake squeal noise using the finite element method: A parametric study. *Applied Acoustics,* 69**,** 147-162.

ÚRADNÍČEK, J., MUSIL, M., GAŠPAROVIČ, L. U. & BACHRATÝ, M. 2021. Influence of Material-Dependent Damping on Brake Squeal in a Specific Disc Brake System. *Applied Sciences,* 11**,** 2625.

VAN DE VELDE, F. & DE BAETS, P. 1996. Mathematical approach of the influencing factors on stick-slip induced by decelerative motion. *Wear,* 201**,** 80-93.

VIELSACK, P. 2001. Stick–slip instability of decelerative sliding. *International Journal of Non-linear Mechanics 36(2)* 237-247.

VON WAGNER, U., HOCHLENERT, D. & HAGEDORN, P. 2007. Minimal models for disk brake squeal. *Journal of Sound and Vibration,* 302**,** 527-539.

WAHLSTRÖM, J. 2011. *A study of airborne wear particles from automotive disc brakes.*

WEI, F.-S. 1990. Mass and stiffness interaction effects in analytical model modification. *AIAA Journal,* 28**,** 1686-1688.

WIECHERT, E. 1889. *Ueber elastische Nachwirkung*, Hartungsche buchdr.

WIECHERT, E. 1893. Gesetze der elastischen Nachwirkung für constante Temperatur. *Annalen der Physik,* 286**,** 546-570.

YANG, J., OUYANG, H. & ZHANG, J.-F. 2016. A new method of updating mass and stiffness matrices simultaneously with no spillover. *Journal of Vibration and Control,* 22**,** 1181.

YEOH, O. H. 1993. Some Forms of the Strain Energy Function for Rubber. *Rubber Chemistry and Technology,* 66**,** 754-771.

YUAN, Y. 1995. A Study of the Effects of Negative Friction-Speed Slope on Brake Squeal. *ASME 1995 Design Engineering Technical Conferences collocated with the ASME 1995 15th International Computers in Engineering Conference and the ASME 1995 9th Annual Engineering Database Symposium.*

ZIENKIEWICZ, O. C., TAYLOR, R. L. & ZHU, J. Z. Finite Element Method - Its Basis and Fundamentals (7th Edition). Elsevier.

ZRTMOTORSPORT. 2016. *Brakes Part 4: Brake Pads* [Online]. Available: https://www.zrtmotorsport.com/brakes-part-4-brake-pads/ [Accessed Jan 2021].